The Pennsylvania State University

The Graduate School

Department of Materials Science and Engineering

EXPLORING THE MECHANISMS OF PASSIVITY ON IRON: EXPERIMENTAL METHODS FOR CHARACTERIZING AND DEVELOPING MODELS TO DESCRIBE NANO-OXIDE GROWTH

A Thesis in

Materials Science and Engineering

by

Brian M. Marx

Submitted in Partial Fulfillment
of the Requirements
for the Degree of

Doctor of Philosophy

May 2006

The thesis of Brian M. Marx was reviewed and approved* by the following:

Digby D. Macdonald
Distinguished Professor of Materials Science and Engineering
Thesis Advisor
Chair of Committee

Howard W. Pickering
Distinguished Professor of Metallurgy

Long-Qing Chen
Professor of Materials Science and Engineering

Thomas E. Mallouk
Dupont Professor of Materials Chemistry
Outside Committee Member

James P. Runt
Professor of Polymer Science
Associate Head for Graduate Studies, Department of Materials Science and Engineering

*Signatures are on file in the Graduate School

ABSTRACT

In this thesis the passive oxide film formed on iron is studied using many experimental techniques in order to aid in the refinement of a Point Defect Model (PDM), which is capable of predicting and quantifying damage due to the general corrosion of iron. Many older electrochemical methods, like Mott-Schottky analysis, are incorporated with more modern techniques, such as scanning wavelength ellipsometry, electrochemical impedance spectroscopy, and XPS to probe the oxide film.

Ellipsometry is used to make in-situ thickness measurements that are performed in unison with potentiostatic and impedance experiments. XPS analysis is used to determine the concentrations of Fe^{2+} and Fe^{3+} present in the oxide film formed on iron. The information obtained is used to derive a PDM containing only oxygen vacancies. In addition, a new idea is proposed concerning three distinct regions over the passive range exhibited by iron in a borate buffer solution. Each region corresponds to a change in the electronic behavior of the film as evidenced by basic Mott-Schottky analysis. It is proposed that these different regions represent phase changes for the film.

Finally, the oxygen vacancy PDM is applied to implicitly determine if the major defects in the iron oxide film are oxide vacancies. The PDM is also fitted to the experimental data to yield the kinetic parameters and to make predictions concerning the steady-state thickness and current. A Warburg impedance is used in the fitting to obtain diffusivity data for the defects. The kinetic parameters are generated as both a function

of formation potential and temperature. A PDM, containing only oxygen vacancies, does not fit the data. Therefore, iron interstitials were added to the model, which yielded good fits to the data. A discussion is provided as to the interpretation of the results and the viability of applying the PDM to the iron system.

TABLE OF CONTENTS

LIST OF FIGURES

LIST OF TABLES

ACKNOWLEDGEMENTS

I would like to express my sincere gratitude to my advisor, Dr. Digby Macdonald, for his guidance, encouragement, and kindness during the course of this work. I would like to thank my colleagues and friends, especially Adan Sun and Balaji Soundarajan, for all of their help, support and advice. I would also like to thank Dr. Pickering for stirring up my interest in corrosion while taking his class. I thank my committee members for the time they spent discussing this project with me, as well as for their many suggestions regarding this work. I gratefully acknowledge the generous support by the Dept. of Energy which gave me the opportunity to work on this project.

I am eternally grateful for all of the love and support from my entire family. I thank my uncle Bruce for his endless help, support and encouragement during my time as a student. I thank my father for teaching me the meaning of the word “stick-to-it-tiveness”. I thank my mother for all of her encouragement and support. I am grateful to my wife for all of her patience. Most of all, I am indebted to my son, Colin, and daughter, Charlotte for being the best sources of motivation a person could have. This is dedicated to them.

Chapter 1

Introduction and Research Objectives

Although iron was first used by humans thousands of years ago, iron and steel (with the major constituent being iron) remain an integral part of modern society. Without iron, most engineered structures and technologies such as ships, automobiles, bridges, and skyscrapers could not exist in their modern forms and quantities, if at all. Iron and its alloys offer many advantages for engineering applications, with the key ones being its strength, formability and low production costs. However, it does have one major drawback: it corrodes relatively easily.

Corrosion is estimated to cost the U.S. $276 billion per year [1]. While material selection and corrosion prevention methods (i.e. coatings, sealants and corrosion inhibitors) make up the bulk of the up-front costs, inspection and corrosion maintenance are on-going costs and can contribute substantially to the overall cost. Inspection and maintenance can be time-consuming, labor-intensive, and not always 100% accurate. Therefore, developing a means by which corrosion damage can be monitored or even predicted, with minimal human input, could have a tremendous impact on the life-cycle costs of structures, vessels, and transportation vehicles.

An example demonstrating the impact that a reliable corrosion monitoring technique can have is very evident in applications dealing with the storage of hazardous liquid waste in metal containers. For instance the waste might need to be stored for

extended periods of time until it can be treated or it degrades on its own. A particular case is that dealing with the temporary storage of high level nuclear waste in tanks at the Savannah River and Hanford waste sites. These tanks will contain the liquid waste until it is approved to be vitrified and stored at the Yucca Mountain Repository. It has been estimated that the process of vitrifying and transferring the waste from the tanks to the repository should take 30-40 years, but could take as long as 100 years [2].

Due to the harmful constituents in the waste, it is not always feasible to visually inspect corrosion damage in the tanks. If proper inspections were to be performed, the tanks would have to be emptied and cleaned in order to inspect and repair any damage, while the waste is held temporarily in another container. This type of venture is both costly and dangerous to humans and the environment. In-situ monitoring methods, based on electrochemical techniques, can be used to constantly monitor corrosion and could possibly be used to predict when an inspection is necessary or to schedule maintenance. This could avoid unnecessary inspections and maintenance, which would be beneficial in terms of cost and safety.

Currently, there are 177 tanks containing 253 million liters of High Level Nuclear Waste (HLW) from fifty years of weapons production [3] at the Hanford site; the Savannah River site has 49 tanks storing 133 million liters of HLW[4-6]. The tanks that were constructed in the early 1950's were made primarily of ASTM A283 (at Hanford) and ASTM Type A285-50T (at Savannah River). These first tanks are single-walled and the welds were never stress-relieved. The tanks constructed after 1960 are primarily made of ASTM A516/A537 steel. These tanks are double-walled and the welds were stress relieved during fabrication.

Shortly after the early, single-walled tanks began storing waste (containing untreated nitrates) in the 1950's, leaks began to occur. Since this time leaks have occurred in a significant number of the single-walled tanks [2, 3]; 67 tanks are estimated to be leaking. The corrosion has been attributed to nitrate induced Stress-Corrosion Cracking (SCC) [7]. Although the waste originated from many sources and the composition of each tank is not truly known, the majority of the waste can be attributed to nuclear weapons production. In addition a smaller percentage of the waste is from the reprocessing of irradiated fuels from reactors used for energy production. The waste in the tank is found in the following forms:

- Supernatant Liquid – liquid containing dissolved species.
- Sludge – layer of water-insoluble chemicals (i.e. metal oxides, etc.) and un-dissolved soluble species that settle to the bottoms (or sides) of tanks.
- Saltcakes – created by the crystallization of salts due to the evaporation of the supernatant liquid.
- Slurry – mixture of solids suspended in the supernatant liquid.

Table **1-1** lists a compositional analysis, performed in the 1990's, of the soluble constituents in the HLW solid sludge contained in a tank in Savannah River [8]. The concentrations of radioactive species are not considered to have a major influence on the corrosion failure and are not listed in Table **1-1**. However, due to radioactive decay, the average temperature of the waste in the tanks is approximately 90°C. Analytical methods included gamma spectroscopy, alpha spectroscopy, beta spectroscopy, ion chromatography, inductively-coupled plasma emission spectroscopy (ICP-ES), inductively-coupled plasma mass spectroscopy (ICP-MS), cold vapor atomic absorption

spectroscopy (CV-AAS), acid-based titration, scanning electron microscopy, particle size distribution and X-ray diffraction (XRD).

Table **1-1**: Species Present in Tank at Savannah River Site

Species	**Concentration (wt %)**
Na	27 ± 1.2
Al	0.093 ± 0.005
P	0.37 ± 0.002
Zn	0.04 ± 0.001
Cr	0.021 ± 0.003
K	0.014 ± 0.0043
Free OH^-	1 ± 0.0009
$Al(OH)_4^-$	0.22 ± 0.012
CO_3^{2-}	6.5 ± 0.79
NO_3^-	44.1 ± 1.5
NO_2^-	0.5 ± 0.009
PO_4^{3-}	0.98 ± 0.11
SO_4^{2-}	0.038 ± .002
$Cr_2O_4^{2-}$	0.076 ± .004
Cl^-	0.02 ± 0.0003

Average concentrations and standard deviations of the soluble species present in the HLW analyzed for one tank at the Savannah River site (adapted from [8]). The remainder of the waste consists of the insoluble elements.

To combat the problem of stress corrosion cracking and pitting, additives such as nitrites (to prevent pitting/SCC) and sodium hydroxide (to raise the pH) were mixed with the waste during processing. Two tanks, containing low activity waste, at the Savannah River site have now been decommissioned (cleaned, sealed and deemed to be safe). The composition of the solids waste indicates that the bulk of the waste originated from the reprocessing of irradiated fuels. The average concentrations of species in the supernatant liquid waste removed from these tanks is shown in Table **1-2.** The amount of corrosion inhibitors (specifically, local corrosion inhibitors) is high enough that SCC and pitting are not considered to be an issue in these tanks.

Table **1-2**: Supernatant Liquid Analytical Results from Decommissioned Savannah River tank

Species	**Concentration**	**Units**
NO_3^-	.004	M
NO_2^-	.22	M
PO_4^{3-}	.002	M
CO_3^{2-}	.2	M
$Al(OH)_4$	.016	M
OH^-	.23	M
Na	.97	M
B	26	mg/L
Cr	1.0	mg/L
Si	6.5	mg/L
As	1.4	mg/L
Se	2.3	mg/L
^{137}Cs	.0002	μCi/mL
^{3}H	3.4	μCi/mL
^{99}Tc	.0007	μCi/mL
^{238}U	.000001	μCi/mL
^{239}Pu	.0002	μCi/mL
^{237}Np	.000001	μCi/mL

Predominant species found in the liquid contained in the waste removed from the decommissioned tank at the Savannah River site. The high hydroxide, high nitrite, and low nitrate concentrations greatly reduces the likelihood of stress-corrosion cracking or pitting damage (adapted from [8]).

Despite reducing the concerns over SCC and pitting, due mostly to the addition of corrosion inhibitors and pH control, failure due to general corrosion remains an issue for the fact that the waste might need to be contained for extended periods of time (as high as 100 years). It is well know that increasing the pH of a solution in contact with iron (or mild steels) enhances the passivity of the iron and greatly reduces the general corrosion damage. However, for long time periods and at elevated temperatures, failure due to general corrosion could be an issue.

To ensure tank integrity, Electrochemical Noise analysis (EN) has been used to monitor the types of corrosion occurring in the tanks. EN measures the fluctuations in the electrochemical currents and potentials which arise from the electrochemical reactions occurring on the corroding surfaces. By performing a statistical analysis of the temporal records, the type of corrosion can be identified. The differences in this technique are mainly found in the algorithm used to examine the data. Fast Fourier Transforms have been the preferred technique, but work on wavelet analysis has been applied recently, including on this project [9]. While exhibiting success with identifying local corrosion processes, the low current densities and small potential fluctuations attributed to general corrosion make it difficult to analyze with high accuracy due to external perturbations (i.e. artifacts in the measuring apparatuses or influence from equipment running near by).

Therefore, the focus of this thesis will be on describing the physical mechanisms that might be involved in the general corrosion process on iron and providing a method by which predicting damage could be possible. The arrangement is as follows:

- Chapter 2 – Review of the work on the passivity of iron.
- Chapter 3 – Introducing a Point Defect Model (PDM)
- Chapter 4 – Experimental Analysis of Iron Oxide
- Chapter 5 – Applying the PDM to Iron in Borate Buffer Solution

The knowledge acquired from studying and understanding the corrosion mechanisms involved in HLW containment can prove to be incredibly beneficial for future waste

processing control, containment design, and life-cycle predictions. In addition, it is the hope of the author that the insight gained from this work could prove beneficial in any area where iron is used: from automobiles to airplanes, from large structures to electronic circuits.

1.1 References

1. Technology, C. and International, N., *US Corrosion Costs*, N. International, Editor. 2005.
2. Hanson, L., A., *Radioactive Waste Contamination of Soil and Groundwater at the Hanford Site*. 2000, University of Idaho.
3. Ohl, P.C., Thomson, J.D., and Vollert, F.R. *Corrosion Considerations for Life Management of Hanford High Level Waste Tanks*. in *CORROSION/94*. 1994. Houston, TX: NACE International.
4. Laboratory, L.A.N., *The Actinide Research Quarterly: 2nd Quarter 2002*. 2002.
5. Subramanian, K.H., Zapp, P.E., and Wiersma, B.J., *Review of Corrosion Inhibition in High Level Radioactive Waste Tanks in the DOE Complex*. 2003, Westinghouse Savannah River Company, Savannah River Site.
6. Edgemon, G.L., et al., *Detection of Localized and General Corrosion of Mild Steel in Simulated Defense Nuclear Waste Solutions Using Electrochemcical Noise Analysis*. 1995, Westinghouse Hanford Company P.O. Box 1970 Richland, WA: Richland, Washington.
7. Lini, D.C., *Compilation of Hanford Corrosion Studies*. 1975, Atlantic Richfield Hanford Company Report.
8. Hobbs, D.T., et al., *Characterization of High Level Nuclear Wastes Stored at the Savannah River Site*. 1999, Westinghouse Savannah River Company.
9. Smith, M.T., *Wavelet Analysis of electrochemical noise data for monitoring corrosion in nuclear waste storage containers*, in *MatSE*. 2005, Pennsylvania State University: State College, PA.

Chapter 2

Models Describing the Passivity of Iron

2.1 Abstract

In this chapter, a review of many of the models proposed for describing anodic oxidation, particularly on iron, are reviewed. The details and rate-determining steps are briefly discussed. This review is being performed to illustrate the development of more detailed models over the course of the last century. By understanding the reasons why certain models were chosen over others can aid in the development of future models.

2.2 Overview

In 1836 Michael Faraday performed a set of experiments on iron in nitric acid solutions. He noticed that at a specific pH, the iron seemed to stop corroding. Schoenbein, Faraday's colleague, stated that the iron became passive, from which the word passivity was derived. Faraday surmised that a film, possibly an oxide, formed on the surface and that this film had two distinct characteristics. First, it rendered the iron passive and second, it was too thin to see by eye or even cause interference patterns from

reflected light (at least for the techniques available in his day). Today, we do know that it is an oxide film that forms and that it is approximately 2-6 nm thick.

It is easy to arrive at the conclusion that the passive nature of the film is directly related to the impedance of the film. Impedance is the measure of the resistance to electrical current flow when an electrical potential is applied across something (the film in this case) and it is comprised of both a resistance and a capacitance. If charge cannot move through the film easily, corrosion becomes difficult because it is an electrochemical process. This simple argument gives rise to the next question, how can charge pass through the oxide film? This question has been a focus of attention in the corrosion field since the first model was proposed in the 1930's by Verway [1].

Experimental work has shown that the oxide that forms on iron in oxygen containing environments has a logarithmic or parabolic growth rate [2-4]. In 1935, Verway proposed a model that accounted for cations migrating through the oxide film due to the existence of a high field within the film, with the rate of migration being exponentially dependent on the local field [1]. This model and all others that are based on this assumption are now referred to as "The High Field Models" (HFM). Since this time, there has been a wealth of work performed on iron in aqueous solutions and many models have been developed to describe the growth of iron oxide[4-15]. These models fall into categories that essentially differ only on the choice of the rate-determining step for oxide growth. Most models proposed in the literature are just variations of an original model from one of these categories. For this reason, only a few of the major models are reviewed here.

2.2.1 Verwey's High Field Model

Verwey's HFM describes the growth of a passive oxide film on aluminum in which the rate-determining step is assumed to be the migration of aluminum interstitials through the oxide film. Growth begins with the accumulation of oxygen ions at the surface of the metal. The oxygen lattice is assumed to grow at the outside surface, while metal cations are supplied from within and diffuse/migrate interstitially (in γ-Al_2O_3) through the film. At the onset of oxide formation, a high field across the film develops and metal cations migrate through the film. Upon film thickening, the electric field decreases until cation migration becomes insufficient and the film growth stops. The current at low field strengths is believed to be an electronic one. The current under high field conditions takes the simple form:

$$i = \alpha e^{\beta F} \qquad \textbf{2.1}$$

In Eq. **2.1** i represents the current, α is the jump probability of a cation interstitial and is shown in Eq. **2.2,** β is calculated by the Eq. **2.3,** and F is the electric field strength (V/cm)**.**

$$\alpha = \frac{0.24\, e\, k\, T}{a^2 \varphi_o \tau} e^{-\frac{\varphi_o}{kT}} \qquad \textbf{2.2}$$

$$\beta = \frac{3ae}{8kT} \qquad \textbf{2.3}$$

In the above equations, e is the electron charge, k is Boltzmann's constant, T is the absolute temperature, a is one half of the jump distance, ψ_o is the minimum potential

barrier, and τ is the time of vibration. The model shown here is for aluminum and the charge associated with the formation of an aluminum cation is $3e$.

As stated above, the model claims that the electric field decreases with thickness. By observing Eq. **2.1**, it is quite evident that the current will decay exponential with the film thickness. The electric field strength, F, in Eq. **2.1** is $\Delta V/L$, where V represents the potential and L is the thickness. As L increases, the current will decrease. Therefore, the model yields a logarithmic growth rate as experiments have shown.

2.2.2 Cabrera-Mott and Fehlner-Mott

A weakness of Verway's high field model is that for very thin films, the model predicts that the electric field in the film must be extremely high. For such a strong field, the migration will only occur in one direction and equilibrium could not occur because there must be a continual exchange of ions (i.e. every ion leaving the metal immediately migrates directly through the thin film). The Cabrera-Mott Model [3] assumes that the migration of cations through the film is very fast for high electric fields and could not possibly be the rate-determining step. Rather, they consider the injection of cation species at the metal/oxide interface to be the rate-determining step. Their derivation leads to an equation with the same form as Eq. **2.1**. Eq. **2.4** and Eq. **2.5** show the values of α and β in the current equation as predicted by the Cabrera-Mott model for very thin films (< 10 nm). The Fehlner-Mott model [16-18] is identical to the Cabrera-Mott model in every aspect, except they assume that the anions (e.g. oxygen in the film) are mobile.

$$\alpha = N' q \nu e^{-\frac{W}{kT}} \qquad \textbf{2.4}$$

$$\beta = \frac{qa}{kT} \qquad \textbf{2.5}$$

In the above equations, *N'* is the number of metal ions per surface area at the metal/film interface, q is the charge associated with the cations, ν is the vibration frequency, W represents the activation energy for the injection of a cation into the film, and *"a"* is one half the jump distance.

Essentially, both Verwey's and Cabrera-Mott's models assume a high field exists across the film and can be referred to as HFM's. It is very evident from the form of Eq. **2.1** that both models predict a logarithmic decay rate for the current. However, the current being described is the transient current and neither model predicts a steady-state current for potentiostatic conditions. In other words the HFM's are based on the rate of growth of the film and that as the current decreases to a negligible value; film growth can be viewed to no longer occur. Therefore, a steady-state current, or thickness, is never achieved.

2.2.3 Bean, Fisher, Vermilyea Model

The Bean-Fisher-Vermilyea Model (BFVM) [19] is yet another adaptation of a HFM. The difference in this model is that it considers the formation of Frenkel defects in the oxide film. Dewald [8] embelished the BFVM and refers to their model as the High Field-Frenkel Model. The BFVM claims that a metal cation on a cation site moves to

occupy an interstitial site and the interstitial cations are considered to be the mobile species in the film. The number of free ions in the film is then based on the rate of formation and annihilation of the Frenkel defects. The model assumes that the interstitials make no jumps against the high field. The basic outcome of the model is that as the field increases, both the number of interstitials and their mobilities increase up to a specific critical field. Above the critical field, there is little or no change in the number of interstitials, but the mobilities of the ions continue to increase with the field strength. The physical reason for the increase in ion mobility is attributed to the electrostatic interaction of the interstitial and the metal vacancy. This interaction modifies the potential energy of the ion in the lattice and ultimately results in a decrease in the jump distance of the ion. Again, the current equation takes on the same form as that shown in Eq. **2.1** and is shown in Eq. **2.6**

$$i = 2\lambda\nu N\, e^{-\left(\frac{Q+Q_1-q(\lambda_1+\lambda)F}{kT}\right)} \qquad \textbf{2.6}$$

In Eq. **2.6** Q is the activation energy for an interstitial jump at zero-field, Q_1 is the activation energy of interstitial formation at zero-field, λ is a distance related to the jump distance of an ion, λ_1 arises from the formation of the Frenkel defect and represents an intermediate jump distance smaller than λ. N is the equilibrium concentration of ion positions, ν is the frequency, F is the electric field, k is Boltzmann's constant and T is the temperature.

This model was introduced to better account for the change in activation energy for ion conduction with field strength. The results do account for this change fairly well and the model also yields a steady-state condition based on the rates of formation and

annihilation of defects. However, the charged vacancies formed in the oxide are assumed to be immobile, even in the presence of such a high field. This claim seems to be inconsistent with the fact that if the field is strong enough to produce Frenkel defects, it should be strong enough to allow for the movement of both types of defects, interstitial and vacancies. Another point of controversy is that the BFVM does not account for any effects due to the formation of a space charge layer at the interfaces. In other words, in all of the models above, charge-neutrality in the film is assumed to be compensated for (e.g. formation of vacancies accounting for the interstitial charges).

2.2.4 Young's Model

Continuing on the development of a model to describe the formation of a high ionic resistance oxide film, Young [11, 15] built on the previous concepts of the HFM. In his model Young considers both vacancies and interstitials to be mobile species. In addition Young considers that vacancies can form at the metal/oxide interface and in the oxide itself via Frenkel defects as in the BFVM. To make it more inclusive, Young considers the mobility of oxygen ions in the film. Young attributes the steady-state current to the ionic current through the film and the equation depicting this is shown in Eq. **2.7**. The transient current is also described in a qualitative manner, but is not discussed here.

$$i = q_O 2a_M \nu_O \left(\frac{m_I \nu_I}{2a_O \nu_O} \right) e^{\left(\frac{W_O - W_I - W_M}{kT} \right)} e^{(\beta_M + \beta_I - \beta_O)F} \qquad \textbf{2.7}$$

In Eq. **2.7** the subscripts "O" and "M" refer to oxygen and metal ions. The subscript "*l*" refers to the oxide/solution boundary, q is the charge on ion, a is the half jump distance for the ions, ν is the vibration frequency of ions, m is the concentration of metal vacancies, W is the activation energy at zero field, *a* is half jump distance, and β is the same as in the Cabrera-Mott Model, Eq. **2.5.**

The essential outcome of Young's Model (YM) is that the concentration of ions can vary with field strength (which is dependent on film thickness), thus leading to the formation of a space charge layer at one of the interfaces. This space charge layer isolates the oxide from the effects of the metal/oxide interface. The result is a model that predicts that the kinetics can be controlled by two mechanisms:

1. Kinetics are controlled by the reaction rates at the metal/film interface when the film is thin and the space charge effects are neglibible.
2. Kinetics are controlled by the migration of the mobile species in the oxide for thicker films when the space charge isolates the effects of the metal/film interface.

The YM behaves similar to the Cabrera-Mott Model for thin films due to the rate-determining step being the injection of metal ions at the metal/film interface. The key difference is that Young accounts for both metal vacancy and oxygen migration in the film. As the film grows, the rate-determining step becomes the migration of ions through the film as in Verwey's original HFM. Although metal vacancy and oxygen migration are accounted for, the current is attributed to the motion of metal ions. The other defects merely contribute to the formation of a space charge layer that changes the

rate-determining mechanism. The end result is that the YM reduces to the same form as that shown in Eq. **2.1**.

2.2.5 The Chemi-Conductor Model for Iron

The models mentioned here thus far have been general anodic oxidation models that can be applied to various metals. The Chemi-Conductor Model (CCM) was introduced by Cahan [7, 20, 21] in 1982 to account for the formation of the passive film on iron. The essential claim made by the CCM is that the oxide film is not a semi-conductor, but rather an insulator. Cahan defines a "chemi-conductor" material as a material whose stoichiometry changes by means of oxidative/reductive valence state changes.

Cahan performed an ellipsometric study of the passive film formed on iron in borate buffer solution [21]. From his results, Cahan believes the film is a single-layer film similar to α-Fe_2O_3 and no Fe_3O_4 is present. However, thermodynamics predict that Fe^{2+} must be present near the metal film interface. The CCM accounts for the excess charge, from Fe^{2+}, by suggesting that oxygen vacancies/protons are present in the film. The oxygen vacancies/protons are only present to explain charge nuetrality, and the iron ions in the film are used to explain the electronic properties of the film.

The CCM states that the conductivity of the passive film formed on iron varies with thickness due to the change in Fe^{2+} concentration through the film. Assuming that an electrostatic potential exists across the film, the Fe^{2+} ions will then migrate to establish a linear chemical gradient to balance the electrostatic potential at steady-state.

At lower formation potentials, the Fe^{2+} concentration "spreads" out more evenly through the film and dissolution becomes possible (Fe^{2+} being more soluble than Fe^{3+}). As the potential is raised, some of the Fe^{2+} is oxidized to Fe^{3+} (and Cahan claims to Fe^{4+} near the film/soln interface). The Fe^{2+} ions shift much closer to the metal/film interface and the variation of the oxidation states of iron ions (seen as dopants) through the film gives rise to the electronic properties of the film. For a linear chemical potential gradient, the variation in concentration of the iron ions through the film would be exponential; therefore, the conductivity would vary exponentially through the film. An exponential variation in conductivity (with thickness) is analagous to a description given by Young [15] on niobium oxide. Young's equations are used to explain the impedance of the film, however, no equations describing the current or thickness are given. The CCM has only been developed in a more qualitative manner.

2.2.6 Battaglia-Newman Model for Iron

The Battaglia-Newman Model (BNM) takes a more intimate look at the oxide film formed on iron. In their model [4] Battaglia and Newman follow the developments made concerning the understanding of the oxide formed on iron. They came to the conclusion that the mechanism(s) governing the oxide formation involve point defects. Credit is given to Frenkel [22] for developing the first of the "point defect models". However, MacDougall's [23] interpretation of a point defect model was also considered before Battaglia and Newman decided to base their formulation on the model developed by Macdonald and workers [12, 24, 25].

The BNM uses Wagner's approach [26] to describe the mobility of charged defects within the film. Based on structure studies and ring-disc electrode experiments, iron interstitials are viewed to be the dominant defect in the film. Both Fe^{3+} interstitials and electrons are regarded as mobile species in the film. The structure of the oxide formed on iron is considered to be γ-Fe_2O_3 with a variation in the concentration of Fe^{3+} interstitials through the thickness of the film. A higher Fe^{3+} concentration occurs closer to the metal/film interface and decreases through the film thickness. Battaglia claims that a γ-Fe_2O_3 structure with excess iron interstitials (8.4 M Fe^{3+} if the volume of the oxide is considered in liters as Battaglia does) is similar to the Fe_3O_4 structure and is most likely the reason for the problems in identifying the structure type. The variation in the concentration of iron interstitials is analogous to the CCM proposed by Cahan in which an exponential variation in the oxidation states of iron across the film forms under strong electric fields. Because iron ions and electrons are present in the oxide and metal, the potential drop across the metal/film interface is set to zero. The diffusion/migration of the mobile species through the film is the rate-determining step in the BNM.

The BNM uses three concepts to derive an equation describing the transient current as a function of applied potential. A mole balance is performed for each of the minor species in the film. Poisson's equation is used to account for any space-charge. A lattice velocity is applied to allow for the movement of the interfaces during growth. Solving these equations simultaneously will give the current density value. If the oxide was electrically neutral and there was no flux of electrons, the limiting current according to the BCM is shown in Eq. **2.8.**

$$i_{\lim} = 3F\left(\frac{4D_{Fe_i^{3+}} c_{Fe_i^{3+}}}{L}\right) \qquad \textbf{2.8}$$

Eq. **2.8** does not take into account any charging due to space-charge or double-layers forming. Rather, the equation is for the limiting case, where only the charged ionic species are responsible for the current. In Eq. **2.8** D represents the diffusivity of the interstitial iron cations, c is the concentration of interstitial cations and is dependent on the thickness and L is the thickness of the film. It should be noted that this equation is only for the limiting current case, but the BCM was developed to account for the transient currents. The fits shown in their paper are based on the transient equations and not on the limiting current case. However, an inclusive model should be able to account for steady-state conditions (e.g. potentiostatic conditions for long periods) and Eq. **2.8** represents a limiting current for a specific thickness and is not a true steady-state prediction.

Realizing that it is not possible to discuss every oxidation model, one other work should be mentioned in this section. Fromhold performed an exhaustive analysis on the oxidation of metals. However, due to the complexity and variety of the models (many with numerical analysis solutions), his work on the theory of oxidation [14] will not be discussed. Most of the models discussed in this chapter have many similar assumptions and vary only slightly in the treatment on how to best model oxide formation. These similarities will be discussed in further detail in the next chapter. Based on some of the ideas put forth by the work described here, another model describing the oxidation of iron will be proposed.

2.3 References

1. Verwey, J.W., *Electrolytic Conduction of a Solid Insulator at High Fields.* Physica, 1935. **2**: p. 1059.
2. Burstein, G.T. and Davenport, A.J., *The Current-Time Relationship during Anodic Oxide Film Growth under High Electric Field.* J. Electrochem. Soc., 1989. **136**(4): p. 936-941.
3. Cabrera, N. and Mott, N.F., *Theory of the Oxidation of Metals.* Reports in Progress of Physics, 1949. **12**: p. 163.
4. Battaglia, V. and Newman, J., *Modeling of a Growing Oxide Film: The Iron/Iron Oxide System.* J. Electrochem. Soc., 1995. **142**(5): p. 1423-1430.
5. Beverskog, B., et al., *A mixed-conduction model for oxide films on Fe, Cr and Fe-Cr alloys in high-temperature aqueous electrolytes--II. Adaptation and justification of the model.* Corrosion Science, 2002. **44**(9): p. 1923-1940.
6. Hendy, S.C., Laycock, N.J., and Ryan, M.P., *Atomistic Modeling of Cation Transport in the Passive Film on Iron and Implications for Models of Growth Kinetics.* Journal of The Electrochemical Society, 2005. **152**(8): p. B271-B276.
7. Cahan, B.D. and Chen, C.-T., *The Nature of the Passive Film on Iron III. The Chemi-Conductor Model and Further Supporting Evidence.* J. Electrochem. Soc., 1982. **129**(5): p. 921-925.
8. Dewald, J.F., *Transient effects in the ionic conductance of anodic-oxide films at high fields.* Journal of Physics and Chemistry of Solids, 1957. **2**(1): p. 55-66.
9. El Miligy, A.A., Geana, D., and Lorenz, W.J., *A theoretical treatment of the kinetics of iron dissolution and passivation.* Electrochimica Acta, 1975. **20**(4): p. 273-281.
10. Ahn, S. and Kwon, H., *Diffusivity of point defects in the passive film on Fe.* Journal of Electroanalytical Chemistry, 2005. **579**(2): p. 311-319.
11. Young, L., *The Theory of Formation of High Resistance Anodic Oxide Films.* Can. J. Chem., 1959. **37**: p. 276-285.
12. Chao, C.Y., Lin, L.F., and Macdonald, D.D., *A Point Defect Model for Anodic Passive Films III. Impedance Response.* J. Electrochem. Soc., 1982. **129**(9): p. 1874-1879.
13. Pagitsas, M., Diamantopoulou, A., and Sazou, D., *A point defect model for the general and pitting corrosion on iron|oxide|electrolyte interface deduced from current oscillations.* Chaos, Solitons & Fractals, 2003. **17**(2-3): p. 263-275.
14. Fromhold, J., A. T., *Theory of Metal Oxidation*. Defects in Crystalline Solids, ed. A. S., R. Gevers, and J. Nihoul. Vol. 9. 1976, Amsterdam: North-Holland Publishing Company.
15. Young, L., *Anodic Oxide Films.* Transactions of the Faraday Society, 1955: p. 1251-1260.
16. Fehlner, F.P. and Mott, N.F., *Low-Temperature Oxidation.* Oxidation of Metals, 1969. **2**(1): p. 59-99.
17. Fehlner, F.P. and Mott, N.F., *Reply to M. J. Pryor's discussion of low-temperature oxidation.* Oxidation of Metals (Historical Archive), 1971. **3**(3): p. 275-277.

18. Fehlner, F.P., *Oxidation at low temperatures.* Philosophical Magazine B, 1985. **52**(3): p. 729-738.
19. Bean, C.P., Fisher, J.C., and Vermilyea, D.A., *Ionic Conductivity of Tantalum Oxide at Very High Fields.* Physical Review, 1956. **101**: p. 551.
20. Cahan, B.D. and Chen, C.-T., *The Nature of the Passive Film on Iron II. A-C Impedance Studies.* J. Electrochem. Soc., 1982. **129**(3): p. 474-480.
21. Chen, C.-T. and Cahan, B.D., *The Nature of the Passive Film on Iron I. Automatic Ellipsommetric Spectroscopy Studies.* J. Electrochem. Soc., 1982. **129**(1): p. 17-26.
22. Frenkel, J., Z. Phys., 1926. **35**: p. 652.
23. MacDougall, B., *Interpretation of Log i-Log t Relationships for Nickel Passivation.* J. Electrochem. Soc., 1983. **130**: p. 114.
24. Chao, C.Y., Lin, L.F., and Macdonald, D.D., *A Point Defect Model for Anodic Passive Films I. Film Growth Kinetics.* J. Electrochem. Soc., 1981. **128**(6): p. 1187-1194.
25. Lin, L.F., Chao, C.Y., and Macdonald, D.D., *A Point Defect Model for Anodic Passive Films II. Chemical Breakdown and Pit Initiation.* J. Electrochem. Soc., 1981. **128**(6): p. 1194-1198.
26. Wagner, C., J. Electrochem. Soc., 1952. **99**: p. 346C.

Chapter 3

Deriving a Point Defect Model

3.1 Abstract

Almost all studies on the formation of passive oxide films have arrived at the conclusion that point defects are responsible for the properties exhibited by the films. This includes the early stages of film formation to the steady-state measurements of thick films (on an atomic scale). The underlying mechanisms for describing currents, thicknesses, impedances, and structures are based firmly on the defect chemistry of the oxide. However, an exact description of the structure and properties of the passive film on iron is still a matter of disagreement today. Iron oxides are capable of producing a plethora of point defects under various formation conditions (i.e. cation interestitials, cation vacancies, oxygen vacancies, and different cation oxidation states). This makes it difficult to identify a single defect type as being responsible for the incredible variety of properties exhibited by passive iron over a wide range of formation conditions. However, it is due to these difficulties that the research surrounding iron oxide continues to be of great interest. This section will attempt to discuss applying one version of a point defect model to implicitly show which defects must be present at various potentials over the passive range.

3.2 A General Point Defect Model

Since Frenkel first suggested a defect-type model [1] by claiming that charged defects were responsible for current conduction in oxide films, many others have continued with the concept. In fact, the so called High Field Models (HFM) [2-5] are really defect models that allow high fields to be present across the oxide film. The Battaglia-Newman [6] model discussed in section **2.2.6** is a point defect model. However, it was not until the 1980's that the term, point defect model, began to be applied to describe the oxidation of metals in aqueous solutions. Chao and Macdonald proposed that the electric field strength in the oxide is a constant due to Esaki tunneling [7-9] and officially termed the model "The Point Defect Model" (PDM). The idea of a constant electric field is the major concept that sets the PDM apart from the HFM, as well as the prediction of true steady-state conditions. Since the introduction of the PDM, many researchers have adapted the concepts suggested by Macdonald and have modified the model to describe the anodic oxidation of metals [10-18]. Two versions of the PDM will be discussed briefly here before describing a more general PDM that will be used in this work.

Due to the complexity of the PDM, many researchers have sought to simplify the model to make it more "user-friendly"[13-15]. In doing so, one risks the chance of neglecting terms, or reactions, which can have a profound effect on the model predictions. Krishamurthy's model attempts to describe the film growth rate as related to

a vacancy flux through the film. The model was developed to provide better information on the interfacial reaction kinetics. However, the reactions used were not truly elementary reactions which make it impossible to describe the kinetics correctly as was determined by Hendy [19] when testing the validity of models based on previous structure studies [20]. Therefore, a comprehensive model should begin with the elementary interfacial reactions.

Other models incorporate equivalent circuits and other mechanisms that aid in fitting the model to the data. While this approach does yield better fits, it loses the ability to accurately describe the physical mechanisms involved. A very eloquent and in depth study was performed on iron by Bojinov and workers [10, 21, 22] to better understand the influence of electronic conductivity on the film's impedance. Bojinov first measured the film's impedance with an iron working electrode and an iridium counter electrode. Then, through a carefully thought-out and beautifully implemented set of experiments, Bojinov was able to measure the electronic impedance due to the film. To begin Bojinov measured the impedance of two iridium probes in contact to determine if the oxide formed on Ir contributed to the measured impedance (it did not). Next, it was found that a maximum pressure could be applied to an iron oxide layer in order to reduce the contact resistance while preventing the rupture of the oxide. To avoid applying too much pressure and rupturing the film, Bojinov cleverly measured the yield stress of the oxide film and used pressures safely below this limit for the experiments. Finally, the iridium probe was pressed against the oxidized iron sample (in solution) and another impedance measurement was made.

The experiments measured both the ionic and electronic impedances of the film. Bojinov then derived a very in depth model accounting for both types of impedances. The model yielded very nice fits to the impedance data. However, in the end, time constants were introduced for various frequency ranges to allow for the fits. Although these time constants can be explained to be valid based on different relaxation mechanisms (dependent on the frequency range), they introduce an empirical artifact to the model. This artifact helps to conceal, or blur, the "true" physical characteristics of the film. Therefore, a general PDM to describe the oxidation of iron will be presented and discussed next.

This general PDM will be used as a starting point to describe the oxidation of iron in aqueous solutions. Then, in the next chapter, experimental data will be used to aid in the deployment of the PDM to describe the oxidation mechanisms occurring on iron. The end goal is to use the model to predict the damage incurred on iron due to general corrosion.

Before describing the PDM being used in this work, it should be noted that the original PDM as proposed by Chao and Lin [7, 8, 23] relates the impedance of the film to the diffusion of charged defects through the film. Because the diffusion of defects through the film is unlikely to be the rate-determining step, one must consider the reaction kinetics (involving defect formation/annihilation) at the interfaces to be the rate-determining mechanism(s). Therefore a PDM, accounting for the reaction kinetics, was derived by Jun Liu to describe the impedance of the film [24]. All derivations of the PDM in this thesis are variations of Liu's derivation, which was originally derived by

Macdonald in unpublished work on iron (and by Macdonald and Smedley [25-27] for other metals).

To begin, a PDM should account for all reactions involving the creation/annihilation of defects as well as any electrochemical reactions involved with charge transfer. For simplicity it will be assumed that the oxide formed on iron is a single layer oxide. In addition, as will be discussed in the experimental section, chelating agents can be added to the solutions to prevent the formation of an outer precipitation layer. The thickness of the oxide formed on iron in aqueous solutions has been measured using many techniques [6, 11, 12, 22, 28-35] and the various findings indicate the film to be between 1-6 nm in thickness.

Because the oxide is so thin, another basic assumption to begin with is that electronic conduction through the oxide can be considered to be very fast. Both tunneling and "electron-hopping" are possible mechanisms for electron conduction in the thin passive oxide layers [36-39]. Furthermore, ionic conduction through the film is viewed to be fast due to the highly defective structure and the thickness. Again, these are assumptions to begin the modeling process. To better account for ionic conduction, a Warburg impedance can be applied as will be discussed later.

Ignoring the electronic and ionic conduction through the film leads to the conclusion that the oxide film impedance can be attributed to the reaction rates themselves. Therefore, impedance due to electronic conduction through the film is non-existent or negligible. This contradicts Bojinov's findings, but the assumption is being made to simplify the starting point for model development. Further support for neglecting the contribution from electronic conduction can be found in Fromhold's

consideration of thin oxide film formations [36]. In his book, Fromhold indicates that for very thin films (under 5 nm) the electronic conduction is mainly due to tunneling and is generally considered to be a few orders of magnitude larger than the ionic conduction [36]. Therefore, the rate-limiting mechanisms for oxide formation, growth, and destruction can be viewed to be governed by the reactions responsible for film formation and growth. For this to be possible in a model, there must be a reaction involving the formation of new lattice structure sites and a reaction involving the destruction of lattice structure sites. For a film to achieve a steady-state, the reaction rates for these two reactions must be equal. Once the lattice structure non-conservative reactions achieve the same rates, the film will be at steady-state and the defect concentrations will be determined by these rates. Although the reaction rates are the same at steady-state, the rate constants may differ unless the rate constant for each of the reactions have the same units. A more detailed description of this concept is provided in the following section.

The overall understanding so far is that any reactions involving defects and electrons as related to film formation and growth must be present in order to account for oxide formation and growth. Therefore, the following defects have been considered for the oxidation of iron: cation vacancy ($V_{Fe}^{\chi-}$), cation interstitial ($Fe_i^{\chi+}$), anion vacancy (V_O^{2+}). The notation in parentheses is referred to as the Kröger-Vink notation and is the popular notation used in defect chemistry. The *V* stands for a vacancy, the subscripts represent the type of vacant lattice site (i.e. the Fe subscript means that it is a vacant iron site). The notation using the element (in this case Fe) and the subscript *i* is used to represent an interstitial. The superscripts, along with the +/- sign, represent the charge associated with that particular defect. Notice for the iron vacancy, χ was used instead of

an actually charge number. This is because iron can exist in multiple oxidation states. Therefore, knowing the oxidation state(s) present in iron oxide could help to further simplify the number of reactions/unknowns in the model (discussed later). An oxygen vacancy has a charge of plus two associated with it because oxygen has one stable oxidation state for the conditions being studied. Oxygen interstitials are not considered in this work because the size of an oxygen ion is so large that it is a physical impossibility for it to be present in the low temperature systems being considered in this paper. A very basic 2-D diagram is shown in Figure **3-1** to aid in visually showing the various types of defects. The added AB (A and B represent two elements) in the diagram represents the formation of new structure sites and would represent film growth. Whereas, a missing pair of anion-cation sites would represent film destruction.

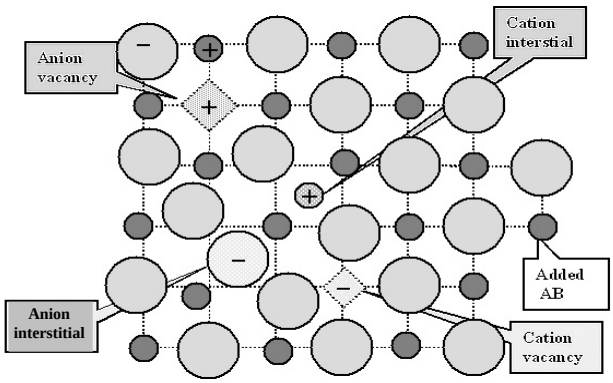

Figure **3-1**: A 2-D view of the various vacancies which can form within a crystal structure.

It is important to point out that in an ionic crystalline structure, such as that depicted in Figure **3-1**, the overall or net charge associated with the material is zero. This is because all of the positive charge associated with the cation lattice is equal to the sum

of all of the negative charge associated with the anion lattice. Consequently, a vacancy (which is a missing charged ion) is understood to have a charge equal to and opposite that of the ion. To illustrate this better, Fig. 3 shows that an anion vacancy has a positive charge associated with it and a cation vacancy has a negative charge. This can easily be understood because a "perfect" structure, one in which every lattice site is occupied by the proper ion, has a net charge of zero. Therefore, if an ion is missing, the overall charge associated with the structure is minus the missing charge (i.e. a missing O^{2-} ion would correlate to a 2+ oxygen vacancy). Interstitial ions are extra ions within the structure and their charge would simply be the same as that of the ion (i.e. a Fe^{3+} interstitial represents a charge of 3+).

All of these defects are referred to as atomic/ionic point defects in a crystalline material because an atom/ion is missing, out-of-place, or replaced by an impurity atom/ion. Another common and well-known type of defect is an electronic defect. This type of defect occurs when an electron is moved from a valance band to the conduction band within a crystalline material and it is the major concept behind semiconductors. An electron in the conduction band has a charge of 1- and a hole in the valence band has a charge of 1+. In metals and other good conductors, electron-hole pairs need not form because the conduction band is already occupied by electrons. On the other hand, the oxide formed on iron exhibits semi-conductive behavior [40].

If we look at the electronic defect reactions shown in equations Eq. **3.1,** Eq. **3.2,** and Eq. **3.3,** it can be seen that the defects corresponding to n-type behavior involves either oxygen vacancies and/or metal interstitials. The reaction responsible for p-type behavior involves metal vacancies as shown in Eq. **3.3**.

$$V_O^x \leftrightarrow V_O^{\bullet\bullet} + 2e^- \quad \textbf{3.1}$$

$$M_i^x \leftrightarrow M_i^{\bullet} + e^- \quad \textbf{3.2}$$

$$V_M^x \leftrightarrow V_M^{\chi-} + 2h^{\bullet} \quad \textbf{3.3}$$

Essentially, what Eq. **3.1** is showing is that a positive oxygen vacancy formed in the structure acts as an electron trap (i.e. electrons in the conduction band that are in the vicinity of a positive vacancy will become "trapped" in it). The metal interstitial shown in Eq. **3.2** behaves in nearly the same way. When a potential is applied across the film, the trapped electrons will be promoted back to the conduction band and the electronic conduction is believed to occur through electronic hopping from defect to defect. The energy required to form electronic defects in iron oxide has been estimated to be around 0.14 eV to 0.18 eV [41], which makes electronic conduction more favorable, but dependent on defect concentrations.

3.2.1 All-inclusive PDM for Iron

Based on the above discussion, Figure **3-2** displays a diagram of a PDM that accounts for the reactions associated with each defect type (see the figure caption for description). This reaction set accounts for every defect type and for the forward and

reverse reaction directions. These concepts were all put forth in earlier work on a PDM by Macdonald [42, 43] and Jun Liu [24]. The reactions are shown relative to the interface at which they occur. If electronic/ionic current through the film is not considered to be the limiting mechanism, then the reaction rate(s) themselves must be limiting.

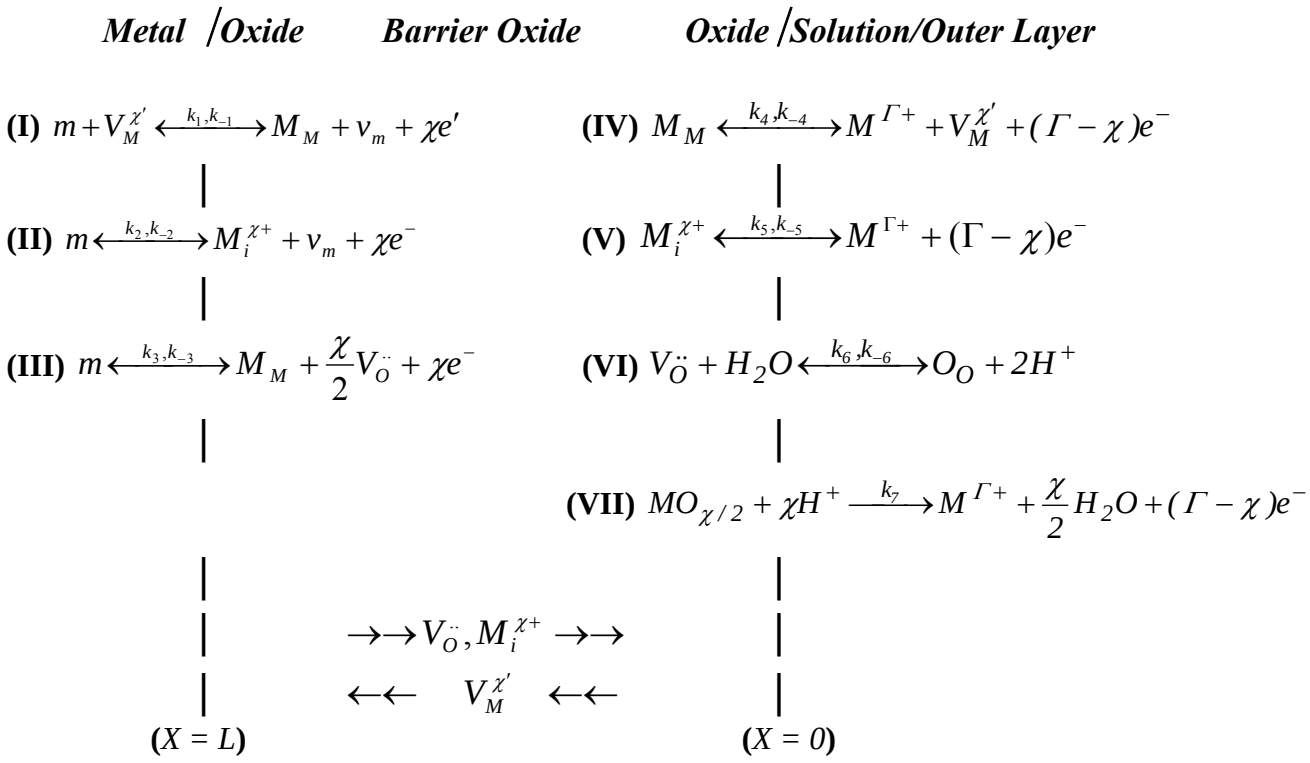

Figure **3-2**: Schematic of physiochemical processes that occur within a passive film according to the PDM. The metal/oxide and the oxide/solution interfaces are depicted by the dashed lines and the reactions are located at the interface where they occur. The oxide/solution interface is defined as X=0 and the metal/oxide interface is defined as X=L, where L is the oxide film thickness. Using Kröger-Vink notation: m = metal atom on a metal lattice site, v_m = vacancy in metal phase, M_M = metal cation on cation site in oxide, O_O= oxygen ion on an anion site in oxide, $V_M^{\chi'}$ = cation vacancy in oxide, $V_O^{\cdot\cdot}$= oxygen vacancy in oxide (the two dots represent that an oxygen vacancy has a charge of 2+), $M_i^{\chi+}$= interstitial cation in oxide, $M^{\Gamma+}$= metal cation in solution during the film growth. The oxidation state of the ions/vacancies are labeled as Γ and χ (i.e. for an Fe^{2+} interstitial in the film, χ = 2; for an Fe^{3+} ion in solution, Γ=3). Cation vacancies ($V_M^{\chi'}$) are produced at the film/solution interface and are consumed at the metal/film. Likewise, anion ($V_O^{\cdot\cdot}$) vacancies are formed at the metal/oxide interface and are consumed at the oxide/solution. Consequently, the fluxes of cation vacancies and anion vacancies are in the directions indicated. The reactions with two-way arrows show that the reactions can occur in the forward or reverse direction. The forward and reverse reaction rates are k_i and k_{-i}, respectively (i = reaction number).

This model is somewhat complicated to grasp by just looking at the diagram, so it will be explained here in greater detail. To better illustrate how the model works, reactions will be grouped into sets of two. One reaction (rxn) is responsible for the defect

formation and the other is responsible for the defect "consumption". All rxns in Figure **3-2** can occur in forward or reverse directions as noted by the two-way arrows. Only rxn VII is considered to proceed in the forward direction.

Rxn IV shows a metal cation in the oxide film dissolving into solution and leaving behind a metal cation vacancy in the film. The difference in the oxidation states between the cation in the film and in the solution will lead to the release of electrons. If the oxidation state is the same in both phases, no electrons will be released (i.e. if Γ is equal to χ). The metal cation vacancy can diffuse through the film, where it is "consumed" by rxn I. In rxn I a metal atom in the metal phase is oxidized and diffuses to occupy the cation vacancy site within the oxide. In doing so, a metal vacancy is formed within the metal phase and it can diffuse into the bulk metal (a metal vacancy has no charge associated with it).

Rxn II depicts the formation of a metal cation interstitial via the oxidation of a metal atom in the metal, which moves to occupy an interstitial site in the oxide lattice. The interstitial then diffuses through the film to the barrier layer/solution interface, where the metal cation can dissolve into solution as shown in rxn V. Rxn V shows a metal interstitial oxidizing prior to entering the solution. As in the previous set of rxns, if the oxidation state does not change, no electrons will be released by rxn V (i.e. if Γ is equal to χ).

Rxn III describes the formation of new metal oxide, where the oxide is seen as growing into the metal phase. This rxn is in good agreement with radioactive tracer experiments that show that the oxide does grow *into* the metal [12]. According to the PDM, this occurs by the oxidation of a metal atom at the metal/oxide interface. The

metal cation is now seen as occupying a newly formed cation site within the metal oxide. To account for the overall charge balance within the oxide structure (as mentioned earlier), when a new cation lattice site is formed, a new anion lattice site must also form. Consequently a new anion lattice site forms on the oxygen lattice and is represented by the oxygen vacancy in rxn III. The oxygen vacancy can now diffuse through the lattice to the oxide/solution interface, where it reacts with a water molecule in solution to yield an occupied oxygen lattice site and hydrogen ions as shown in rxn VI.

Film dissolution takes place by means of rxn VII. In this rxn the metal oxide reacts with the hydrogen ions in solution to form an aqueous metal cation and a water molecule. By doing so the two lattice sites are destroyed and the oxide becomes thinner. Rxn VII is depicted as only occurring in one direction because the oxide is understood to grow into the metal (not the solution). If the reaction was reversed, the oxide would be growing into the solution and this would be contradictory to the current understanding that the oxide grows into the metal as mentioned previously.

Out of the seven rxns discussed here, only rxn IV and rxn VII are lattice non-conservative. Rxn IV shows the formation of new oxide lattice sites which grow into the metal and rxn VII accounts for the destruction of oxide lattice sites via oxide dissolution. If the lattice sites are forming and dissolving at the same rates, the oxide film is in a steady-state. Therefore, a steady-state thickness and current would exist.

A model can be derived to account for the impedance of the oxide film in terms of the reaction rates. The kinetic parameters used to describe the reaction rates can then be used to calculate the transient/steady-state passive layer thickness and the current (which directly relate to the corrosion rate) as a function of pH, electrical potential, and

temperature. However, with this many reactions the model becomes extremely complicated. In order to make the model simpler, some reactions can be ignored if it could be shown that certain defects are dominant and that others are highly unlikely to occur. Two methods can be applied to determine this information. An obvious one is looking at the thermodynamics of the reactions themselves and the other is to apply experimental techniques that can provide some insight into the electronic character of the oxide film. The next chapter applies some thermodynamic data and some experimental evidence for further simplifying the model.

3.3 References

1. Frenkel, J., Z. Phys., 1926. **35**: p. 652.
2. Verwey, J.W., *Electrolytic Conduction of a Solid Insulator at High Fields.* Physica, 1935. **2**: p. 1059.
3. Cabrera, N. and Mott, N.F., *Theory of the Oxidation of Metals.* Reports in Progress of Physics, 1949. **12**: p. 163.
4. Bean, C.P., Fisher, J.C., and Vermilyea, D.A., *Ionic Conductivity of Tantalum Oxide at Very High Fields.* Physical Review, 1956. **101**: p. 551.
5. Burstein, G.T. and Davenport, A.J., *The Current-Time Relationship during Anodic Oxide Film Growth under High Electric Field.* J. Electrochem. Soc., 1989. **136**(4): p. 936-941.
6. Battaglia, V. and Newman, J., *Modeling of a Growing Oxide Film: The Iron/Iron Oxide System.* J. Electrochem. Soc., 1995. **142**(5): p. 1423-1430.
7. Chao, C.Y., Lin, L.F., and Macdonald, D.D., *A Point Defect Model for Anodic Passive Films I. Film Growth Kinetics.* J. Electrochem. Soc., 1981. **128**(6): p. 1187-1194.
8. Chao, C.Y., Lin, L.F., and Macdonald, D.D., *A Point Defect Model for Anodic Passive Films III. Impedance Response.* J. Electrochem. Soc., 1982. **129**(9): p. 1874-1879.

9. Tsu, R. and Esaki, L., *Tunneling in a finite superlattice.* Appl. Phys. Lett., 1973. **22**(11): p. 562-564.
10. Beverskog, B., et al., *A mixed-conduction model for oxide films on Fe, Cr and Fe-Cr alloys in high-temperature aqueous electrolytes--II. Adaptation and justification of the model.* Corrosion Science, 2002. **44**(9): p. 1923-1940.
11. Ahn, S.J. and Kwon, H.S., *Effects of solution temperature on electronic properties of passive film formed on Fe in pH 8.5 borate buffer solution.* Electrochimica Acta, 2004. **49**(20): p. 3347-3353.
12. Ahn, S. and Kwon, H., *Diffusivity of point defects in the passive film on Fe.* Journal of Electroanalytical Chemistry, 2005. **579**(2): p. 311-319.
13. Krishnamurthy, B., White, R.E., and Ploehn, H.J., *Non-equilibrium point defect model for time-dependent passivation of metal surfaces.* Electrochimica Acta, 2001. **46**(22): p. 3387-3396.
14. Krishnamurthy, B., White, R.E., and Ploehn, H.J., *Electric field strength effects on time-dependent passivation of metal surfaces.* Electrochimica Acta, 2002. **47**(15): p. 2505-2513.
15. Krishnamurthy, B., White, R.E., and Ploehn, H.J., *Simplified point defect model for growth of anodic passive films on iron.* Electrochimica Acta, 2002. **47**(20): p. 3375-3381.
16. Castro, E.B., Vilche, J.R., and Oliveira, C.L.F., *Comparative EIS study of passive layers formed on iron and iron-chromium alloys.* Materials Science Forum Proceedings of the 5th International Symposium on Electrochemical Methods in Corrosion Research - EMCR'94. Part 2 (of 2), Sep 5-8 1994, 1995. **192-194**(pt 2): p. 611-622.
17. Pagitsas, M., Diamantopoulou, A., and Sazou, D., *A point defect model for the general and pitting corrosion on iron|oxide|electrolyte interface deduced from current oscillations.* Chaos, Solitons & Fractals, 2003. **17**(2-3): p. 263-275.
18. Cheng, Y.F., Yang, C., and Luo, J.L., *Determination of the diffusivity of point defects in passive films on carbon steel.* Thin Solid Films, 2002. **416**(1-2): p. 169-173.
19. Hendy, S.C., Laycock, N.J., and Ryan, M.P., *Atomistic Modeling of Cation Transport in the Passive Film on Iron and Implications for Models of Growth Kinetics.* Journal of The Electrochemical Society, 2005. **152**(8): p. B271-B276.
20. Davenport, A.J., et al., *The Structure of the Passive Film That Forms on iron in Aqueous Environments.* Journal of The Electrochemical Society, 2000. **147**(6): p. 2162-2173.
21. Bojinov, M., et al., *Coupling between ionic defect structure and electronic conduction in passive films on iron, chromium and iron-chromium alloys.* Electrochimica Acta, 2000. **45**: p. 2029-2048.
22. Bojinov, M., et al., *Conduction Mechanism of the Passive Film on Iron Based on Contact Electric Impedance and Resistance Measurements.* J. Electrochem. Soc., 2001. **148**(6): p. B243-B250.
23. Lin, L.F., Chao, C.Y., and Macdonald, D.D., *A Point Defect Model for Anodic Passive Films II. Chemical Breakdown and Pit Initiation.* J. Electrochem. Soc., 1981. **128**(6): p. 1194-1198.

24. Liu, J., *Electrochemical emmision and impedance spectroscopies of passive iron and carbon steel*, in *Material Science and Engineering*. 2002, Pennsylvania State University: University Park, PA. p. 170.
25. Macdonald, D.D., Smedley, S.I., and Urquidi-Macdonald, M., J. Electrochem. Soc., 1988. **135**: p. 2410.
26. Macdonald, D.D. and Smedley, S.I., *An electrochemical impedance analysis of passive films on nickel(111) in phosphate buffer solutions.* Electrochimica Acta, 1990. **35**(11-12): p. 1949-1956.
27. Macdonald, D.D. and Smedley, S.I., *Characterization of vacancy transport in passive films using low frequency electrochemical impedance spectroscopy.* Corrosion Science, 1990. **31**: p. 667-672.
28. Ohtsuka, T. and Ohta, A., *Growth of a passive film on iron in a neutral borate solution by three-parameter ellipsometry.* Materials Science and Engineering A, 1995. **198**(1-2): p. 169-175.
29. Azumi, K., Ohtsuka, T., and Sato, N., *SPECTROSCOPIC PHOTORESPONSE OF THE PASSIVE FILM FORMED ON IRON.* Journal of the Electrochemical Society, 1986. **133**(7): p. 1326-1328.
30. Chen, C.-T. and Cahan, B.D., *The Nature of the Passive Film on Iron I. Automatic Ellipsommetric Spectroscopy Studies.* J. Electrochem. Soc., 1982. **129**(1): p. 17-26.
31. Chin, Y.-T. and Cahan, B.D., *An Ellipsometric Spectroscopic Study of the Passive Film on Iron-Potential and Chloride Dependence.* J. Electrochem. Soc., 1992. **139**(9): p. 2432-2442.
32. Schmuki, P., et al., *Passivity of Iron in alkaline solutions studied by in situ XANES and Laser Reflection techniques.* J. Electrochem. Soc., 1999. **146**(6): p. 2097-2102.
33. Stimming, U. and Schultze, J.W., *The Capacity of Passivated Iron Electrodes and the Band Structure of the Passive Layer.* Berichte der Bunsen-Gesellscaft, 1976. **80**(12): p. 1297-1302.
34. Stimming, U., *Photoelectrochemical studies of passive films.* Electrochimica Acta, 1986. **31**(4): p. 415-429.
35. Sato, N. and Kudo, K., *Ellipsometry of the Passivation Film on iron in Neutral Solution.* Electrochimica Acta, 1971. **16**: p. 447-462.
36. Fromhold, J., A. T., *Theory of Metal Oxidation*. Defects in Crystalline Solids, ed. A. S., R. Gevers, and J. Nihoul. Vol. 9. 1976, Amsterdam: North-Holland Publishing Company.
37. Rosso, K.M., Smith, D.M.A., and Dupuis, M., *An ab initio model of electron transport in hematite basal planes.* Journal of Chemical Physics, 2003. **118**(14): p. 6455-6466.
38. Janek, J. and Martin, M., *Electrotransport in Ionic Crystals: II. ADynamical Model.* Ber. Bunsenges. Phys. Chem., 1994. **98**(5): p. 665-673.
39. Wang, L., et al., *Magnetoelectric transport properties of quenched polycrystalline magnetite.* Journal of Magnetism and Magnetic Materials, 1999. **207**(1-3): p. 111-117.

40. Castro, E.B., *Analysis of the Impedance Response of Passive Iron.* Electrochimica Acta, 1994. **39**(14): p. 2117-2123.
41. Alves, V.A. and Brett, C.M.A., *Characterisation of passive films formed on mild steels in bicarbonate solution by EIS.* Electrochimica Acta, 2002. **47**(13-14): p. 2081-2091.
42. Macdonald, D.D., Biaggio, S.R., and Song, H., *Steady-State Passive Films Interfacial Kinetic Effects and Diagnostic Criteria.* J. Electrochem. Soc., 1992. **139**(1): p. 170-177.
43. Macdonald, D.D., *Passivity-the key to our metals-based civilization.* Pure and Applied Chemistry, 1999. **71**(6): p. 951-978.

Chapter 4

Experimental Analysis of the Passive Oxide Formed on Iron

4.1 Abstract

The passive film formed on iron is analyzed with ellipsometry, electrochemcical impedance spectroscopy, AFM, and XPS. The films were grown in a borate buffer solution under potentiostatic conditions within the passive range of iron. It is shown that in the early stages of oxide formation (-0.4 V_{SCE} to 0.0 V_{SCE}) that the impedance is low compared to the later stages of oxidation, indicating either the easy transport of species through the film or that the oxide only partially covers the surface. At 0.0 V_{SCE} the film thickness, as measured by ellipsometry, is approximately 8 Å, which is nearly equal to the lattice parameters for the various oxides believed to be forming on iron in borate solution (γ-Fe_2O_3, Fe_3O_4, or the LAMM phase). XPS analysis shows that the iron species present in the film is almost completely $Fe^{3+}$and that Fe^{2+} comprises less than 10% of the film (the detection limit of the equipment). Therefore, at least 20 % of the Fe^{2+} sites in Fe_3O_4 must be vacant which would most likely give the film a p-type character. The LAMM (no meaning for the acronym is provided by the authors [1]) phase contains mostly iron vacancies as the majority defect, also making the film p-type. However Mott-Schottky analysis shows the film to be an n-type semi-conductor with high levels of

defects. This leads to the conclusion that the passive film formed on iron is most likely similar to γ-Fe_2O_3.

4.2 Introduction

As evidenced by the complexity of the seven reaction model shown in Figure **3-2**, a useful model derived from these reactions, capable of predicting corrosion damage, would be questionable at best. Solving the kinetic equations as set forth by the model leads to a very complex solution. The solution is an over-parameterized set of equations describing the film growth, steady-state thickness, current values, and impedance. It is somewhat difficult to use these equations for making predictions because of the infinite number of solutions that are possible. However, if parameters can be obtained experimentally and inserted into the model, this model can prove to be an incredible tool for making predictions. With that being stated, few parameters were found in literature and only a few can be obtained from various experimental methods. This is most likely the reason that Chao, Lin, and Macdonald [2] used a reverse manner to justify their original PDM (i.e. fitting the model to data and verifying that the fit parameters are sensible).

For this reason this chapter will focus on using the experimental data and some thermodynamic data to better understand the passive iron oxide layer. The ultimate goal is to reduce the number of reactions and/or unknowns that appear in the seven reaction model.

The chapter will begin by discussing the potentiodynamic plot(s) for iron in order to understand what conditions are best for studying the oxide film formed on iron. All experiments were carried out in a borate buffer solution. This particular solution is used extensively in studies involved with the formation process of iron oxide due to the wide potential range over which the oxide is stable. In addition the dissolution of iron in borate buffers is very slow making it possible to achieve accurate measurements for potential-step experiments [1, 3-5]. Ord and De Smet also found that this solution is ideal for making optical measurements [3, 6], which is useful for making ellipsometer measurements.

Ellipsometry is used for two reasons in this work. First it is used as a non-destructive method for measuring film thickness. Second, ellipsometry measurements are used to show that the outer, precipitated layer is prevented from forming through the use of a chelating agent. A chelating agent, Ethylenediaminetetraacetic Acid (EDTA), is used to prevent the formation of the precipitate layer. By removing the precipitate layer, the inner oxide layer, known as the barrier layer, can be studied exclusively. It is generally agreed upon that the barrier layer is responsible for the passive characteristics exhibited by iron.

The potentiodynamic and ellipsometric experiments make it possible to determine the best conditions to grow and study the iron oxide formed in borate buffer solutions. Two types of electrochemical experiments, AC Impedance and Mott-Schottky Analysis, are used to probe the characteristics of the barrier layer. These experiments can yield valuable information pertaining to the electronic nature of the barrier layer and aid in the development of a PDM suitable for describing the passive behavior of iron.

Finally, XPS analysis and AFM are applied to further understand the composition and microstructure of the film. The XPS results will be used in the next chapter to help reduce the number of specie type(s) present in the film. The AFM results, though moot, can be used to quantify the grain sizes and point to the type of diffusion occurring through the film. In addition the obvious and very important finding that a polycrystalline structure is formed helps to negate any notions that the passive film formed on iron is amorphous.

4.3 Experimental

Polycrystalline iron, 99.99% pure, was obtained from Nilaco of Japan. The 2 mm thick plate was cut into 1 cm by 1 cm sections and copper wires were attached with a silver based solder. The samples were then mounted in Hysol, high temperature epoxy. After mounting, the samples were ground with SiC paper, polished with diamond suspensions, followed by a very fine polish with a silica colloidal suspension (0.04 μm). The final RMS roughness, as measured by AFM, was 3.6 nm. The samples were placed in a vacuum furnace and held at 350° C for four hours to help relieve any surface stresses induced by polishing. All experiments discussed in this thesis were performed used this preparation method.

All of the electrochemical experiments were performed using a Solartron 1268 potentiostat connected with a Solartron 1250 frequency response analyzer. The electrochemical cell used to perform the experiments is shown in Figure **4-1** and a picture

of the cell is shown in Figure **4-2**. The cell was designed and built to perform electrochemical and ellipsometric experiments simultaneously. Also, not shown here, a port was built in to allow for the insertion of a Teflon-coated heater for controlling solution temperature. A Luggin probe containing a porous, zirconia frit was attached to the SCE reference electrode. All potentials listed will be with respect to the SCE reference electrode. Eq. **4.1** was used to account for any drift in the SCE potential with temperature. "T" represents the temperature for the experiment and T_{RT} is room temperature.

$$0.241V - \left[0.661\times10^{-3}\left(T - T_{RT}\right)\right] \qquad \textbf{4.1}$$

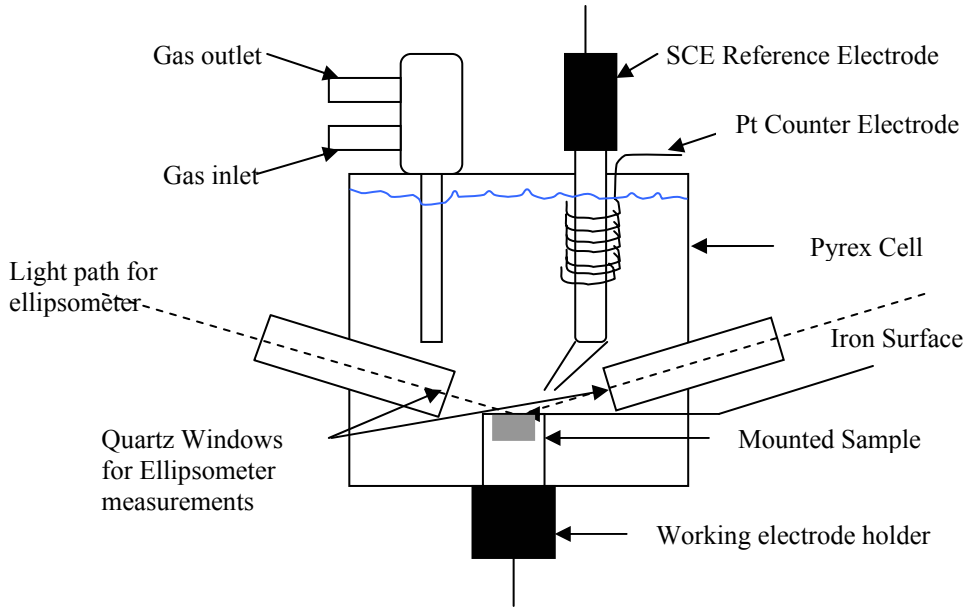

Figure **4-1**: Diagram of the electrochemical cell used in this work. The dashed line is used to represent the path of the light beam from the ellipsometer. The drawing is not to scale and the angle of the incident/reflected light beam is 75° from normal. The quartz windows were mounted precisely 90° to this (though not evident in diagram). Not shown here is the clamp for connecting the upper and lower sections of the cell.

The solution used in most experiments was a pH 8.94 borate buffer. The chemical composition of this solution was 0.3 M H_3BO_3 + 0.075 M $Na_2B_4O_7$ + 0.01 M EDTA. To study the effects due to changes in pH, the concentration of boric acid was altered and NaOH was added to achieve a higher pH value. The solutions were mixed with 18 MΩ cm deionized water obtained from a Millipore system.

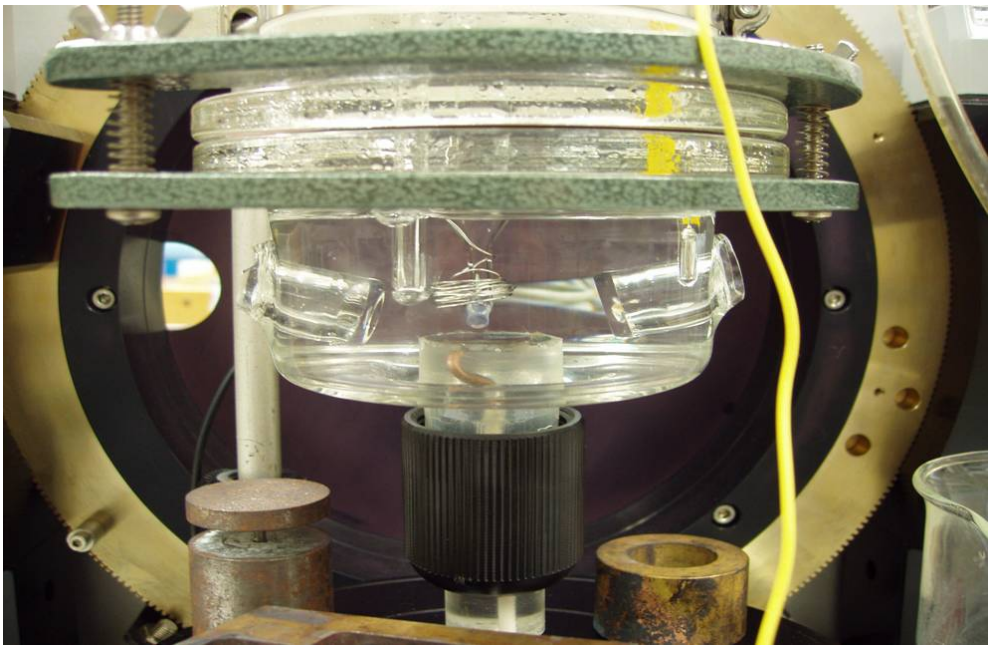

Figure **4-2**: Picture of the electrochemical cell used in these experiments.

Prior to each experiment, high purity Ar gas was bubbled for 30 minutes. After this time, the iron electrode was held at -1 V_{SCE} for two minutes to remove any air-formed oxide. Ellipsometry measurements were made to ensure that the air-formed oxide was removed. The Ar gas was continuously bubbled throughout every experiment and the exhaust was placed in a water-filled beaker to prevent any oxygen from entering the cell.

The above procedure was followed for each experiment and a new sample was used each time. Details of the individual experiments (i.e. ellipsometry, XPS, AFM) will be given in the respective sections to follow. However, the preparation and electrochemical procedure discussed above was applied to prepare each sample for analysis.

4.4 Potentiodynamic Plots for Iron

Potentiodynamic experiments were carried out at three temperatures: 21° C (measured T_{room}), 50° C, and 75° C. It was the hope of the author to make measurements at 90° C to correspond with the temperature of the waste contained in the tanks. However, the reference electrode used for this work was limited to 80° C and the optical constants of the solution were altered too much to make any reasonable ellipsometer measurements at 90° C.

Figure **4-3** displays the anodic polarization curves (potentiodynamic curves) for iron for each temperature. The potentiodynamic plots shown in Figure **4-3** display a wide passive range that varies from roughly -0.4 V to approximately +0.8 V. The increase in the overall current density (both in the active and passive Regions) with temperature is clearly evident and more discussion on this will follow in the proceeding chapter.

The passive range can be separated into three distinct Regions. From the onset of passivation (-0.4 V) to 0.0 V, the current density is slightly larger at room temp. and this is referred to as Region I. From 0.0 V to +0.6 V the current remains nearly constant and

this is referred to as Region II. As the potential increases from +0.6 V to the onset of oxygen evolution (approximately +0.8 V), the current increases slightly before a sudden rise in current due to the oxygen evolution reaction. The last Region, from +0.6 V to +o.8 V is termed Region III.

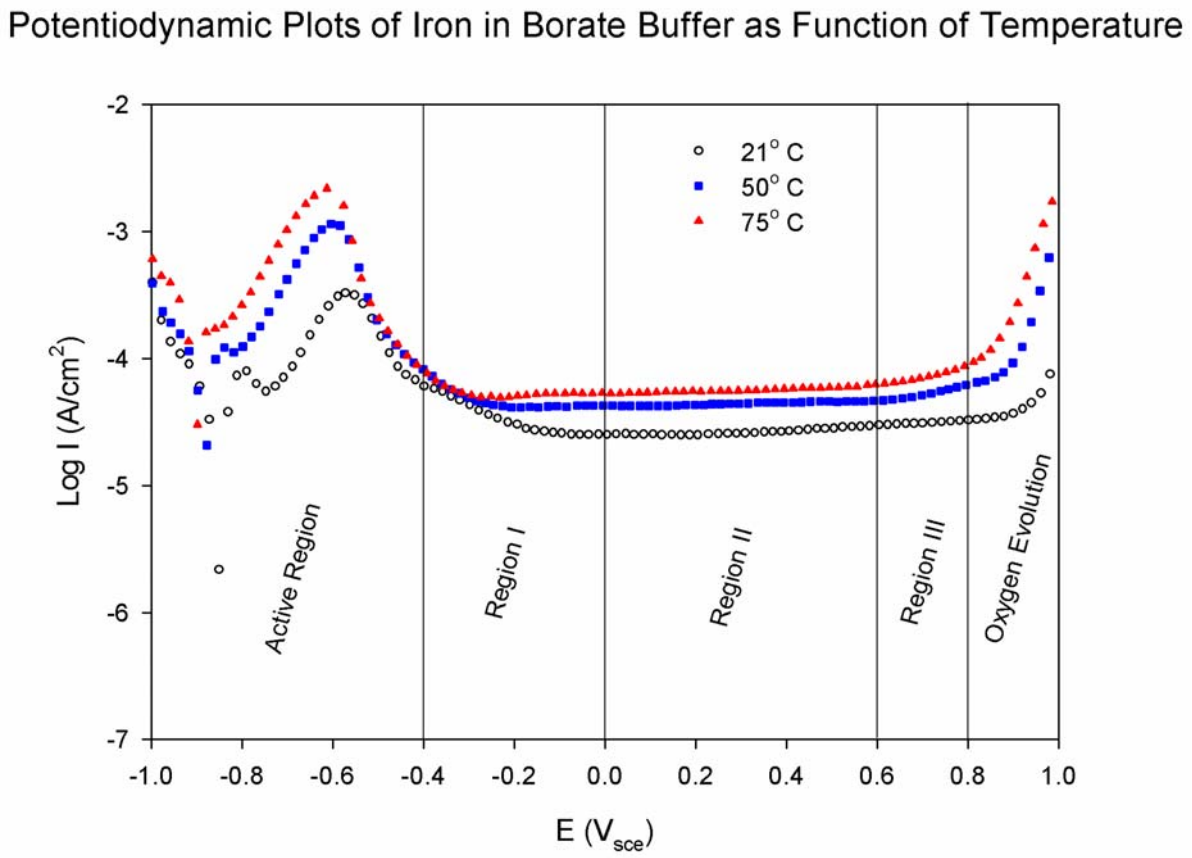

Figure **4-3**: Anodic polarization curves of iron in deaerated borate buffer solution with pH 8.15. The scan rate is 5 mV/sec for each temperature range (Room Temp., 50° C, and 75° C)

Although it is not very visible in Figure **4-3** a second anodic peak occurs at -0.2V in Region I [7, 8]. This peak can be seen as a slight rise in the current in the 75° C plot at approximately +2 V. Many researchers have attempted to explain this peak as the oxidation of Fe^{2+} to Fe^{3+}, which leads to the sudden increase in the current [9-11]. This

approach is thermodynamically reasonable because Fe_3O_4 is the first thermodynamically stable film and contains Fe^{2+} in its structure[12]. Macdougall performed a study where he monitored the Fe^{2+} concentration in the solution as a function of time while holding the potential within the Region I range [11]. While in this potential range, the Fe^{2+} concentration in the solution increased with time. Two reasons for this observation can be provided. First, in this potential range, Fe_3O_4 is the stable phase present in the film and can easily dissolve [13] . Therefore, the formation and dissolution of the magnetite layer leads to the observed increase in the Fe^{2+} concentration in the solution and slightly higher currents. The second reason is to view the oxide formed in this Region as only partially covering the iron surface, thereby making it possible for active dissolution of the iron to occur in exposed areas on the surface [14].

The potentiostatic plot for iron in borate buffer solution at -0.4V is shown in Figure **4-4**. This plot shows that the current density decreases after a few hours to a value in the $\mu A/cm^2$ range. This would indicate that some sort of passive film must be covering the surface and that active dissolution on exposed areas of the iron surface is unlikely. Therefore, the reason for the increase in the Fe^{2+} concentration in the solution must be due to either the dissolution of Fe_3O_4 or diffusion through the film. It is the author's view that magnetite is the stable oxide phase in Region I of the potentiodynamic plot. Magnetite, which contains Fe^{2+}, dissolves more readily than hematite (Fe_2O_3) [13, 15]. This is also evident when considering the steady state currents in Region I and II. A higher steady state current (10^{-6} A/cm^2) is observed for formation potentials in Region I, while the steady state currents in Region II are generally a magnitude lower (10^{-7} A/cm^2). Ellipsometry was used to measure a film thickness in this Region, but no useful data was

obtained due to excess noise in the optical measurements. This noise is being attributed to the dissolution of Fe^{2+} occurring at the surface. XPS work showed that an oxide was formed at – 0.2 V (in Region I), but no XPS analysis was performed on samples treated at – 0.4 V.

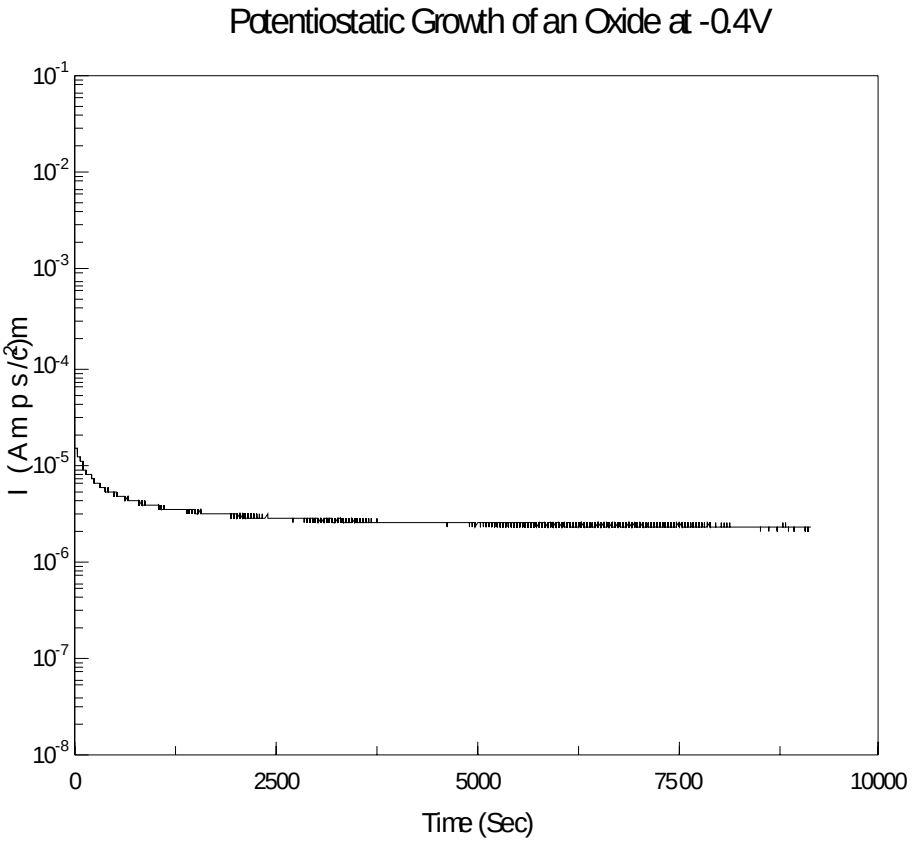

Figure **4-4**: The potentiostatic plot for iron in borate buffer held at -0.4V. The current density reaches a near constant value in the $\mu A/cm^2$ range after a few hours.

The transition from Region I to Region II has been a matter of speculation by researchers for sometime [4, 5, 11, 14, 16-18]. Some view it as the formation of an outer layer of Fe_2O_3 [4] through which ionic conduction is difficult. While others view it as a

mixed phase [12, 18] comprised of both magnetite and hematite or a new phase altogether as proposed by Davenport and workers [1]. Battaglia argues that in Region II, the structure takes on the form of γ-Fe_2O_3, but the presence of Fe^{3+} interstitials and electrons gives it the appearance of Fe_3O_4 [18]. Based on the XPS work described later, the author views the transition from Region I to Region II as an actual phase change from Fe_3O_4 to γ-Fe_2O_3. Due to the phase change, ionic conduction switches to an interstialcy-type of diffusion where Fe^{3+} ions temporarily exist on interstitial and cation lattice sites. Thermodynamic predictions indicate that Fe^{2+} must form first, but only has a substantial concentration very near the iron/oxide interface as is Cahan's view [13]. The reasoning is that any Fe^{2+} formed at the interface cannot diffuse through the film in that oxidation state and must oxidize to Fe^{3+} first for diffusion to occur. Therefore, the overall concentration of Fe^{2+} in the film is very small.

At around 0.2V ellipsometry results indicate the formation of an oxide film on the iron surface with a thickness of approximately 1 nm, which is slightly larger than the 0.84 nm lattice [1] constant for γ-Fe_2O_3. This would indicate that a monolayer of oxide has formed on the surface. The growth of the film will be described in the ellipsometry section. To determine if steady-state conditions were present in this range, potentiostatic experiments were carried out where the potential was held constant for a 24 hour period while the current was measured over time. The potential was stepped from +0.2V to +0.8V in 0.2V increments and held for 24 hours at each potential. From +0.2V to +0.6V, the measured current density was 124 nA/cm^2 with an error in the measurement of ± 12 nA/cm^2. The fact that the current density remained the same over this range indicates

that steady-state (or quasi steady-state) conditions were achieved. This phenomena is predicted by the PDM [19-21] and will be discussed in further detail in the next chapter. At +0.8V the current density doubled to a value of 258 nA/cm^2 ±12 nA/cm^2. Above this potential the current density increased drastically indicating that oxygen evolution began to occur.

The slight increase in current density between +0.6V to +0.8V could possibly be due to the early onset of oxygen evolution, although no bubbles could be seen to form on the surface. To help verify the oxygen activity, thermocalc software was used to calculate the activity of oxygen as a function of potential. The reason for using thermocalc is because the magnetite phase or γ-Fe_2O_3 could be "locked" in as the only stable phase during the calculations (as well as the chemical concentrations in the solution). The results indicate that at approximately +0.6 V_{SCE} the oxygen activity begins to increase slightly at the surface. Although gas bubbles were not visible, the increase in oxygen activity should certainly give rise to an increase in the current. Others suggest that in this range $Fe^{2+} \rightarrow Fe^{3+}$, however, as suggested earlier, this oxidation reaction is understood to take place at around -0.2 V. Based on the Mott-Schottky analysis that is discussed later, the slight increase might possibly be attributed to a switch in the defect type of the film. Due to the changes observed in this potential range, this is considered to be Region III. Although there appears to be another change in the behavior of the film in this Region, it has not been studied in any detail like the transition from Region I to Region II has been. There will be further discussion concerning this in the sections to follow.

4.5 Electrochemical Impedance Spectroscopy

All of the Electrochemical Impedance Spectroscopy (EIS) measurements were made using a 10 mV perturbation to confine the current response to a linear regime. The frequency range was .01 Hz to 10^4 Hz and was limited by the capabilities of the frequency response analyzer. For the present the impedance data are only being used in a qualitative matter to describe the transitions between the three Regions mentioned in section **4.4** . Further analysis of the impedance data, in a quantitative manner, will be undertaken in the next chapter.

All measurements were made on films formed for atleast 24 hrs under potentiostatic conditions. Earlier work on the project showed that larger perturbations cause the system to become non-linear and the data generated is not useful [22]. To ensure that the system was stable, there should be good agreement between the frequency sweep up and down directions. Figure **4-5** and Figure **4-6** display the EIS data for an up and down frequency scan for iron at +0.4V. This value is chosen because it falls near the center of the stable passive Region of interest in this study. As can be seen the agreement is good indicating the stability of the system for these measurements. In addition, all impedance data was tested using the Kramers-Kronig transforms to ensure the validity of the data [23]. Any data that was not Kramers-Kronig consistent was disregarded.

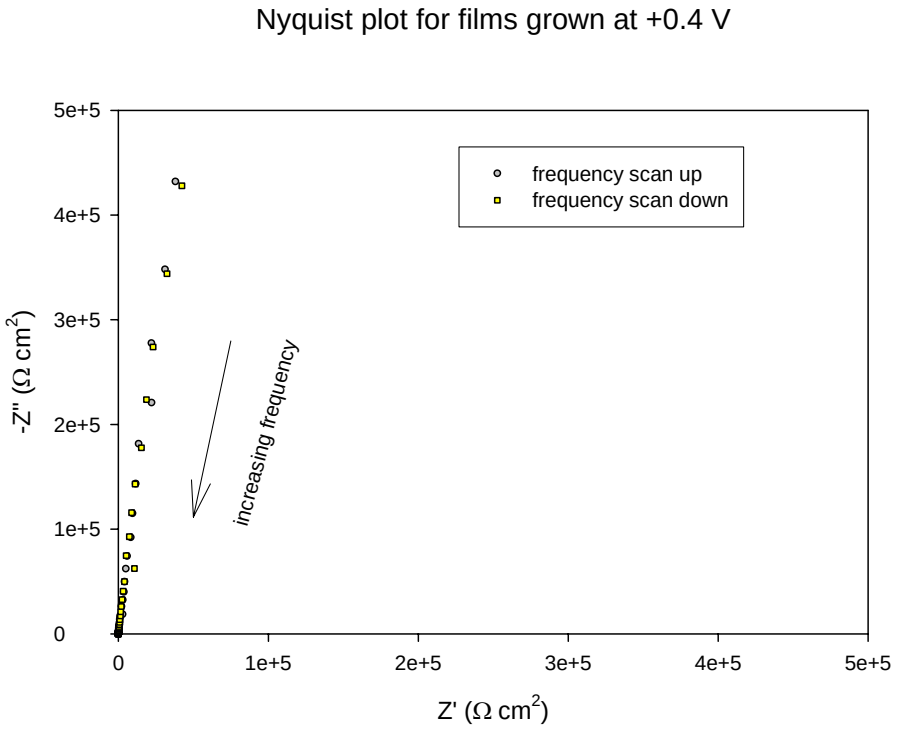

Figure **4-5**: Nyquist plot showing a good agreement between the up and down frequency scan.

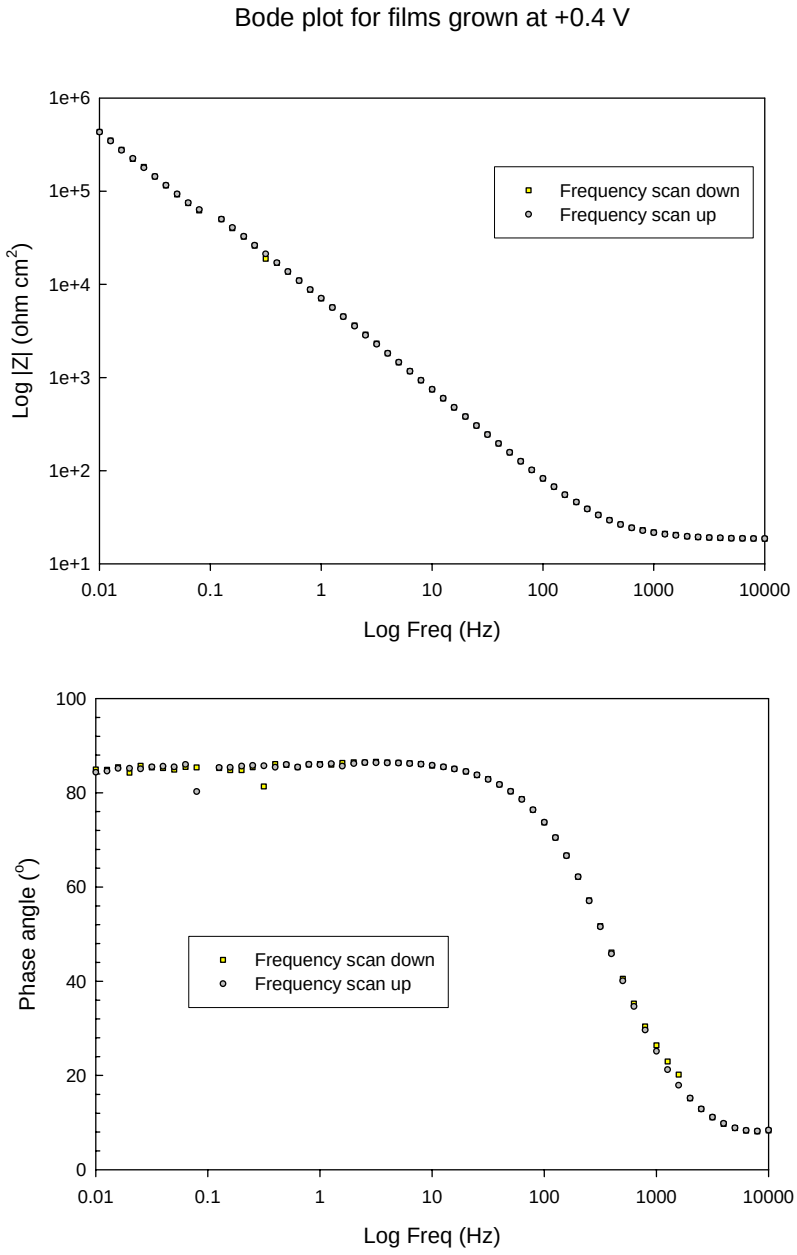

Figure **4-6**: Bode plot showing a good agreement between the up and down frequency scan. The break in the data at a frequency of 0.1 Hz corresponds to the switch in current measurement range of the auto-ranger of the equipment.

To begin, EIS measurements were made at a few potentials across Region I. The Nyquist plots are shown in Figure **4-7** and Bode plots in Figure **4-8**. It can easily be seen that the impedance increases greatly at a film formation potential of 0.0V. This finding is

consistent with the view that the oxide phase changes from the more conductive Fe_3O_4 structure to the less conductive γ-Fe_2O_3 structure.

Figure **4-9** and Figure **4-10** show the impedance measurements for films formed at various potentials across Region II. The impedance does not change dramatically in this range indicating that a single phase is most likely stable over Region II. This is consistent with the suggestion that the γ-Fe_2O_3 structure (or another higher impedance) structure exists over this Region. The small difference in the impedance in the passive range is also in agreement with the predictions of the PDM [22, 24]. Since the electric field strength within the film is viewed to be constant over the passive range, the impedance should be independent of the thickness (or formation potential).

The data for a passive film formed at +0.8V (in Region III) is shown to illustrate the sudden change once in the "new" Region. The cause of this transition will be discussed later. Figure **4-11** and Figure **4-13** show the Nyquist plots for the 50° C and 75° C measurements. Figure **4-12** and Figure **4-14** show the Bode plots for the same temperatures, respectively. The frequency range was scanned from 0.05 Hz to 10000 Hz for these temperatures because the low/high frequency ranges introduced noise into the data. Figure **4-15** and Figure **4-16** show the change in impedance with temperature for films grown at +0.4 V (middle of Region II). The data shown is for the frequency range of 0.1 Hz to 10000 Hz for the sake of comparison. It can be seen that the impedance does drop with the temperature, but the difference between the 50° C and 75° C does not appear to be a too large.

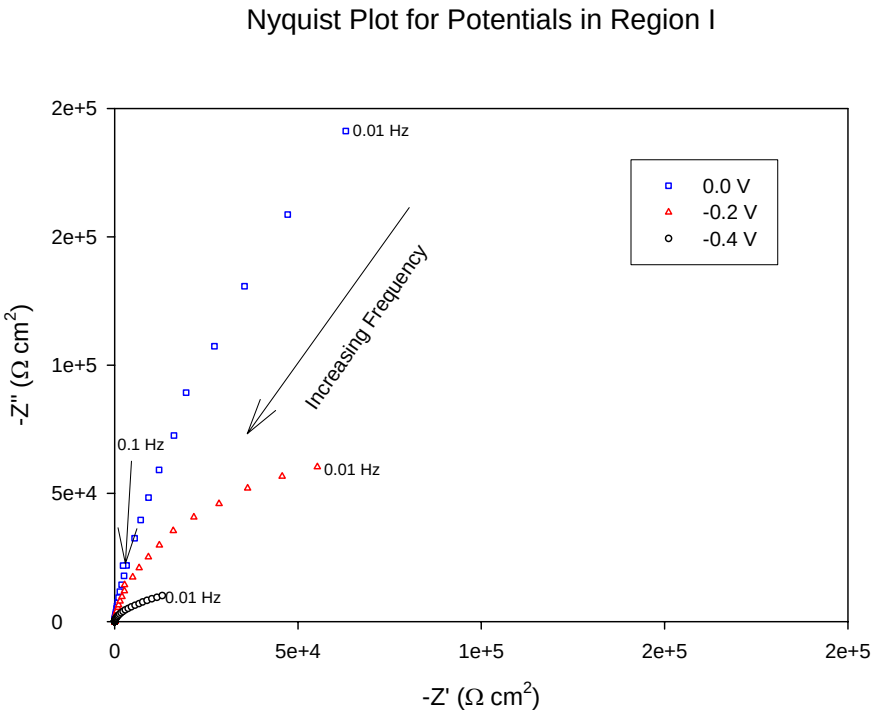

Figure **4-7**: Nyquist plot showing the increase in impedance with the film formation potential across Region I. The measurements were made at -0.4V, -0.2V, and 0.0V. The frequency was scanned in the up direction. The impedance increases greatly at 0.0V. All scans were performed from 0.01 Hz to 10000 Hz.

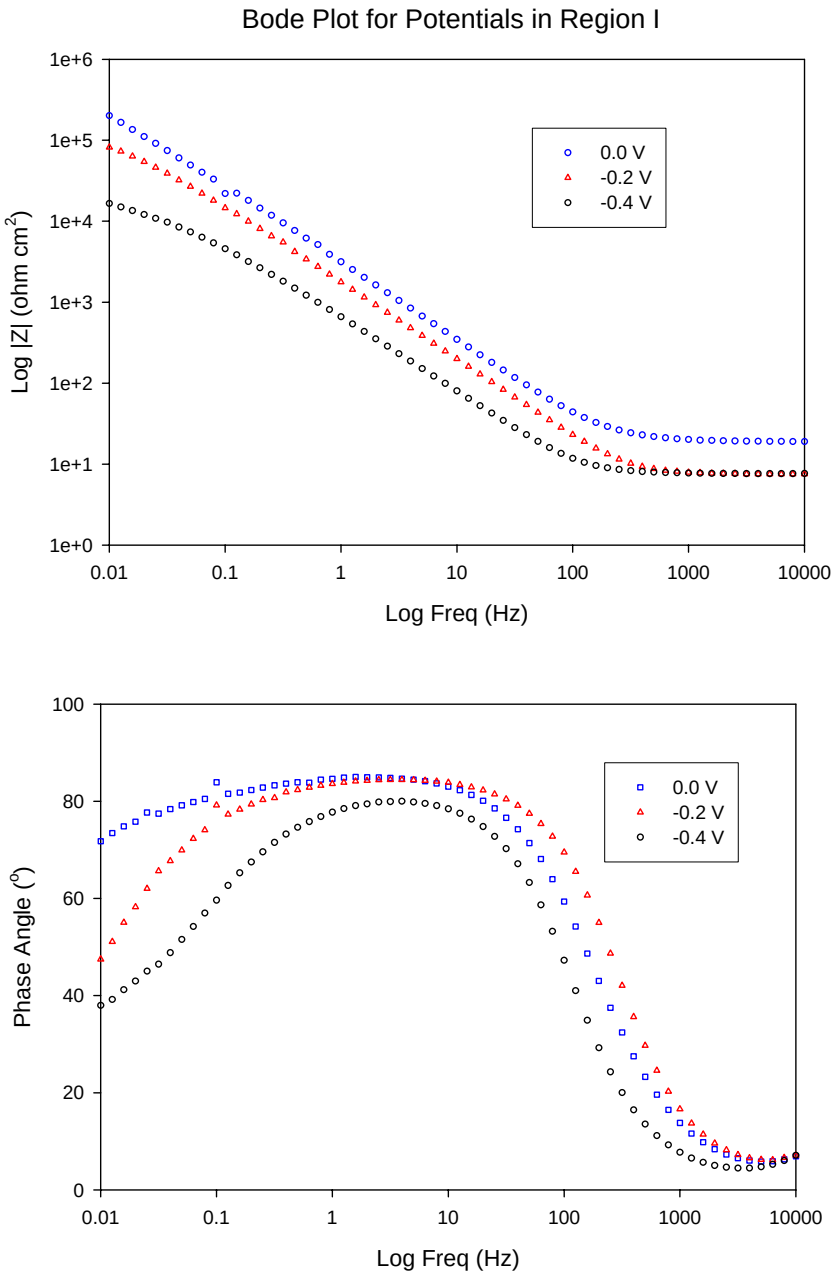

Figure **4-8**: Bode plot showing the increase in impedance with the film formation potential across Region I. The measurements were made at -0.4V, -0.2V, and 0.0V. The frequency was scanned in the up direction. The impedance increases greatly at 0.0V. All scans were performed from 0.01 Hz to 10000 Hz.

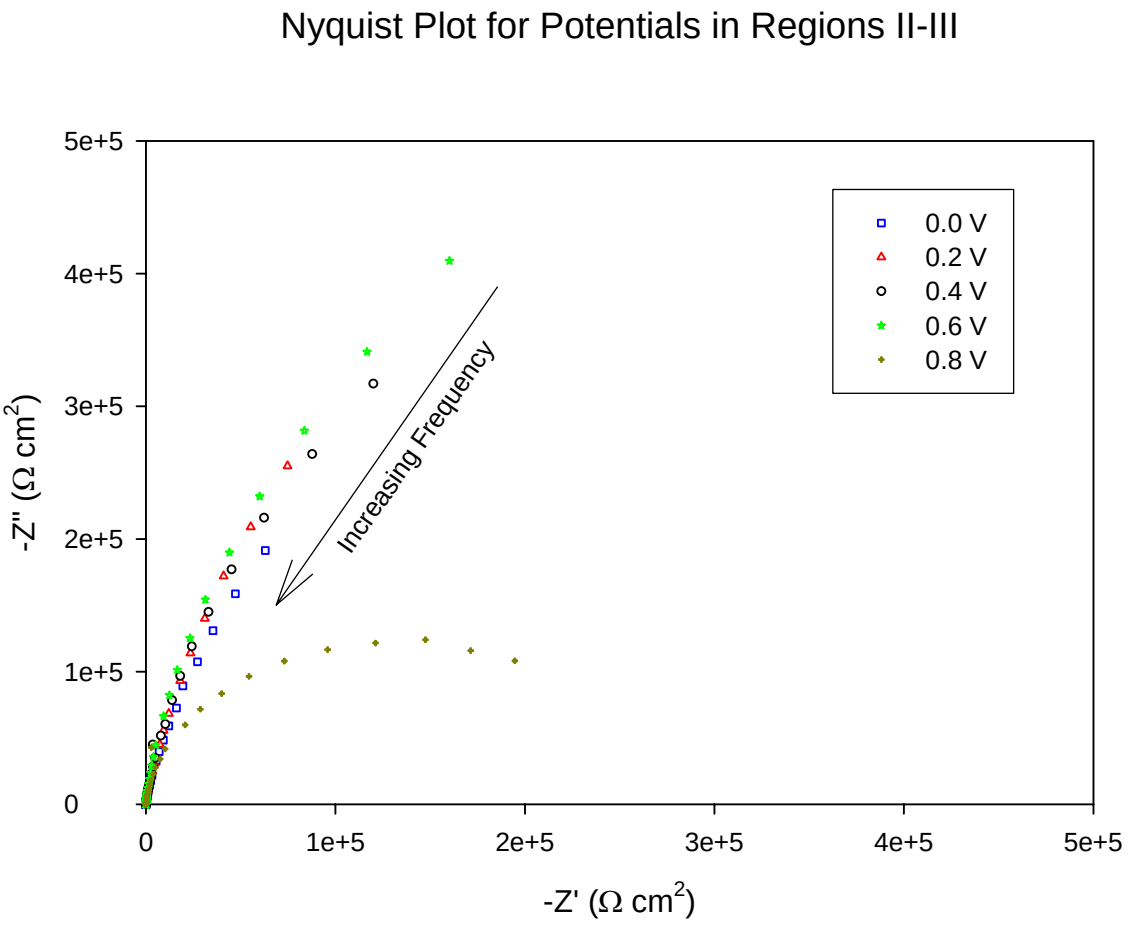

Figure **4-9**: Nyquist plot showing the impedance values over the potential range of Region II. The impedance values for +0.8V are shown to indicate the abrupt change when in Region III.

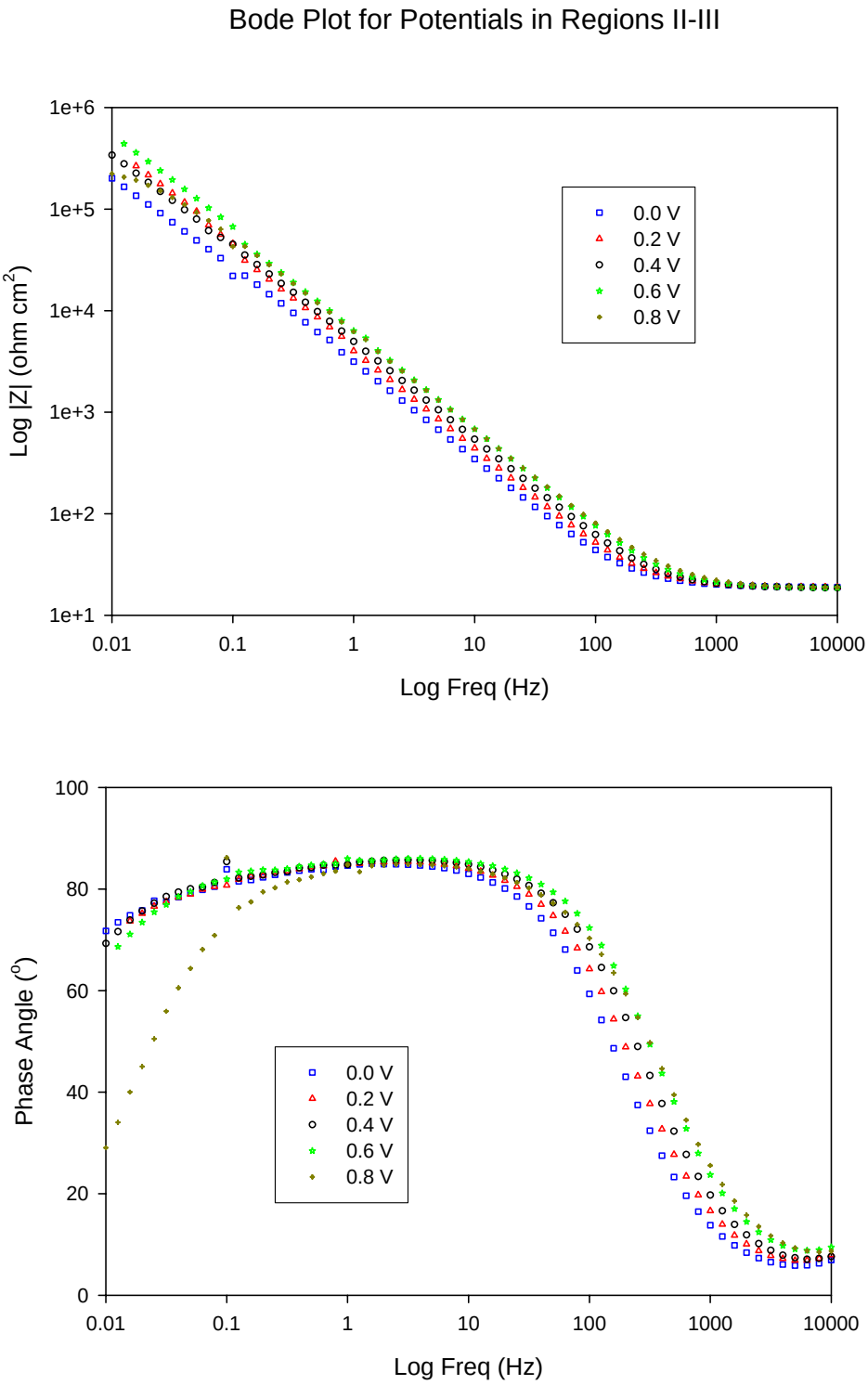

Figure **4-10**: Bode plot showing the impedance values over the potential range of Region II. The impedance values for +0.8V are shown to indicate the abrupt change when in Region III (particularly in the low frequency range).

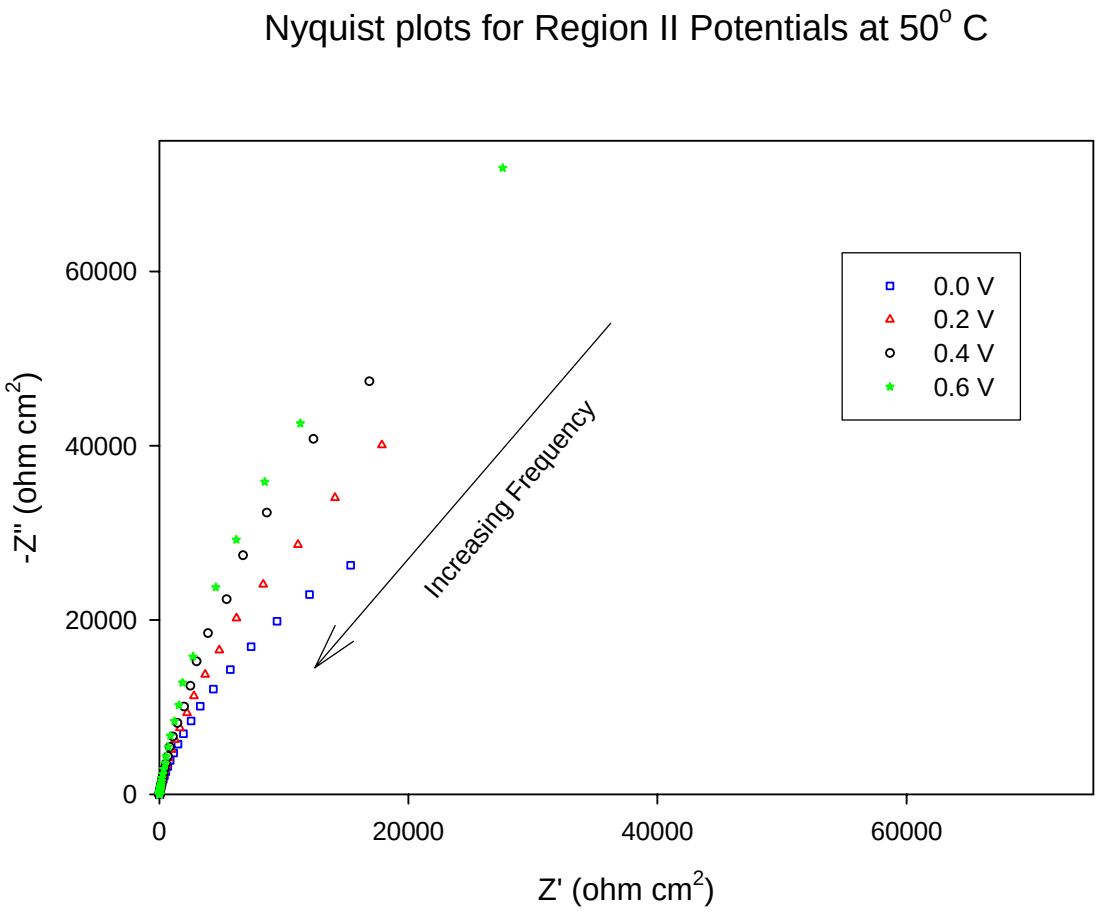

Figure **4-11**: Nyquist plot showing the impedance values over the potential range of Region II for impedance measurements at 50° C. The scans were performed from 10000 Hz to 0.05 Hz because the data at the low/high frequencies were "noisy".

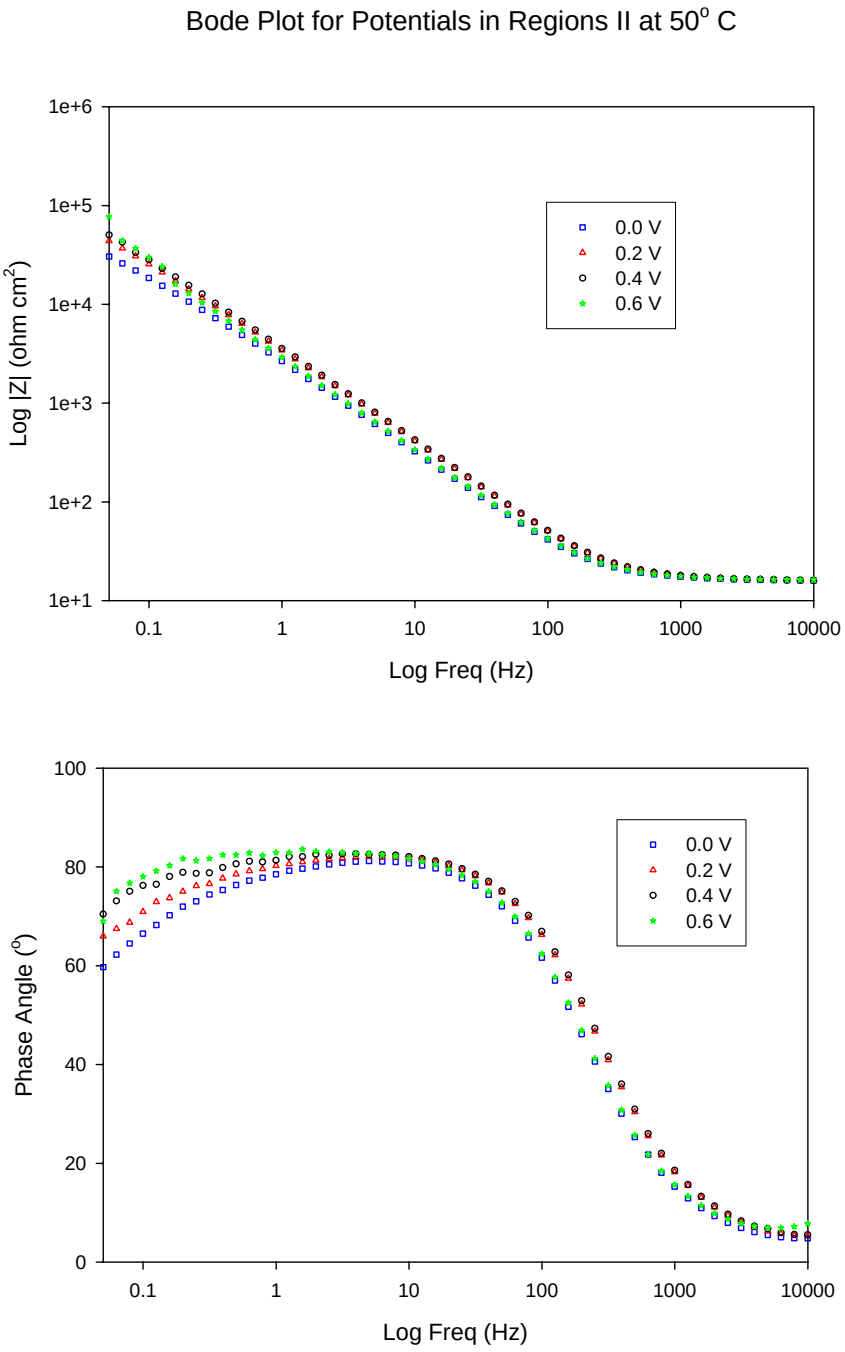

Figure **4-12**: Bode plot showing the impedance values over the potential range of Region II for impedance measurements at 50° C. The scans were performed from 10000 Hz to 0.05 Hz because the data at the low/high frequencies were "noisy".

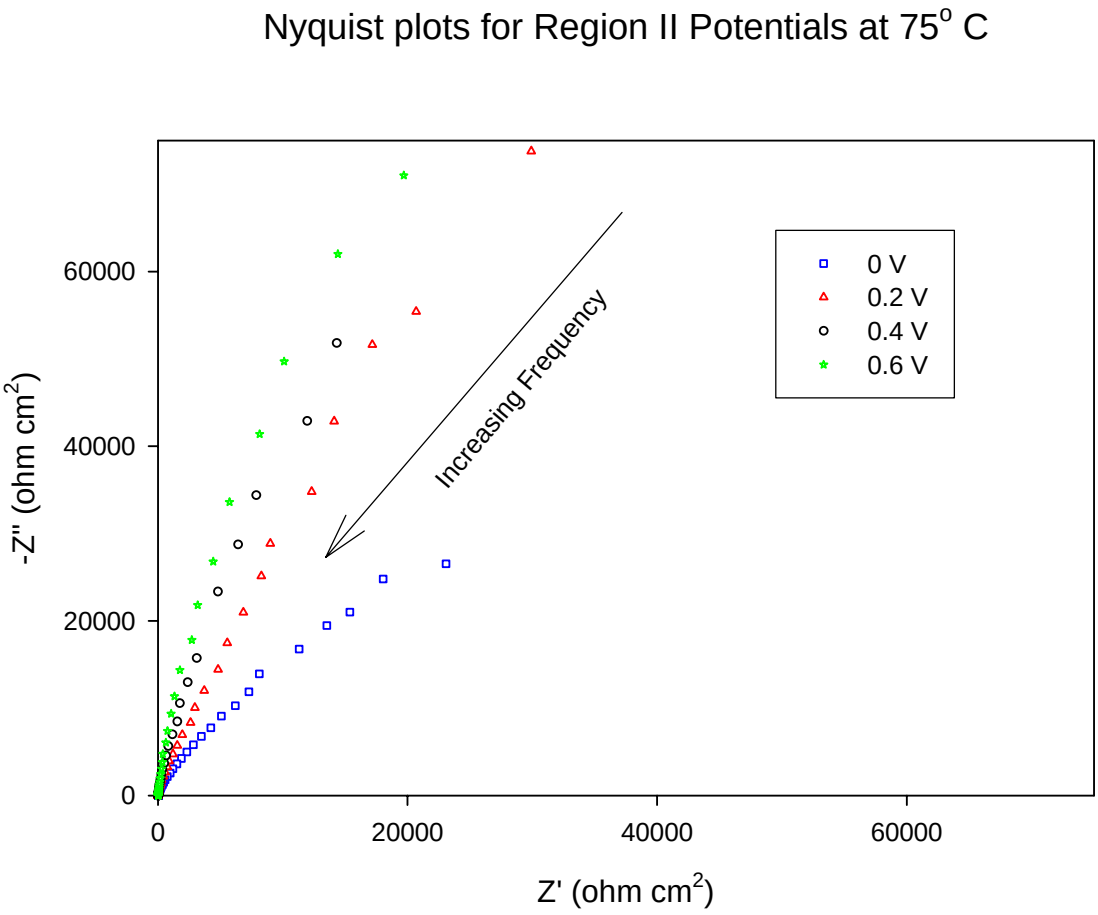

Figure **4-13**: Nyquist plot showing the impedance values over the potential range of Region II for impedance measurements at 75° C. The scans were performed from 10000 Hz to 0.05 Hz because the data at the low/high frequencies were "noisy".

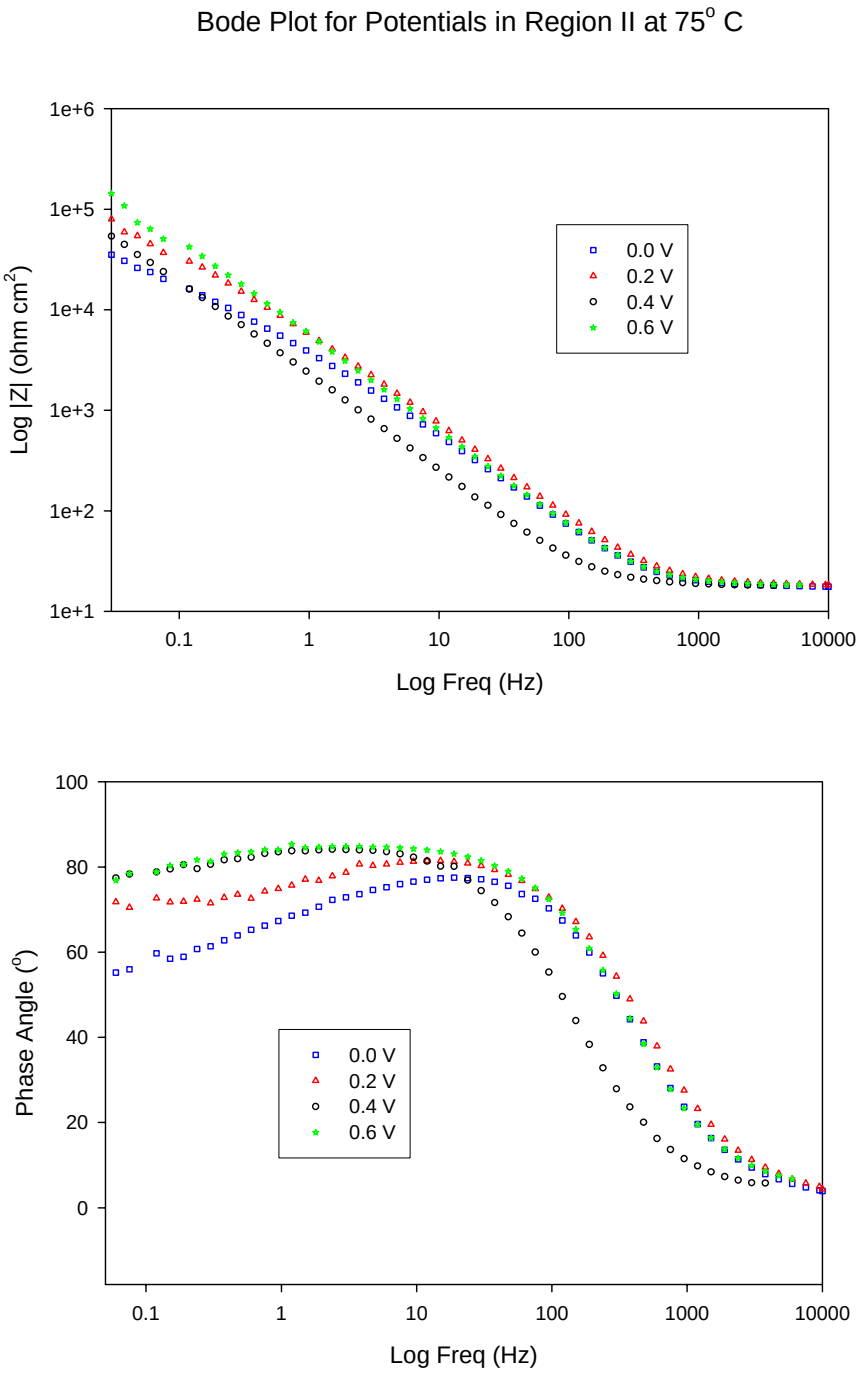

Figure **4-14**: Nyquist plot showing the impedance values over the potential range of Region II for impedance measurements at 75° C. The scans were performed from 10000 Hz to 0.05 Hz because the data at the low/high frequencies were "noisy".

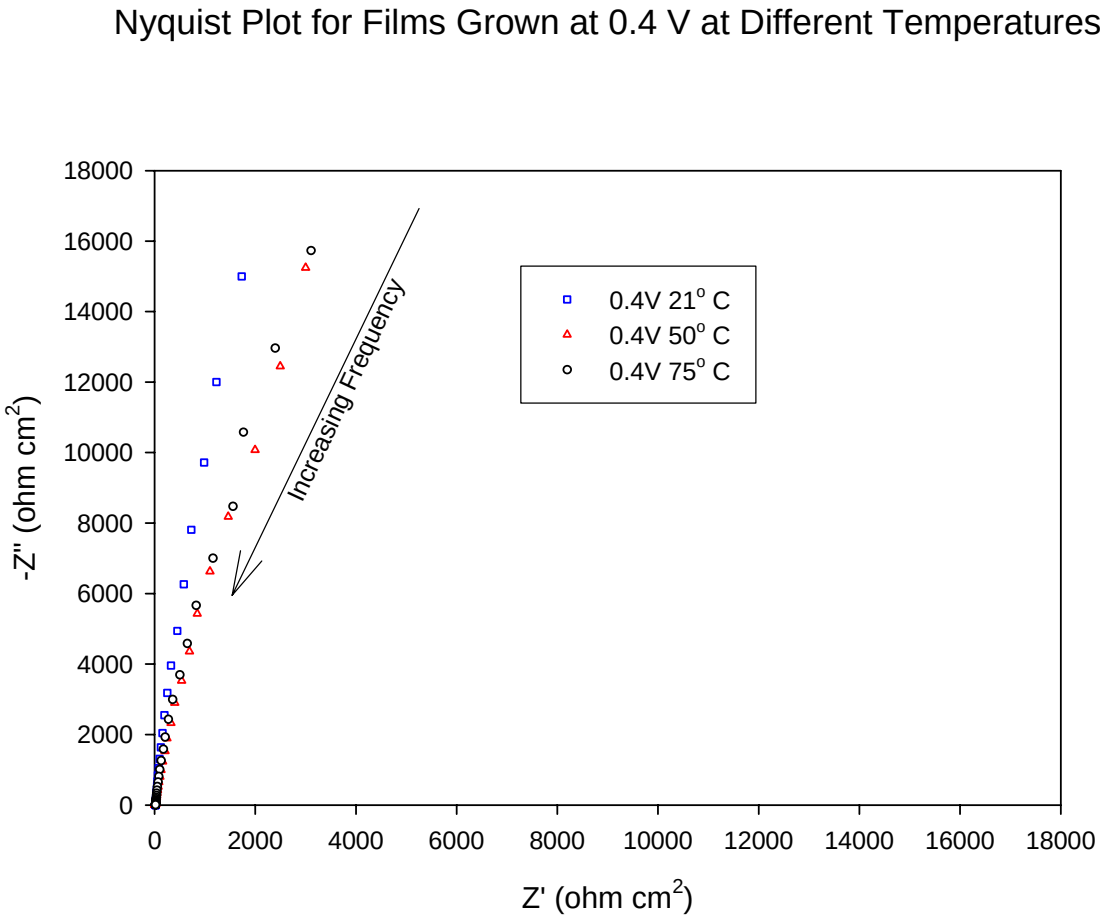

Figure **4-15**: Nyquist plots for films grown at 0.4 V at the various temperatures.

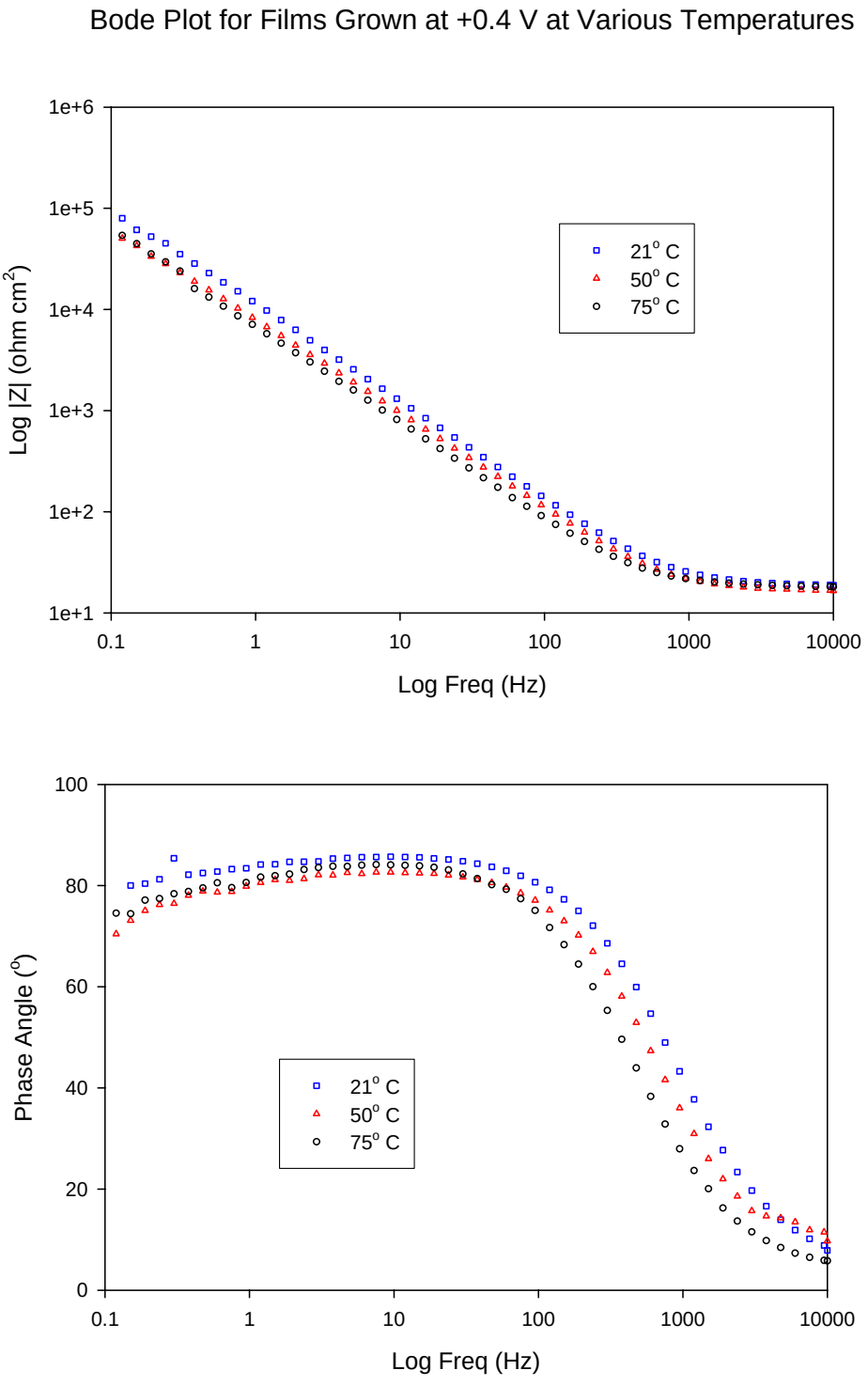

Figure **4-16**: Bode plots for films grown at 0.4 V at the various temperatures.

4.6 Ellipsometry Results

Ellipsometry is an optical analysis technique capable of measuring film thicknesses based on the optical constants (refractive index (n) and extinction coefficient (k)) of the substrate and the film. It is a non-destructive technique and can measure changes in film thickness in the angstrom range if the optical constants are known with a great deal of accuracy.

Ellipsometry splits elliptically polarized light into two components, one parallel to the surface and one perpendicular to the surface. The superscript "s" is used to identify the plane parallel to the plane of incidence while "p" denotes the plane perpendicular to the incident plane. Ellipsometry works by measuring two parameters, Ψ and Δ . The parameters are usually measured as tan Ψ and cos Δ.. Tan Ψ is the angle whose tangent is the ratio of the magnitudes of the total reflection coefficients and is shown in Eq. **4.2.**

$$\tan \psi = \frac{\left| R^{P} \right|}{\left| R^{S} \right|} \qquad \textbf{4.2}$$

R^P represents the ratio of the change in wave amplitude of the incident wave to the reflected wave in the P plane. R^S is the same, except for the S plane. The absolute value is the magnitude of the amplitude changes. Cos Δ is the phase shift in the wave after reflection and is shown in Eq. **4.3.** In this equation, δ_1 is the phase difference between the s wave and p wave prior to reflection and δ_2 is the phase difference of the two waves after reflection.

$$Cos\Delta = \partial_1 - \partial_2 \qquad \textbf{4.3}$$

These two parameters are functions of n, k, and d (film thickness). Therefore, if the optical constants are known, the film thickness can be determined to high accuracy. However, the optical constants for passive films are not always the same as those of the bulk. Therefore, we are left with two equations and three unknowns. By using the Levengrand-Marquet algorithm and assuming starting values for the optical constants (based on the known n and k for the bulk materials) and an estimated film thickness, regression analysis can yield the best fit to the data. From this fit, the film thickness and optical constants can be obtained.

Many researchers have applied ellipsometry to analyze the film formed on iron [12, 25-28] and the results vary a little. However, it should be noted that most of these measurements were based on a single wavelength and this measurement technique has a high degree of error associated with it. Because optical constants are actually a function of wavelength (and not really constants), a measurement over a wavelength range helps decrease the errors in measurement. The ellipsometer used in this work is a scanning wavelength ellipsometer. The wavelength range of the equipment is 250 nm to 850 nm.

The measurement method used in this paper began by measuring the effective optical constants for the iron-borate buffer system. The effective optical constant method can be used because it is assumed that the optical constants of the pure iron surface in contact with the borate buffer solution remain the same at a single temperature. Therefore, a base measurement was taken directly after electrochemically removing the air-formed oxide layer (i.e. a 30 sec pretreatment at -0.1 V) . Because no film is present at this point, there is no thickness parameter needed in the calculations. Therefore, the optical constants can be directly calculated from the equation discussed above. It should

be noted that the surface roughness is now accounted for in this measurement which alleviates the need to add a roughness layer into the model.

Next, capacity measurements were used to estimate the film thickness based on a parallel plate capacitor (with the film representing the dielectric). The thickness was measured using the basic parallel plate equation shown in Eq. **4.4**. In this equation, the dielectric constant ($\hat{\varepsilon}$) used for iron is 30 and ε is the vacuum permittivity with a value of 8.85×10^{-14} F/cm. The surface area is represented by A (cm^2) and L is the thickness. This method is somewhat controversial as a method for measuring film thickness, but nevertheless it provides a good estimate to use in the ellipsometric regression analysis. In addition the values obtained using this method are in close agreement to other methods used to calculate film thickness (such as galvanometric studies, XPS analysis, reflectivity measurements, etc.).

$$C = \frac{\hat{\varepsilon}\varepsilon_o A}{L} \qquad \textbf{4.4}$$

Ellipsometric measurements were made on potentiostatically formed films over the passive range at 21°C, 50°C, and 75°C. The room temperature data (21° C) is shown in Figure **4-17** and Figure **4-18**. While looking at the Tan Ψ, the change with potential is observed to be rather small, except for the longer wavelengths. This is because small changes in film thickness affect the reflected intensity very little. However, the Cos Δ plots reveal a much greater change with film thickness because the phase shift is much more sensitive to small thickness changes.

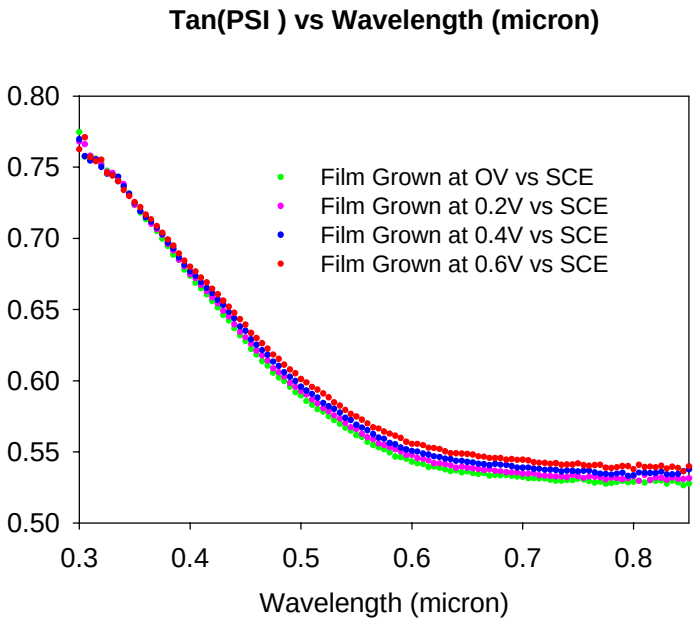

Figure **4-17**: Tan Ψ vs. wavelength for oxide films grown at room temperature in borate buffer solutions containing EDTA. The observable differences are much larger for the longer wavelengths and show an increasing trend with formation potential.

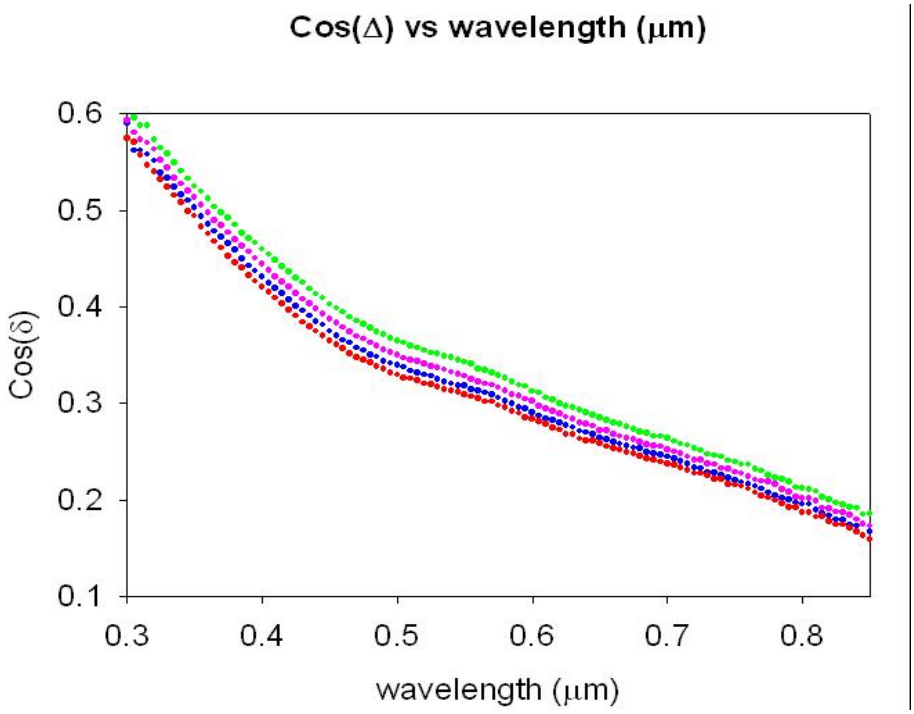

Figure **4-18**: Cos Δ versus wavelength for the room temperature ellipsometer measurements. The change with formation potential is much more evident with this parameter because small changes in thickness can shift the phase.

Before showing the results, it should be explained that a film thickness was measured for each formation potential using the parallel plate capacitor method. This thickness was input into the ellipsometer model for each of the formation potentials and regression analysis was performed on each set of data. The result yielded the optical constants for each set of ellipsometry data. The optical constants (n and k) were in very close agreement for each formation potential as would be expected if the thicknesses were close to the true values. Therefore, an average of all of the n and k's obtained were used to represent the optical constants for the film formed on iron. These constants were used for the passive film in each of the temperature studies. However, a base

measurment was made on the film-free iron in solution for each temperature. This was done to account for any changes in the effective optical constants induced by the temperature change in the solution.

Before showing the thickness results for the above ellipsometer measurements, the effects of EDTA on the film will be briefly discussed. The same experiments were carried out in a borate buffer solution without EDTA. However, a single layer model did not allow for a good fit on the data as seen in Figure **4-19**

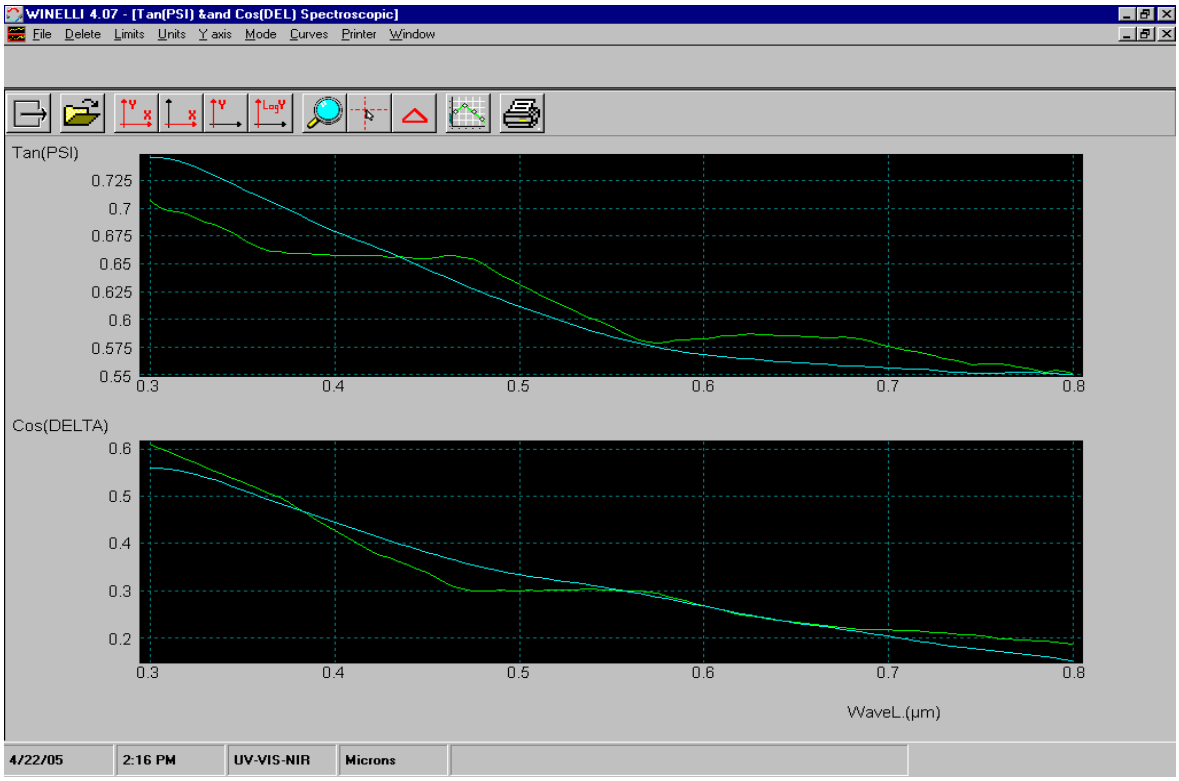

Figure **4-19**: Regression fit (blue line) to ellipsometry data for a film grown at +0.4V vs SCE in borate buffer solution containing no EDTA. The model used was for a single oxide film and yields a very poor fit. It is easily seen in this plot that the data (green line containing the step patterns) is obviously different than for the data generated in solutions containing EDTA.

Therefore, a two-layer model was generated to help account for the obvious difference in shape of the ellipsometry data. The model consisted of the orginal effective optical constants as a substrate, a layer with the optical constants obtained from the solution without EDTA, followed by another layer with unknown optical constants and layer thickness. Because many researchers state the outer layer formed on iron has a similar structure to Fe_2O_3, the bulk optical constants (from Fe_2O_3) were used as estimates to begin the regression process. Estimates for the inner and outer film thicknesses were entered in the model and were chosen as fitting parameters in the regression model. The end result yielded a very good fit to the data as can be seen in Figure **4-20**. This provides further circumstantial evidence that EDTA does prevent the formation of an outer layer as has been suggested by others [8].

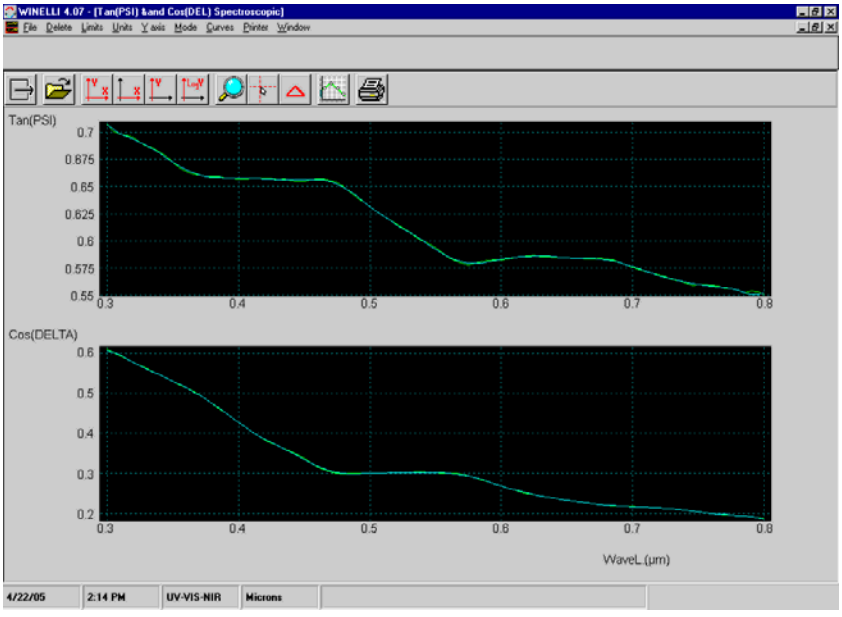

Figure **4-20**: Regression fit (blue line) to ellipsometry data for a film grown at +0.4V vs SCE in borate buffer solution containing No EDTA. Model used was for double-layer oxide film and it gives a good fit.

The thickness values generated from the regression analysis are shown in Table **4-1**. The data indicates that EDTA added to the solution prevents the formation of an outer precipitate layer. In addition the EDTA appears to lead to a thinning of the inner layer that is viewed to be the barrier layer in both the single and two-layer regression models. Another interesting outcome is that the inner layer reaches a thickness of about 3 nm at the lowest formation potential in solutions without EDTA. The inner layer thickness remains the same for each potential and it is only the outer layer that grows. This could be attributed to the fact that the outer layer slows the dissolution process allowing the inner layer to achieve a maximum thickness in the early stages of passivation. The error in the regression values, based on the fits, had a maximum value of 6% (or roughly 0.2 nm for the worst fit).

Table **4-1**: Individual layer and total thickness values for the oxide(s) formed on iron in borate buffer solution with and without EDTA. Values were obtained by performing a regression analysis on the tan(Ψ) and Cos(Δ) to obtain a thickness or thicknesses for the oxide film(s) formed on iron. A **single layer model** was used to fit the data for oxides grown in the **EDTA containing** solution, while a **double layer model** was used for the fit for oxides formed in solutions **not containing EDTA**.

Potential for Film Growth (V vs SCE)	Oxide Thickness (nm)			
	Without EDTA		With EDTA	
	Individual Layer (Outer/Inner)	Total	Individual Layer (Outer/Inner)	Total
0.2V	2.99 1.47	4.46	N/A 0.98	0.98
0.4V	3.00 2.01	5.01	N/A 1.08	1.08
0.6V	3.04 2.31	5.35	N/A 1.21	1.21
0.8V	3.03 3.10	6.13	N/A 1.52	1.52

As for the dependence of thickness on temperature, Table **4-2** lists the values as determined by the regression. Figure **4-21** plots the data to illustrate the linear dependence of thickness on potential. However, the 75° C data shows the thickness increases in a linear manner to 0.4 V, where it appears to reach a maximum thickness. This linear dependence is a prediction of the PDM and will be discussed in greater detail in the next chapter. Table **4-3** shows the difference between the parallel plate thickness measurements and the ellipsometry measurements. There is good agreement between the two measurements and the slight difference can correspond to a small change in the dielectric constant, due to defect concentration changes, during the impedance measurement.

Table **4-2**: Thickness values as a function of temperature and formation potential.

Formation Potential	21° C	50° C	75°
0.0V	0.98 nm	1.92 nm	1.82 nm
+0.2V	1.08 nm	2.58 nm	4.08 nm
+0.4V	1.21 nm	3.24 nm	5.24 nm
+0.6V	1.52 nm	4.02 nm	5.36 nm

Table **4-3**: Table showing the thickness values as measured by the parallel plate method and by ellipsometry.

Formation Potential	**Parallel Plate (nm)**	**Ellipsometry (nm)**
0.0 V	0.80	0.98
0.2 V	0.97	1.08
0.4 V	1.16	1.21
0.6 V	1.43	1.52

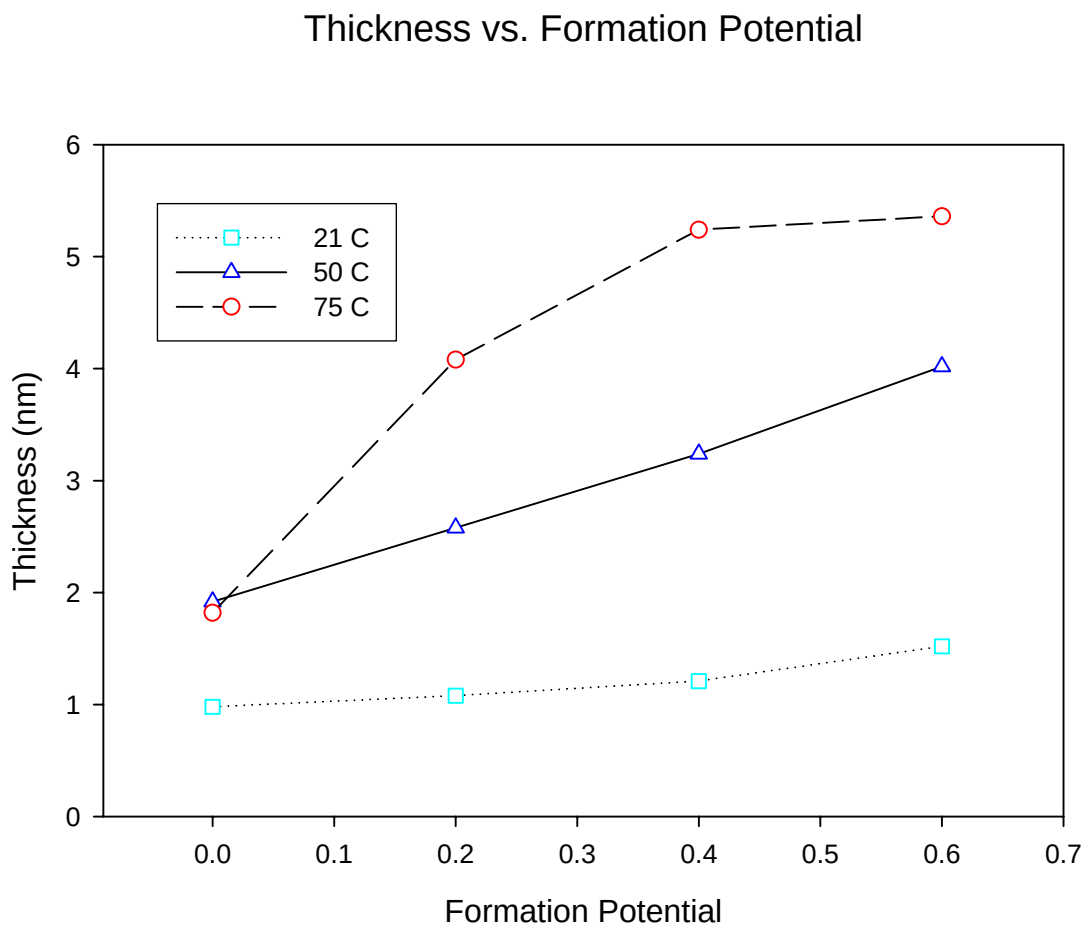

Figure **4-21**: Thickness vs. Potential for the various temperatures. The room temp. and 50° C plots display a linear behavior, whereas the 75° C plot appears to increase in thickness rapidly at the lower potentials.

4.7 Mott-Schottky Analysis

By viewing the film as an abrupt junction, Mott-Schottky analysis can be applied. Mott-Schottky analysis is being performed to identify the electronic nature of the film (n-

type or p-type)[10, 29, 30]. In addition the Mott-Schottky analysis will be used to account for changes in defect densities with formation voltage and temperature. There is some controversy surrounding the application of this type of analysis to aqueous systems, but other analysis techniques, such as photocurrent techniques [7, 31] find a good agreement with the values calculated using Mott-Schottky. Although the technique is designed to be of a quantitative measure, it is being applied more in a qualitative manner in this work.

It is generally agreed that the oxide formed on iron exhibits semi-conductive behavior [32]. Semiconductors can be classified as n-type or p-type. An n-type semiconductor conducts negative (-) charge and a p-type conducts positive (+) charge. By performing a Mott-Schottky analysis, it can be determined which type of semiconductor the iron oxide is. Mott-Schottky analysis measures of the inverse of the space charge capacitance ($1/C_{sc}$) in a semiconductor as a function of an applied potential (or voltage) across it. The C_{sc} exists due to the separation of charge within a semiconductor when a potential is applied. The magnitude of C_{sc} is related to the defect densities within the film. A defect is classified as a donor if it donates electrons to the conduction band and an acceptor if it accepts an electron from the valence band and leaves behind a positively charged hole. Eq. **4.5** and Eq. **4.6** show the relationship between C_{sc} and the defect densities for an n-type and p-type semiconductor, respectively.

$$\frac{1}{C_{sc}^2} = \frac{2}{\varepsilon\varepsilon_0 N_D A^2}\left(V - V_{fb} - 25mV\right) \qquad \textbf{4.5}$$

$$\frac{1}{C_{sc}^2} = \frac{-2}{\varepsilon\varepsilon_0 N_A A^2}\left(V - V_{fb} - 25mV\right) \qquad \textbf{4.6}$$

V_{fb} is the flat band potential and it corresponds to the potential when no band bending is present across the junction. N_D is the donor density concentration, N_A is the acceptor density concentration, ε is the dielectric constant of the oxide, A is the surface area of the interface and ε^o is the vacuum permittivity. Without going into details here, it can easily be seen that a plot of $1/C_{sc}^2$ vs. potential (E) will yield a line of either positive or negative slope. If the slope is positive, it means that the material is an n-type semiconductor and equation 3 would be used to calculate the donor density and flat band potential. If the slope is negative the material is p-type.

Figure **4-22** displays the Mott-Schottky plots for iron at each formation potential over the passive range. A 50 mV/sec scan rate was used to try and quickly measure the capacity before the film had time to adjust to the potential change. This is not a typical methodology for performing Mott-Schottky analysis due to the potential sweep instead of a step. However, the sweep method is used in this work for the reason mentioned above. A plot as a function of the formation potential as a step will be presented at the end of this section. Despite the observed non-linearity, it can be seen that the slope is positive over the majority of the passive Region indicating that the electronic character is n-type. The defects associated with this behavior are either/both oxygen vacancies and/or iron interstitials. Some researchers have suggested reasons for the non-linearity of the plots. Ahn [7] and Bojinov [33] attribute the non-linearity of the plot to mechanisms such as a variation in defect density through the film, presence of deep dopant states, and

relaxation phenomena. Stimming and Schultze state that the reason for the non-linearity is due to charging at the metal/film interface [34]. However, Stimmings Mott-Schottky experiments were performed by a potentiostatic pulse method. The change in slope was evident for each formation potential in his work, whereas, it is only seen at the high formation potential in this work. Therefore, another possible reason is being proposed to account for the non-linearity of the plots shown in Figure **4-22**.

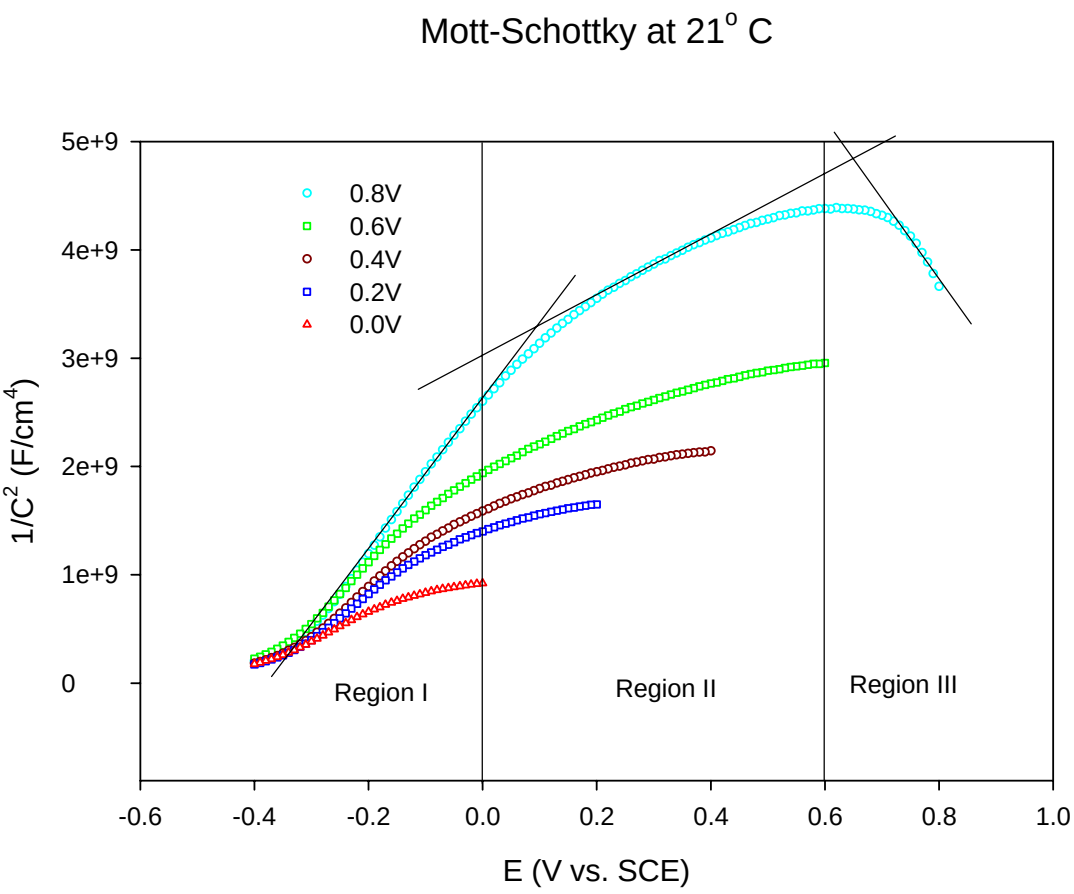

Figure **4-22**: Mott-Schottky plots for various formation potentials. The scan rate was 50mV/sec.

As has been mentioned prior, it is the author's opinion that there is a phase change occurring between the -0.2V to 0.0V range. The phase change is related to the oxidation/reduction of the iron cations from one oxidation state to another in this range (dependent on the potential sweep direction). For example, as the potential sweeps down through this range, Fe^{3+} can be reduced to Fe^{2+} leading to a sudden change in the defect density. Electrons in the conduction band are removed to reduce the iron species. However, the next question concerns the apparent change in the electronic character between 0.6V to 0.8V (Region III in potentiodynamic scan).

The proposed reason for this change in electronic character is that the passive film formed on iron contains nearly the same densities of iron interstitials, oxygen vacancies, and iron vacancies (as calculated by the Mott-Schottky slopes in the three Regions). This claim could possibly lead to the behavior observed near the upper end of the passive Region in iron. The reasoning is as follows, as the potential is increased, the oxygen activity at the surface is increased. The increase in oxygen activity leads to a decrease in the concentration of oxygen vacancies in the film (can be understood by considering the rate constant for rxn V in Figure **3-2**). Because the defect densities are near the same magnitude for each defect type, the drop in oxygen vacancies shifts the majority defect concentration from the n-type defects (oxygen vacancies and/or iron interstitials) to the p-type defect (cation vacancies). This phenomena has been shown to occur in Fe_2O_3 and Fe_3O_4 in high temperature experiments where researchers were measuring the Seebeck voltages. Warnes noted that for temperatures lower than 800° C, both oxides exhibited n-type behavior in oxygen containing atmospheres [35]. However, above 800° C the oxides changed to a p-type behavior. Although Warnes et al. view the oxides to contain

only oxygen vacancies and iron interstitials, the work attributes the change in electronic character to an increase in the mobility of holes at higher temperatures.

While there is not a method described here for identifying the defects present in the film, there is work suggesting that oxygen vacancies can be important minority defects in iron oxide films [36-39] (note: the term minority is loosely used here and is not to be confused with the electronic minority/majority defects). In addition, the thermodynamic data for defect formation in low-temperature iron oxides is scattered and the values for the formation of each of the mentioned defects has been presented as being very close [40]. Most papers listing thermodynamic data for defect formation energies in the various iron oxides also indicate that energy for migration of the defects is lower than the formation energies. Therefore, if defects can form, it is fairly certain that they will be able to migrate through the film. This point helps support the fact that the PDM, applied in this work, at this time ignores the diffusion/migration through the film. However, a simple Warburg impedance can be incorporated to account for the diffusion of defects through the film.

Figure **4-23**, Figure **4-24,** and Figure **4-25** display the defect densities of the types of defects believed to be responsible for the non-linear behavior of the Mott-Schottky plots. The changes in the slopes correspond with the transitions from Region I to Region II and from Region II to Region III as discussed in the potentiodynamic section. The plots show one point corresponding to the p-type defect density as calculated by the negative slope in the upper Region of the passive Region. The values of the n-type defect densities are seen to be decreasing with the increasing potential until they nearly converge on a number very close to the value of that calculated for the defect density in

Region III. This density would be for an acceptor due to the p-type behavior. Therefore, it is suggested that the dominant defect in Region III becomes iron vacancies, which can give rise to the p-type behavior. This finding is also in agreement with the LAMM phase as proposed by Davenport and Toney [1, 41, 42]. The film formation method used by Davenport and Toney first used a cathodic pretreatment to reduce any air-formed oxide and then a direct jump in potential to the highest potential in the passive Region (+0.8 V_{SCE}, almost in the oxygen evolution Region). This might suggest that the oxide goes through yet another phase change that leads to p-type behavior (cation vacancies are major defect in the proposed LAMM phase). However, in order to more fully understand the passivation of iron, the structure should be analyzed as a function of the formation potential across the entire passive range. An overall description would be that $Fe_3O_4 \rightarrow$ γ-Fe_2O_3 in the Region I/Region II transition and then from γ-$Fe_2O_3 \rightarrow$ LAMM phase for the Region II/Region III transition. Yet another explanation can be suggested by considering that the film is closer to a highly defective magnetite, which contains small concentrations of Fe^{2+} (thermodynamics would dictate that some Fe^{2+} should be present in the film). If, at higher potentials, Fe^{2+} oxidizes further, then rxn IV in Figure **3-2** of the PDM would begin to "switch on". This reaction corresponds to the generation of cation vacancies in the film, thereby giving rise to a sudden increase in the acceptor concentration which finally results in p-type behavior.

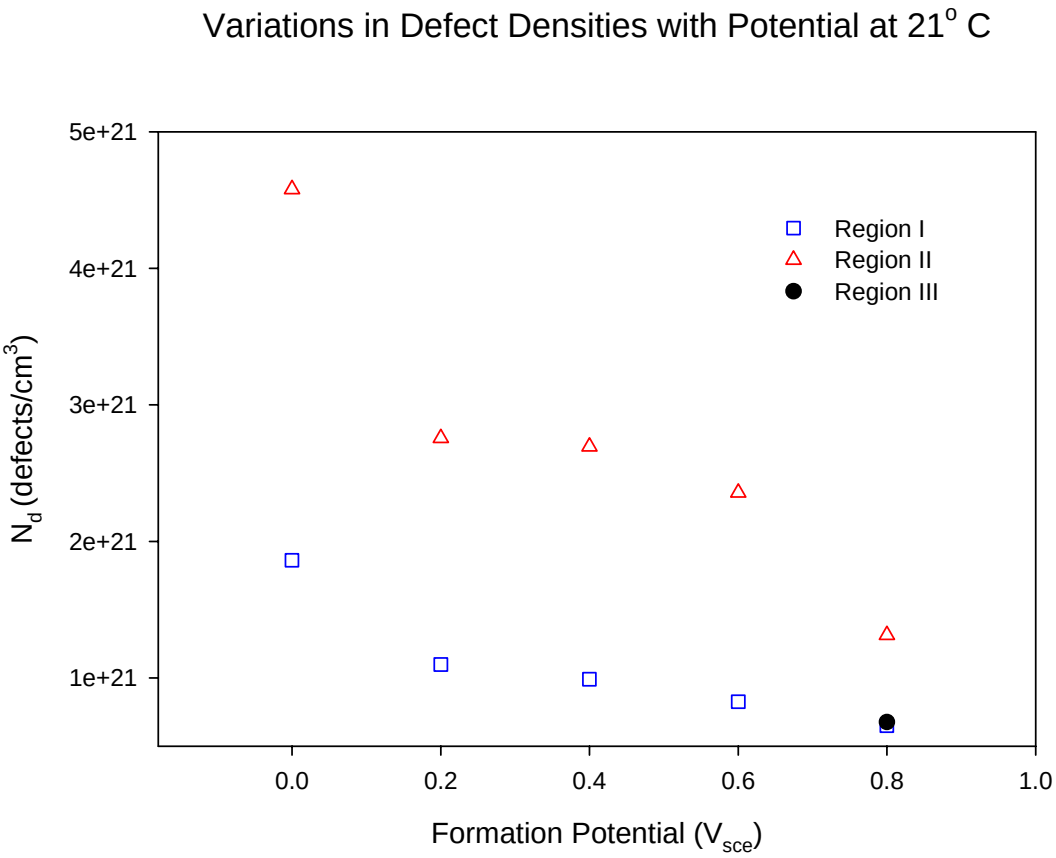

Figure **4-23**: The variation of the defect density with potential as calculated by the Mott-Schottky slopes at room temp.

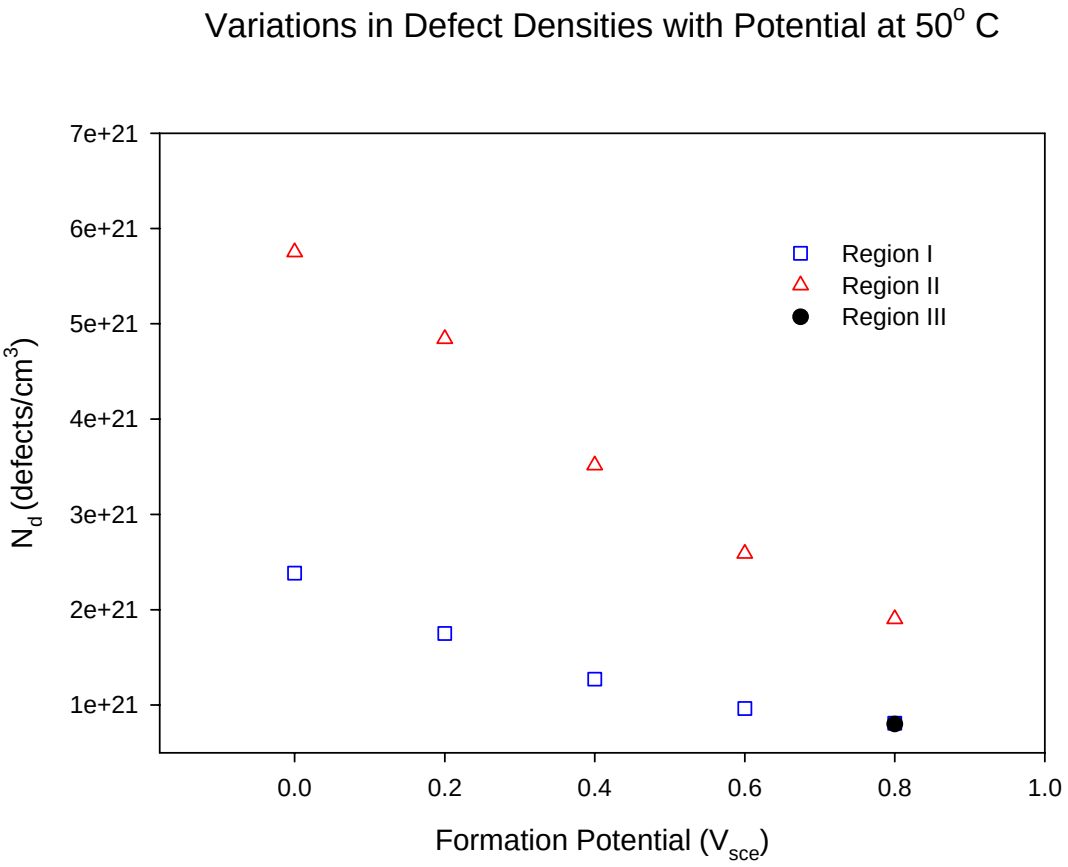

Figure **4-24**: Variation in defect density with potential as calculated by the Mott-Schottky slopes at 50°C.

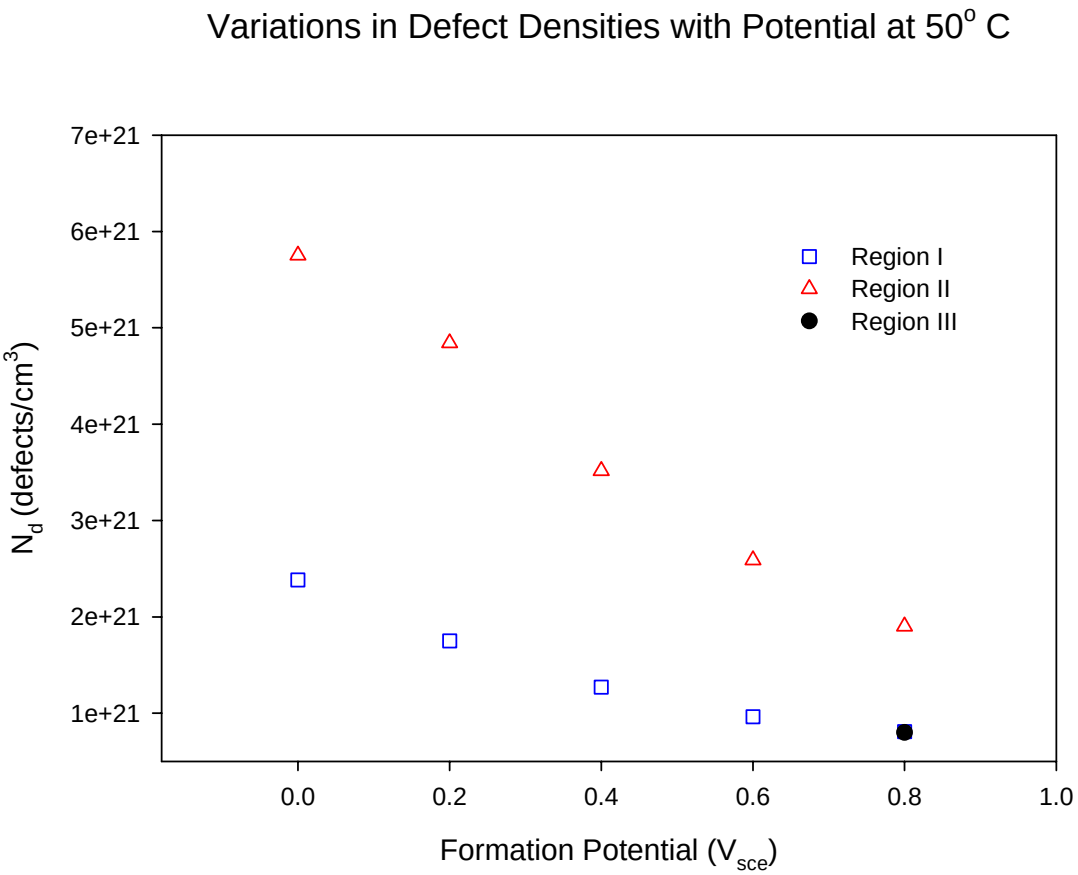

Figure **4-25**: Variation in defect density with potential as calculated by the Mott-Schottky slopes at 75°C.

A final plot of the n-type defect densities as a function of temperature is presented in Figure **4-26**. The defect densities are for a formation potential of +0.4V at each temperature. The defect density increases from the room temperature measurement to the 50° C measurement as would be expected. However, the density drops off at the 70° C temperature.

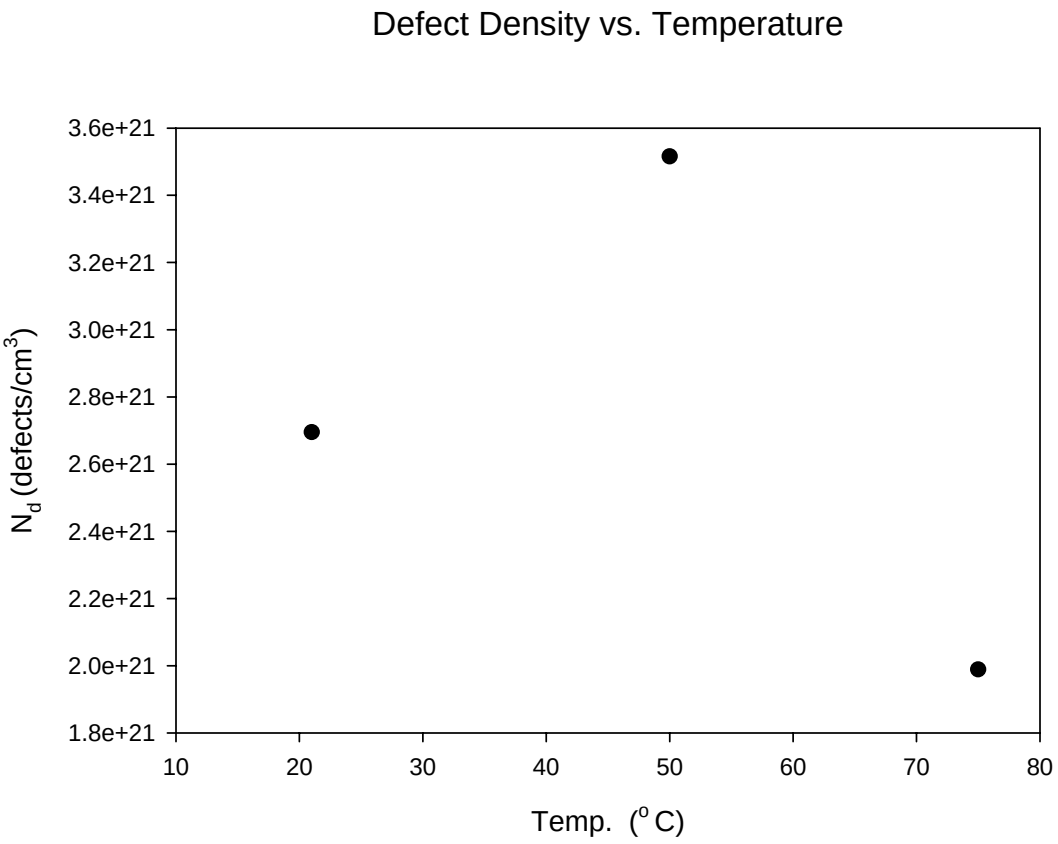

Figure **4-26**: The defect densities corresponding to Region II for an oxide formed at + 0.4 V_{sce}. The density increases from 21° C to 50° C, but decreases again at 75° C.

As stated earlier, a true Mott-Schottky analysis would use a potential step method and plot each point at a single potential (or voltage). Therefore, each $1/C^2$ value was extracted from the data at each formation potential (i.e. a single point on the Mott-Schottky plot) and the plot is shown in Figure **4-27**. The value for the donor density for this plot is 1.8e21 defect/cm^2. It should be noted here that for a sweeping Mott-Schottky plot, it should be no surprise that the plot is not linear when considering the PDM. The reaction rates for the PDM are functions of the potential drops at the interfaces, which is in turn a function the applied potential. As the reaction rates increase or decrease, the

concentration of defects will change. Therefore, a sweeping plot should display non-linearity.

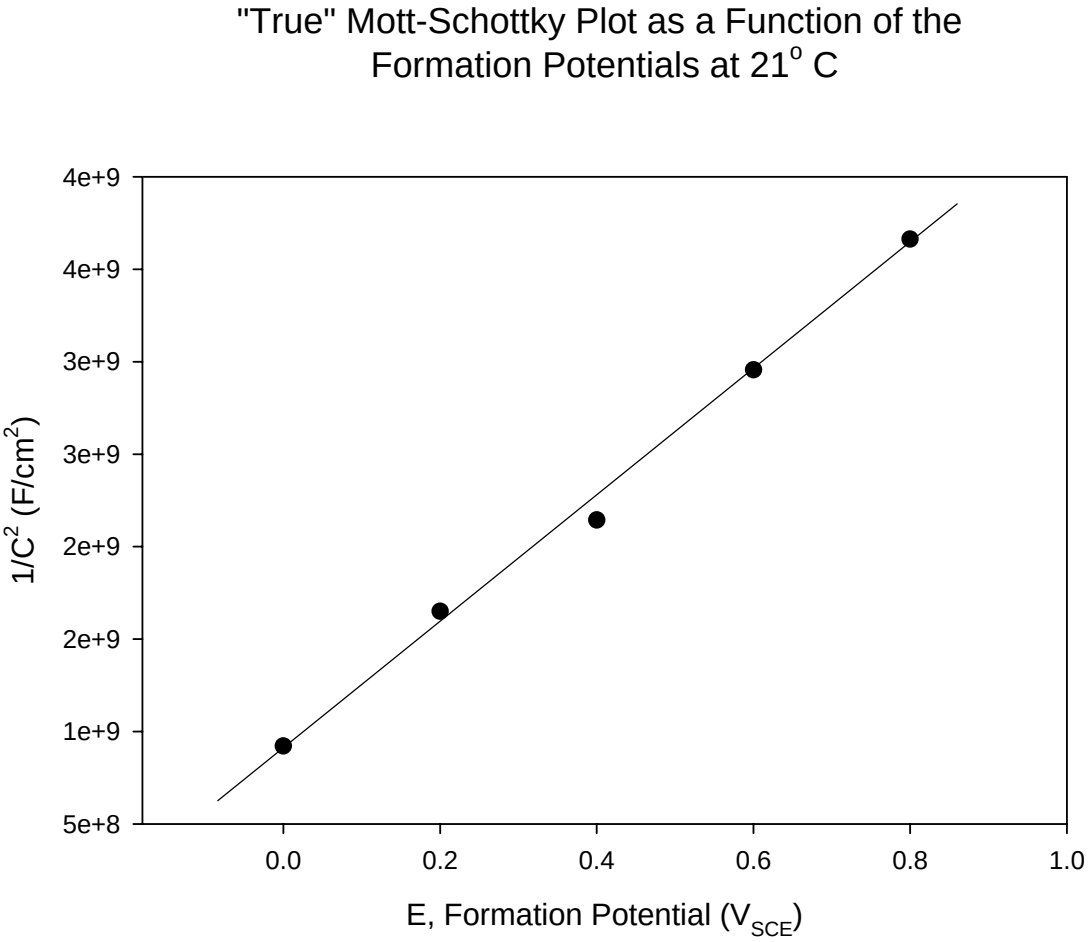

Figure **4-27**: Plotting the $1/C^2$ values for each formation potential and the result is a linear plot.

4.8 XPS Analysis of the Passive Iron Oxide Film

XPS was performed on the iron samples containing oxides grown at -0.2V and +0.5V. The lower formation potential (-0.2V) was chosen to determine if any substantial amount of Fe^{2+} was present in the film. This formation potential is on the edge of Region

I and was found by Nagayama and Cohen to be the potential below which, Fe^{2+} was observed to dissolve in solution [4]. The +0.5V formation potential was chosen because it is located just above the center of the passive Region. The goal of this analysis is to determine which species are present in the film to aid in the development of the PDM.

Low resolution survey scans were acquired on all samples followed by high resolution scans of selected elements. XPS quantification was performed by applying the appropriate relative sensitivity factors (RSFS) for the Kratos instrument to the integrated peak areas. These RSFs take into consideration the x-ray cross section and the transmission function of the spectrometer.

Species observed on both the -0.2V and +0.5V treated samples included Fe° and Fe^{3+}. The initial samples were contaminated with some organic species, most likely due to the ex-situ environment. Table **4-4** lists the concentrations of the species present in the film.

Table **4-4**: Concentration of Elements Detected and Oxide Thickness

Sample	Fe	O	C	$\%Fe^{o}$	$\%Fe^{3+}$	t_{ox} (Å)
-0.2V	19.1	40.7	40.2	70	30	27.0
+0.5V	38.1	48.3	13.5	85	15	39.6

The asymmetric tail on the Fe° peak and the Fe^{3+} 'pre-peak' overlap with the expected Fe^{2+} peak position (~708.5 eV). The resulting relative detection limit on these samples is estimated to be 10% (i.e., if ≤10% of the iron is present as Fe^{2+} it will be undetectable; if ≥10% Fe^{2+} were present it would be detectable). Curve fits acquired at 90° takeoff angles are shown in Figure **4-28** . Angle resolved XPS was not performed

because if any Fe^{2+} were present in the film, it would be located deeper in the oxide layer, near the metal/film interface and the 90° take-off angle would detect it.

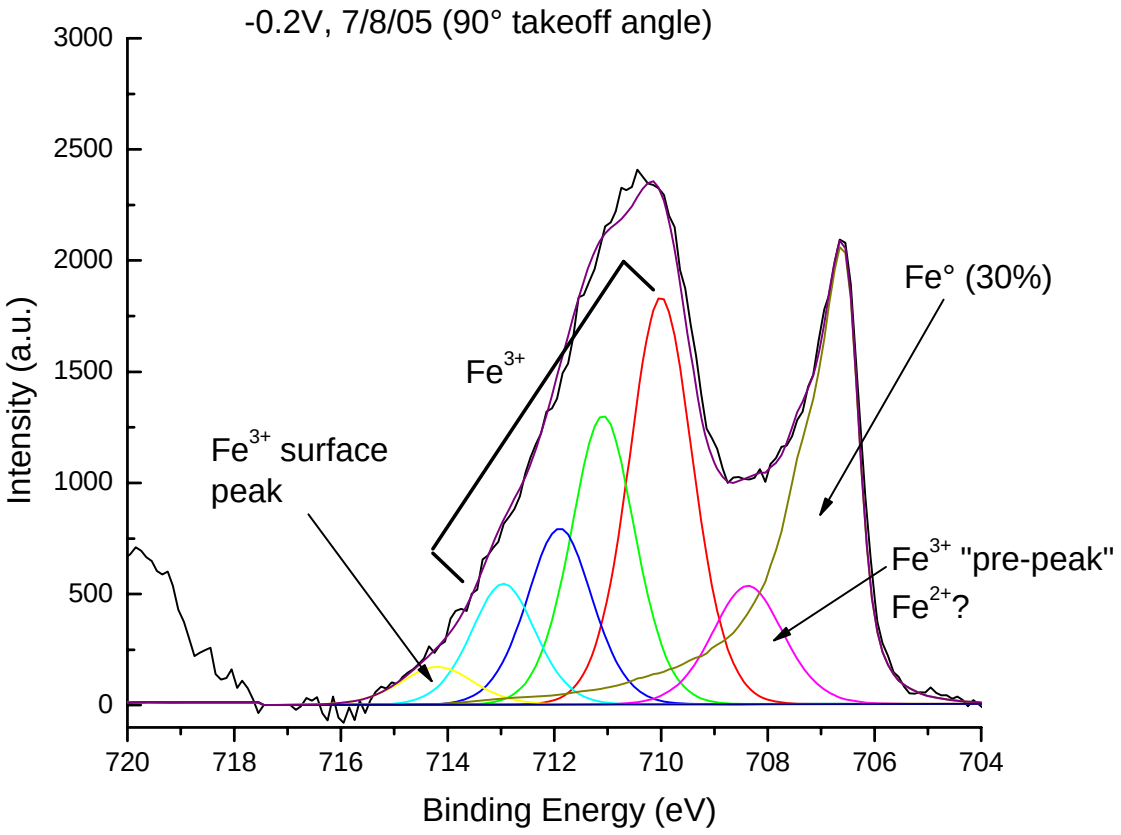

Fitting procedure adopted from Grosvenor et al. *Surf. Interface Anal*. ***36*** *(2004) 1564.*

Figure **4-28**: Curve-fitting to the XPS iron peak to determine the quantities and oxidation states present in an iron film formed at -0.2V.

The Fe oxide thickness was calculated assuming all Fe^{3+} was present as Fe_2O_3 using Eq. **4.7**,a commonly accepted approach in XPS studies. As expected the +0.5V sample contained a thicker oxide layer compared with the -0.2V sample (39.6 Å vs 27.0Å). The technique used for making these measurements follows the procedure set forth by Grosvenor [43].

$$t_{Fe2O3} = \lambda_{Fe2O3} \sin\theta \ln\left\{\left(\frac{\rho_{Fe^\circ}\lambda_{Fe^\circ}}{\rho_{Fe2O3}\lambda_{Fe2O3}}\right)\left(\frac{I^{exp}_{Fe2O3}}{I^{exp}_{Fe^\circ}}\right)+1\right\} \qquad \textbf{4.7}$$

where,

λ_{Fe2O3} = inelastic mean free path of Fe 2p electrons in Fe_2O_3[1] = 16.5 Å

λ_{Fe° = inelastic mean free path of Fe 2p electrons in Fe° = 13.6 Å

θ = takeoff angle, 90°

ρ_{Fe° = atom density of Fe° = 8.47 X 10^{22} atoms/cm^3

ρ_{Fe2O3} = atom density of iron in Fe_2O_3 = (2/5)*9.88 X 10^{22} atoms/cm^3

= 3.95 X 10^{22} Fe atoms/cm^3

I^{exp}_{Fe2O3} = experimentally determined fraction of Fe_2O_3 (from Fe $2p_{3/2}$ curve fit)

$I^{exp}_{Fe^\circ}$ = experimentally determined fraction of Fe° (from Fe $2p_{3/2}$ curve fitting)

Based on the above findings, the oxide cannot possibly be Fe_3O_4 because the number of cation vacancies (approximately 20% of iron sites) would need to be vacant to justify the findings. If this were the case, the film would be p-type which is contradictory to the Mott-Schottky findings discussed above. The same would be true for the structure put forth by Davenport and workers [1]. Calculating the defect densities according to the occupancies of the sites in the suggested LAMM phase, the film would be designated a p-type semiconductor. The defect densities would be 1.2×10^{22} iron vacancies/cm^3 and 3.27×10^{21} interstitials/cm^3. It should be noted that they preclude the presence of any oxygen vacancies in their structure and this could be the reason for the n-type behavior as discussed before. However, as stated earlier, according to the PDM the film can only

grow by rxn III, and this reaction generates oxygen vacancies. Therefore, oxygen vacancies must be present in the film. In fact, by growing the film, then stepping to a lower voltage while measuring the change in thickness, the rate of oxygen vacancy generation can be arrived at. By realizing that at a steady-state, all reaction rates are equal, the dissolution rate would be equal to that of oxygen vacancy generation. This experiment was performed in both a borate buffer with and without EDTA. The results are shown in Figure **4-29**. The dissolution rate, measured as a change in thickness per unit time is nearly identical for both solutions. The noise in the data for the solution not containing EDTA is attributed to the spinning of a step motor in the ellipsometer during the measurements. The thickness change was actually calculated by stepping the potential in the negative direction, from the formation potential, and measuring the change in capacitance with time. The parallel plate method was then used to calculate the thickness change with time.

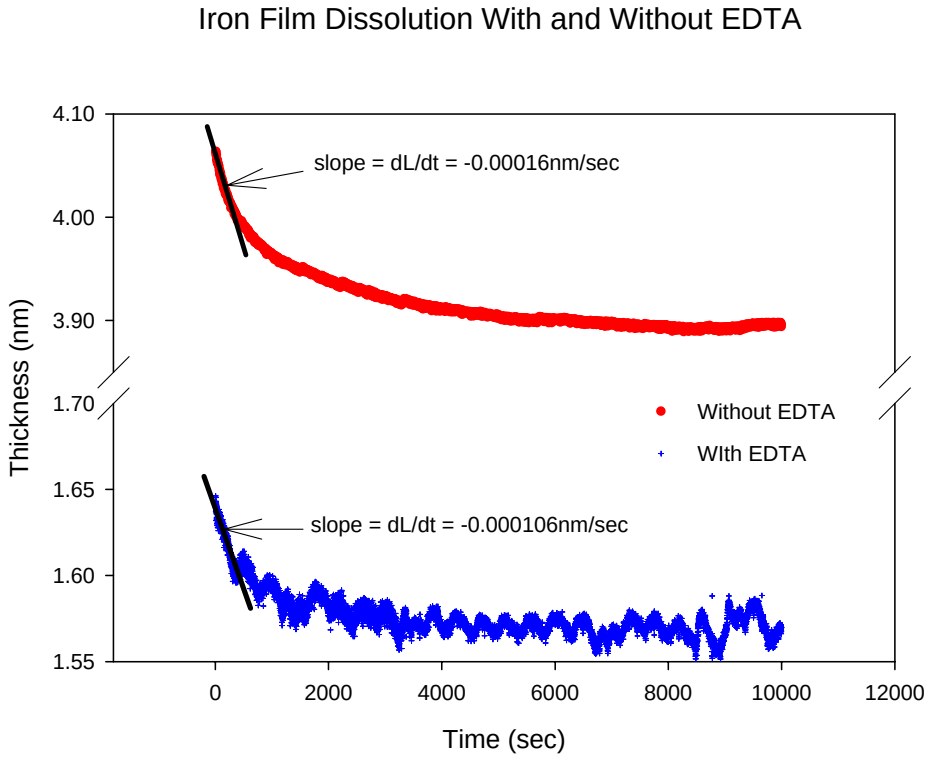

Figure **4-29**: The dissolution rate as measured by stepping the potential from the formation potential (+0.4 V) to -0.2 V and measuring the change in capacitance with time.

The film thickness change can be related to the rate of the reaction corresponding to film formation for the reasons given above. The equation for this is shown in Eq. **4.8**, where Ω is the molar density, χ is the charge associated with the iron cations (i.e. 2 for the initial oxidation of an iron atom) and k_3 is the reaction rate constant. The flux of oxygen vacancies, as calculated, would be approximately $7.41e10^{11}$ defects/cm^2sec. This flux would then dictate that oxygen vacancies should be present in the film.

$$\frac{dL}{dt} = \frac{2\Omega}{\chi} J_O = \Omega k_3 \qquad \textbf{4.8}$$

4.9 AFM analysis

As stated earlier, the original purpose for performing AFM analysis was to determine surface roughness for the ellipsometry regressions. However, the use of effective optical constants made it possible to ignore the surface roughness. Nevertheless, the AFM images obtained were of good quality and do provide useful information. Figure **4-30** displays the highest resolution image obtained from a +0.5V sample.

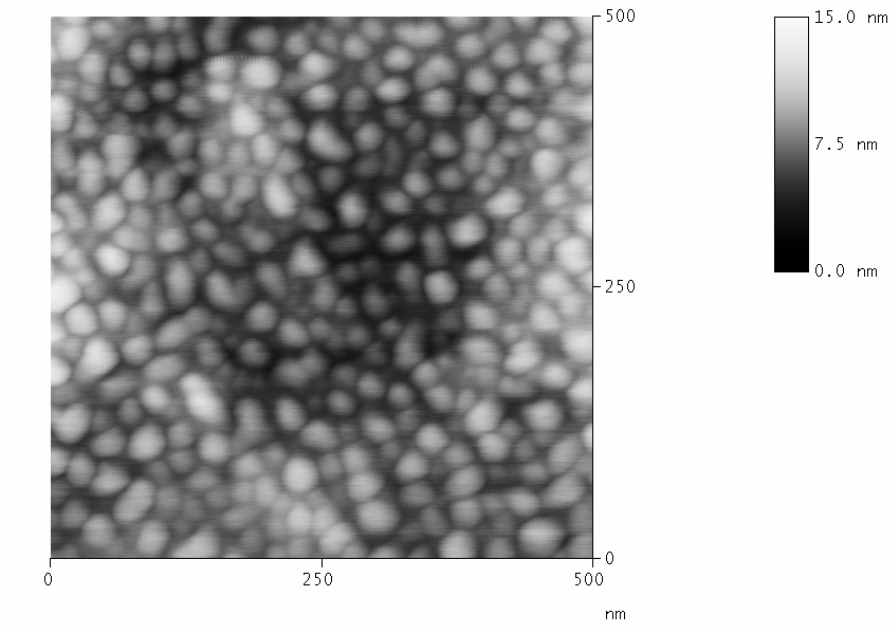

Figure **4-30**: The highest resolution image taken with the AFM of a film grown at +0.5V. The nano-sized grains are quite evident in the image and appear as islands.

The calculation of the grain size was obtained by first deconvoluting the image based on the tip shape. The tip shape is depicted in Figure **4-31.** The mean height of the grains was calculated to be approximately 5.27 nm.

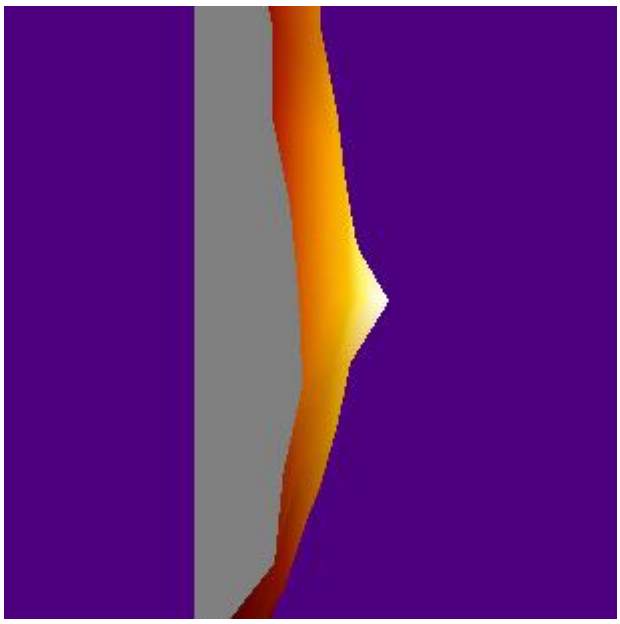

Figure **4-31**: A diagram showing the shape of the AFM tip.

The mean grain size was determined to be 6.86 nm by 16.9 nm. Therefore, indicating a nano-crystalline structure. This information is useful in arguing the validity of a PDM because a structure should be present to account for the existence of point defects (as is obvious). In addition, for future studies, grain boundary diffusion will need to be considered in any models accounting for just only diffusion. However, the point is moot here because only D_{eff} is the value of interest in the model. The effective diffusion coefficient is what would be needed to account for the total ionic current density.

4.10 References

1. Davenport, A.J., et al., *The Structure of the Passive Film That Forms on iron in Aqueous Environments.* Journal of The Electrochemical Society, 2000. **147**(6): p. 2162-2173.
2. Chao, C.Y., Lin, L.F., and Macdonald, D.D., *A Point Defect Model for Anodic Passive Films III. Impedance Response.* J. Electrochem. Soc., 1982. **129**(9): p. 1874-1879.
3. Ord, J.L. and De Smet, D.J., *The Anodic Oxidation of Iron: Overpotential Analysis for a Two-Phase Film.* J. Electrochem. Soc., 1976. **123**(12): p. 1876-1882.
4. Nagayama, M. and Cohen, M., J. Electrochem. Soc., 1962. **109**: p. 781.
5. Sato, N. and Cohen, M., J. Electrochem. Soc., 1964. **111**: p. 519.
6. Ord, J.L. and DeSmet, D.J., *Ellipsometric Measurements on Iron.* J. Electrochem. Soc., 1966. **113**(12): p. 1258-1262.
7. Ahn, S.J. and Kwon, H.S., *Effects of solution temperature on electronic properties of passive film formed on Fe in pH 8.5 borate buffer solution.* Electrochimica Acta, 2004. **49**(20): p. 3347-3353.
8. Sikora, E. and Macdonald, D.D., *The Passivity of Iron in the Presence of Ethylenediaminetetraacetic Acid.* J. Electrochem. Soc., 2000. **147**(11): p. 4087-4092.
9. Bucher, M., et al., *Comparison of the Semiconductive Properties of Sputter-Deposited Iron Oxides with the Passive Film on Iron.* Journal of The Electrochemical Society, 1998. **145**(2): p. 378-385.
10. Konig, U. and Schultze, J.W., *The examination of the influence of a space-charge layer on the formation kinetics of thin passive films by Schottky-Mott analysis.* Solid State Ionics, 1992. **53-56**(Part 1): p. 255-264.
11. Bardwell, J.A. and MacDougall, B., J. Electrochem. Soc., 1988. **135**: p. 2437.
12. Chen, C.-T. and Cahan, B.D., *The Nature of the Passive Film on Iron I. Automatic Ellipsommetric Spectroscopy Studies.* J. Electrochem. Soc., 1982. **129**(1): p. 17-26.
13. Cahan, B.D. and Chen, C.-T., *The Nature of the Passive Film on Iron III. The Chemi-Conductor Model and Further Supporting Evidence.* J. Electrochem. Soc., 1982. **129**(5): p. 921-925.
14. Moshtev, R.V., *Electronic conduction of the oxide film on passive iron in neutral solutions.* Electrochimica Acta, 1971. **16**(11): p. 2039-2048.

15. Keny, S.J., et al., *Radiation effects on the dissolution kinetics of magnetite and hematite in EDTA- and NTA-based dilute chemical decontamination formulations.* Radiation Physics and Chemistry, 2005. **72**(4): p. 475-482.
16. Cohen, M., *The Formation Properties of Passive Films on Iron.* Can. J. Chem., 1959. **37**: p. 286-291.
17. Goetz, R., et al., J. Electrochem. Soc., 1987. **134**: p. 535.
18. Battaglia, V. and Newman, J., *Modeling of a Growing Oxide Film: The Iron/Iron Oxide System.* J. Electrochem. Soc., 1995. **142**(5): p. 1423-1430.
19. Macdonald, D.D., Biaggio, S.R., and Song, H., *Steady-State Passive Films Interfacial Kinetic Effects and Diagnostic Criteria.* J. Electrochem. Soc., 1992. **139**(1): p. 170-177.
20. Liu, J. and Macdonald, D.D., J. Electrochem. Soc., 2001. **147**(11): p. B245.
21. Zhang, L., et al., *Onthe Kinetics of Growth of Anodic Oxide Films.* J. Electrochem. Soc., 1998. **145**(3): p. 898-905.
22. Liu, J., *Electrochemical emmision and impedance spectroscopies of passive iron and carbon steel*, in *Material Science and Engineering*. 2002, Pennsylvania State University: University Park, PA. p. 170.
23. Macdonald, D.D. and Urquidi-Macdonald, N., J. Electrochem. Soc., 1985. **132**: p. 2316.
24. Macdonald, D.D., *Passivity-the key to our metals-based civilization.* Pure and Applied Chemistry, 1999. **71**(6): p. 951-978.
25. An, I., et al., *Simultaneous real-time spectoroscopic ellipsometry and reflectance for monitoring thin-film preparation.* Rev. Sci. Instrum., 1994. **65**(11): p. 3489-3500.
26. Jovancicevic, V., et al., *The Passive Film on Iron: An Ellipsometric-Spectroscopic Study.* Lanmuir, 1987. **3**: p. 388.
27. Ohtsuka, T. and Ohta, A., *Growth of a passive film on iron in a neutral borate solution by three-parameter ellipsometry.* Materials Science and Engineering A, 1995. **198**(1-2): p. 169-175.
28. Sato, N. and Kudo, K., *Ellipsometry of the Passivation Film on iron in Neutral Solution.* Electrochimica Acta, 1971. **16**: p. 447-462.
29. Castro, E.B., Vilche, J.R., and Oliveira, C.L.F., *Comparative EIS study of passive layers formed on iron and iron-chromium alloys.* Materials Science Forum Proceedings of the 5th International Symposium on Electrochemical Methods in Corrosion Research - EMCR'94. Part 2 (of 2), Sep 5-8 1994, 1995. **192-194**(pt 2): p. 611-622.
30. Cabrera, N. and Mott, N.F., *Theory of the Oxidation of Metals.* Reports in Progress of Physics, 1949. **12**: p. 163.
31. Rahner, D., *Fe3O4 as part of the passive layer on iron.* Solid State Ionics, 1996. **86-88**(Part 2): p. 865-871.
32. Ahn, S. and Kwon, H., *Diffusivity of point defects in the passive film on Fe.* Journal of Electroanalytical Chemistry, 2005. **579**(2): p. 311-319.
33. Bojinov, M., et al., *Coupling between ionic defect structure and electronic conduction in passive films on iron, chromium and iron-chromium alloys.* Electrochimica Acta, 2000. **45**: p. 2029-2048.

34. Stimming, U. and Schultze, J.W., *The Capacity of Passivated Iron Electrodes and the Band Structure of the Passive Layer.* Berichte der Bunsen-Gesellscaft, 1976. **80**(12): p. 1297-1302.
35. Warnes, B.M., Aplan, F.F., and Simkovich, G., *Electrical Conductivity and Seebeck Voltage of Fe_2O_3, Pure and Doped, as a Function of Temperature and Oxygen Pressure.* Solid State Ionics, 1984. **12**: p. 271-276.
36. Millot, F. and Niu, Y., *Diffusion of O^{18} in Fe_3O_4: an experimental approach to study the behavior of minority defects in oxides.* J. Phys. Chem. Solids, 1997. **58**(1): p. 63-72.
37. Lewis, G.V., Catlow, C.R.A., and Cormack, A.N., *Defect Structure and migration in Fe_3O_4.* J. Phys. Chem. Solids, 1985. **46**(11): p. 1227-1233.
38. Amami, B., Addou, M., and Monty, C., *Selfdiffusion and Point Defects in Iron Oxides: FeO, Fe3O4, alpha-Fe2O3.* Defect and Diffusion Forum, 2001. **194-199**: p. 1051-1056.
39. Gardner, R.F.G., Sweett, F., and Tanner, D.W., *The electrical properties of alpha ferric oxide--II. : Ferric oxide of high purity.* Journal of Physics and Chemistry of Solids, 1963. **24**(10): p. 1183-1186.
40. Catlow, C.R.A., et al., *Theoretical Calculation of the Energies of Defect Formation and Migration in alpha-Fe2O3 and alpha-Cr2O3.* Cryst. Latt. Def. and Amorph. Mat., 1987. **15**: p. 75-80.
41. Toney, M.F., et al., *Atomic Structure of the Passive Film Formed on Iron.* Physical Review Letters, 1997. **79**(21): p. 4282-4285.
42. Hendy, S.C., Laycock, N.J., and Ryan, M.P., *Atomistic Modeling of Cation Transport in the Passive Film on Iron and Implications for Models of Growth Kinetics.* Journal of The Electrochemical Society, 2005. **152**(8): p. B271-B276.
43. Grosvenor, A.P., et al., *Use of QUASES/XPS measurements to determine the oxide composition and thickness on an iron substrate.* Surf. Interface Anal., 2004(36): p. 632-639.

Chapter 5

Applying the Experimental Data for the Development of a PDM for Iron Oxide Growth

5.1 Abstract

In this chapter, a PDM accounting for oxygen vacancies only, is derived. The model is then used to test the hypothesis that only oxygen vacancies are present in the film. It is shown that an oxygen vacancy model is not capable of describing the oxide formed on iron. Therefore, iron interstitials (the other donor-type defect) must be present. A model containg both defects, along with a Warburg impedance is used to describe the growth of the oxide on iron. Kinetic parameters for the model are obtained for various formation potentials and temperatures in order to allow for predictions concerning the damage incurred by the general corrosion of iron.

5.2 Deriving a PDM Containing Only Oxygen Vacancies

Up to this point, it is understood that the oxide formed on iron exhibits n-type behavior over the majority of the passive range. There are two defect types that can be responsible for this behavior, the oxygen vacancy and the iron interstitial. At this time,

the author knows of no methods for precisely identifying and quantifying the type(s) of defects present in a passive iron oxide film. Therefore, an attempt is being made to apply the PDM to help implicitly identify the type(s) of defects present in the film. Based on the evidence shown in the last chapter, cation vacancies can be considered to be minority defects at most over the bulk of the passive range. This eliminates the two reactions involving cation vacancies in the general PDM depicted in Figure **3-2**. There remain five possible reactions which involve both oxygen vacancies and iron interstitials. To help determine if oxygen vacancies are the only defects present in the film (despite the general understanding that oxygen vacancies are considered to be minority defects, based on high temperature studies [1-3]), a PDM will be derived based on reactions III, VI, and VII in Figure **3-2**. According to this model, oxide growth is not possible without the formation of oxygen vacancies in reaction III. For it is by this reaction alone that oxide growth is believed to occur. Therefore, a PDM based upon this knowledge must include oxygen vacancies as a defect type in the film. If oxygen vacancies are the only defects present in the film then a model containing exclusively oxygen vacancies should be capable of predicting the impedance, steady-state current, and steady-state thickness for the film formed on iron. Another simplification can be made based on the knowledge that iron exists almost wholly in the 3+ state in the film as determined by XPS analysis. This eliminates the need to determine χ in the model. It should be noted that if any Fe^{2+} is present, it is located directly on the metal/film interface and is viewed as being the outermost monolayer of the metal phase.

The reaction responsible for film growth is displayed in Eq. **5.1** (rxn III in Figure **3-2)** and occurs at the metal/film interface. The two remaining reactions are

shown in Eq. **5.2** (rxn VII in Figure **3-2** corresponding to film dissolution) and Eq. **5.3** (rxn VI in Figure **3-2** where an oxygen vacancy reacts with water leaving an occupied oxygen site). The derivation used here follows the original work performed by Liu [4], but in the following work, the experimental evidence is incorporated during the derivation.

$$Fe \rightarrow Fe_{Fe} + \frac{3}{2}V_o^{\cdot\cdot} + 3e^- \qquad \textbf{5.1}$$

$$Fe_2O_3 + 3H^+ \rightarrow Fe^{3+} + \frac{3}{2}H_2O \qquad \textbf{5.2}$$

$$V_o^{\cdot\cdot} + H_2O \rightarrow O_O + 2H^+ \qquad \textbf{5.3}$$

From these reactions, the DC current can be accounted for as the flux of oxygen vacancies through the film and the simple equation is shown in Eq. **5.4**.

$$I = F\left[-2J_0^{\frac{m}{f}}\right] \qquad \textbf{5.4}$$

$$J_0 = -D_0\frac{\partial C_0}{\partial x} - 2KD_0C_0 \qquad \textbf{5.5}$$

The equation depicting the flux of oxygen vacancies through the film is shown in Eq. **5.5**. K=εF/RT, where ε is the electric field strength, F is the mole equivalent, R is 8.314 J/moleK and T is the temperature in Kelvin. Solving the continuity equation for $\delta C_o/\delta t = \nabla J_O$. Using the initial condition that $C_O(x)=C_O^O(x)$ at t=0 and B.C.'s at x=0 (film/soln), the equation becomes Eq. **5.6.**

$$J_0(0) = -\frac{3}{2} k_6^0 e^{a_6 V} C_0(0) \qquad \textbf{5.6}$$

At x=L, the flux of oxygen vacancies is represented by Eq. **5.7.**

$$J_0(L) = \frac{-3}{2} k_3^0 e^{a_3 V} e^{-b_3 L} \qquad \textbf{5.7}$$

The rate of change in the film thickness corresponds to the rate of growth of the film into the metal and the dissolution of the film at the solution interface. The equation for this is shown in Eq. **5.8.**

$$\frac{dL}{dt} = \Omega k_3^0 e^{a_3 V} e^{-b_3 L} - \Omega k_7^0 e^{a_7 V} C_{H^+} \qquad \textbf{5.8}$$

Because it has been shown that only Fe^{3+} is present in the film over region II (the passive range of interest), there is no change in the oxidation state of the iron upon dissolution. Therefore, there is no current generated by rxn VII, so the current is generated by rxn III only and can be written as: Eq. **5.9.** This reaction corresponds to the steady-state current for this model when a steady-state thickness is achieved. The steady state thickness is achieved when the rate of generation and rate of dissolution of film are equal (rxn III and rxn VII). The solution for this (for a PDM containing only oxygen vacancies) is shown in Eq. **5.10**, where the explanations for the symbols are provided below Eq. **5.29**.

$$I = F\left[3k_3^0 e^{a_3 V} e^{-b_3 L}\right] \qquad \textbf{5.9}$$

$$L_{ss} = \frac{(1-\alpha)}{\varepsilon} E_{app} - \frac{1}{\alpha_2 \chi K} \ln\left(\frac{k_5^{00}}{k_3^{00} e^{-\alpha_3 \beta \gamma pH} e^{-\alpha_3 3 \gamma \Phi_{f/s}^0}} C_{H^+}^n\right) \quad \textbf{5.10}$$

Current density is now a function of (V, L) and is shown in Eq. **5.11**. For impedance measurements, the variations are sinusoidal as shown in Eq. **5.13** and Eq. **5.12,** where the Δ L and ΔV are the amplitudes of the sinusoidal fluxuations.

$$\delta I = \left(\frac{\partial I}{\partial V}\right)_L \delta V + \left(\frac{\partial I}{\partial L}\right)_V \quad \textbf{5.11}$$

$$\delta L = \Delta L e^{j\omega t} \quad \textbf{5.12}$$

$$\delta V = \Delta V e^{j\omega t} \quad \textbf{5.13}$$

The Faradaic admittance can then be written as: Eq. **5.14.** The admittance is used here because the equations were derived for a steady-state current and using the admittance simplifies the process because it is found in the numerator. However, the fitting parameters will lead to the same outcome, whether it is impedance or admittance. In the end the impedance can be calculated and used to compare to the data.

$$Y_f = \frac{\delta I}{\delta V} = I^V + I^L \left(\frac{\Delta L}{\Delta V}\right) \quad \textbf{5.14}$$

Where $I^V = \left(\frac{\partial I}{\partial V}\right)_L$ and $I_L = \left(\frac{\partial I}{\partial L}\right)_V$. Now, the ΔL/ΔV term needs to be solved for. To do this, the relaxation in the film thickness must be solved for and is shown in Eq. **5.15.**

$$\frac{d}{dt}(\delta L) = \Omega k_3^0 a_3 e^{a_3 V} e^{-b_3 L} \delta V - \Omega k_3^0 b_3 e^{a_3 V} e^{-b_3 L} \delta L - \Omega k_7^0 a_7 e^{a_7 V} C_{H^+}^n \delta V \quad \textbf{5.15}$$

Considering that $\frac{d}{dt}(\delta L) = j\omega \Delta L e^{j\omega t}$, Eq. **5.15** becomes: Eq. **5.16**

$$j\omega \Delta L e^{j\omega t} = \Omega\left(k_3^0 a_3 e^{a_3 V} e^{-b_3 L} - k_7^0 a_7 e^{a_7 V} C_{H^+}^n\right)\Delta V e^{j\omega t} - \Omega k_3^0 b_3 e^{a_3 V} e^{-b_3 L} \Delta L e^{j\omega t} \qquad \textbf{5.16}$$

Solving for ΔL/ΔV and simplifying by multiplying by the complex conjugate in the denominator and numerator: Eq. **5.17**

$$\frac{\Delta L}{\Delta V} = \frac{\Omega\left(k_3^0 a_3 e^{a_3 V} e^{-b_3 L} - k_7^0 a_7 e^{a_7 V} C_{H^+}^n\right)}{\Omega k_3^0 b_3 e^{a_3 V} e^{-b_3 L} + j\omega} \qquad \textbf{5.17}$$

Simplifying further, Eq. **5.18**

$$\frac{\Delta L}{\Delta V} = \frac{\Phi_2}{1 + j\omega\tau_2} \qquad \textbf{5.18}$$

Where, Eq. **5.19**

$$\Phi_2 = \left(\frac{a_3}{b_3}\right) - \left(\frac{k_7^0}{k_3^0}\right)\left(\frac{a_7}{b_3}\right) e^{(a_7 - a_3)V} e^{b_3 L} C_{H^+}^n \qquad \textbf{5.19}$$

So that the admittance finally becomes: Eq. **5.20.**

$$Y_f = 3F\left[a_3 k_3^0 e^{a_3 V} e^{-b_3 L} - b_3 k_3^0 e^{a_3 V} e^{-b_3 L}\left(\frac{\Phi_2}{1 + j\omega\tau_2}\right)\right] + j\omega C \qquad \textbf{5.20}$$

Solving for the real and imaginary parts of the admittance yields Eq. **5.21** and Eq. **5.22**.

$$Y_{f(real)} = 3F(a_3 k_3^0 e^{a_2 V} e^{-b_3 L} - \frac{\Phi_2 b_3 k_3^0 e^{a_3 V} e^{-b_3 L}}{1 + \omega^2 \tau_2^2} \qquad \textbf{5.21}$$

$$Y_{f(imag)} = 3F\left(\frac{(\Phi_2 \tau_2 \omega) b_3 k_3^0 e^{a_3 V} e^{-b_3 L}}{1 + \omega^2 \tau_2^2} + \omega C\right) j \qquad \textbf{5.22}$$

Using the following reaction rate constants and parameters (Eq. **5.23,** Eq. **5.24,** Eq. **5.25,** Eq. **5.26,** Eq. **5.27,** Eq. **5.28,** Eq. **5.29**), the film admittance/impedance can be described for a PDM containing only oxygen vacancies.

$$k_3^0 = k_3^{00} e^{-\alpha_3 \beta \gamma pH} e^{-\alpha_3 3 \gamma \Phi_{f/s}^0} \quad \textbf{5.23}$$

$$k_6^0 = k_6^{00} e^{\alpha_6 \beta \gamma pH} e^{2\alpha_6 \gamma \Phi_{f/s}^0} \quad \textbf{5.24}$$

$$k_7^0 = k_7^{00} \quad \textbf{5.25}$$

$$\Phi_{f/s} = \Phi_f - \Phi_s = \alpha V + \beta pH + \Phi_{f/s}^0 \quad \textbf{5.26}$$

$$\Phi_{m/f} = (1-\alpha)V - \varepsilon L - \beta pH - \Phi_{f/s}^0 \quad \textbf{5.27}$$

$$\alpha = \frac{d\Phi_{f/s}}{dV} = 0.728 \quad \textbf{5.28}$$

$$\beta = \frac{d\Phi_{f/s}}{dpH} \quad \textbf{5.29}$$

The k_i^{00}'s are the standard rate constants (taking pH into account), the α_i's are the charge-transfer coefficients, γ is F/RT, Φ is the potential (with subscripts m for metal, f for film, s for solution, and the superscript ^{0} implies that it is for standard conditions), α(no subscript) refers to the dependence of the potential drop on formation potential, ε is the electric field strength (1.1e6 V/cm [4, 5]), and β represents the dependence of the potential drop at the film/solution interface on pH.

It is now evident why decreasing the amount of unknowns is essential for the use of the PDM. By using the experimental evidence, the only current generating reaction is that of rxn III (film formation). If the above impedance equation, containing all of the reaction rate constants and parameters, is fitted to the impedance data on iron, values for the unknowns can be obtained. Then from these values, the steady state thickness and current values can be calculated. If the values agree with those measured experimentally, this model is viable for describing the passivity of iron and yields some insight into the defect type present in the film. An equivalent circuit model, which includes the faradaic impedance, is shown in Figure **5-1. Eq. 5.30** displays the total impedance (Z_T) for this circuit. The equivalent circuit model accounts for all mechanisms contributing to the impedance of the system. However, the user can choose to include any/all elements in the fitting process.

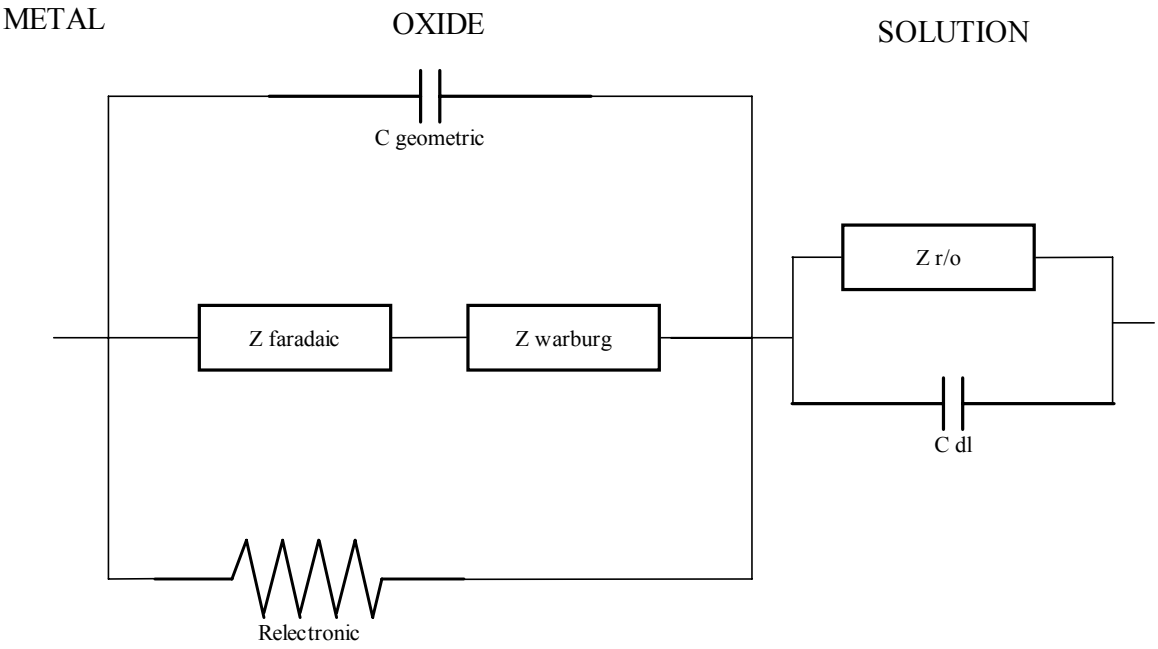

Figure **5-1**: Figure depicting the equivalent circuit used to model the impedance for iron in borate buffer system. The faradaic impedance represents the impedance as derived by the PDM. The Z r/o represents the impedance due to charge transfer at the oxide solution interface and Cdl is the double layer capacitance. The electronic resistance is used to account for any leakage currents (electons/holes) that might occur through the film. All elements are included in this equivalent circuit model, but the actual fits allow for all, or a few of the elements, to be used during the fit.

$$Z_T = \frac{1}{(Z_f + Z_w)^{-1} + R_{e,h}^{-1} + j\omega C_g} + \frac{1}{Z_{R/O}^{-1} + j\omega C_{dl}} \qquad \textbf{5.30}$$

In Eq. **5.30** the faradaic impedance is represented as Z_f, the resistance to a leakage current is $R_{e,h}$ (viewed as a simple resistance to the motion of electrons and holes through the film), the impedance to charge transfer at the film/solution interface is shown as $Z_{R/O}$, and the geometric and double layer capacitance are represented by C with subscripts "g" and "dl", respectively. The angular frequency is ω and the Warburg impedance is represented by Z_w. The Warburg impedance accounts for diffusion of defects through the

film and is shown in Eq. **5.31 ,** where σ is referred to as the Warburg coefficient. The Warburg coefficient is related to the diffusivities of the defects as shown in Eq. **5.32,** where n is the charge on the defect, A is the surface area of the iron exposed to solution, F is Faraday's constant and D and C represent the diffusion constant and concentration of the defects in the film, respectively. For films containing more than one defect, you would simply sum the term in the parenthesis for each individual defect present in the film. However, we are only concerned about the effective diffusion constant (D_{eff}) and at this time cannot quantify the different concentrations of the various defects in the film.

$$Z_W = \left(\frac{(1-j)}{\sqrt{\omega}} \right) \sigma \qquad \textbf{5.31}$$

$$\sigma = \frac{RT}{n^2 F^2 A \sqrt{2}} \left(\frac{1}{\sqrt{D_{eff} C_{eff}}} \right) \qquad \textbf{5.32}$$

5.3 Fit Results for the Oxygen Vacancy PDM

DataFit 8.0 was used to perform a non-linear fit on the equation to the impedance data. Figure **5-2** and Figure **5-3** show a fit to the data for a PDM containing only the oxygen vacancies for a film formed at +0.4 V_{SCE} for 24 hours. Fits were made for films grown at 0.0 V, 0.2 V, 0.4 V, and 0.6 V across region II in the passive region with results consistent with those shown in Figure **5-2**. A fit was performed on the data for a film

formed at 0.8 V as well, but as can be predicted by looking at the impedance at 0.8 V, the fit did not yield any sensible parameters. The values obtained from a PDM containing only the oxygen vacancy defects in the film, at 21° C (measured room temp.), are shown in Table **5-1**.

The sensitivity factor shown in the table is actually, the p-value (probability value) shown in the Datafit software, is calculated by using the null hypothesis for a parameter value. In other words if the parameter value was zero, what effect would it have on the standard error for the fit? Written out, the p-value is shown in Eq. **5.33.**

$$p-value = \frac{s\tan dard\ error\ for\ fit\ with\ the\ actual\ fitted\ parameter\ value}{s\tan dard\ error\ for\ fit\ with\ the\ fitted\ parameter\ set\ to\ zero} \qquad \textbf{5.33}$$

The standard error is normalized, yielding a value between zero to one. Therefore, the sensitivity factor measures the probability that a particular parameter is zero. The sensitivity factor can range from zero to one, where zero corresponds to a 0 % chance that the parameter is zero and one corresponds to a 100% probability the parameter is zero and it has no effect on the fit. It should be noted that some of the parameters are very small to begin (i.e. k_2^{oo} is in the 10^{-15} range) and this may affect the sensitivity factor some.

The results shown in Table **5-1** contain all parameters from the equivalent circuit shown in Figure **5-1**, including the faradaic impedance as derived above. The equivalent circuit parameters, excluding those for the faradaic impedance, were held in the range one would typically expect them to be. Satisfactory fits were obtained for each formation potential and the parameters are in the ranges appropriate for the system. The transfer

coefficient has a value between zero and one, the standard rate constants are in the typical range for electrochemical reactions, and the dependence on the potential drop with voltage and pH is small. However, the resulting values for the steady-state currents, thicknesses, and vacancy diffusivities (as calculated using the parameters) could not be combined in a manner to yield rational description of the film growth. The fit yielded negative thicknesses, very small currents, and diffusivities in the 10^{-6} cm^2/sec range (too large of a value for a solid). This is most likely due to the fact that the only current generating reactions is that for film formation, where oxygen vacancies are generated, and film dissolution. In order to increase the current and thickness, the reaction rate constants (k_3^{oo} and k_7^{oo}) would need to be increased. Upon increasing the reaction rate constants, it was noted that either the thickness or the current would become excessively large. In the end, the best fits seemed to yield negative values for thickness and extremely low steady state current values. In addition, using the Warburg impedance in the fit yielded extremely high values for the vacancy diffusivities (expected to be in the range of 10^{-16} cm^2/sec[6, 7]). Attempts were made to fit data for the 50° C and 75° C temperatures. The fits for measurements made at 50° C resulted in similar findings and the parameters generated for fits at 75° C were very poor.

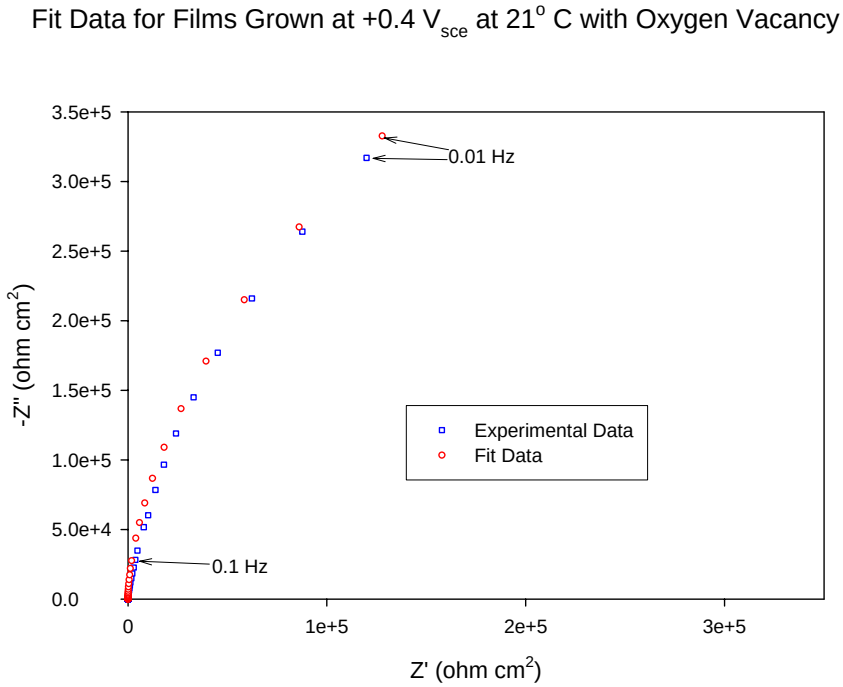

Figure **5-2**: Nyquist plot showing the fit for a PDM containing only oxygen vacancies. Films were grown for 24 hours at each formation potential prior to impedance measurements.

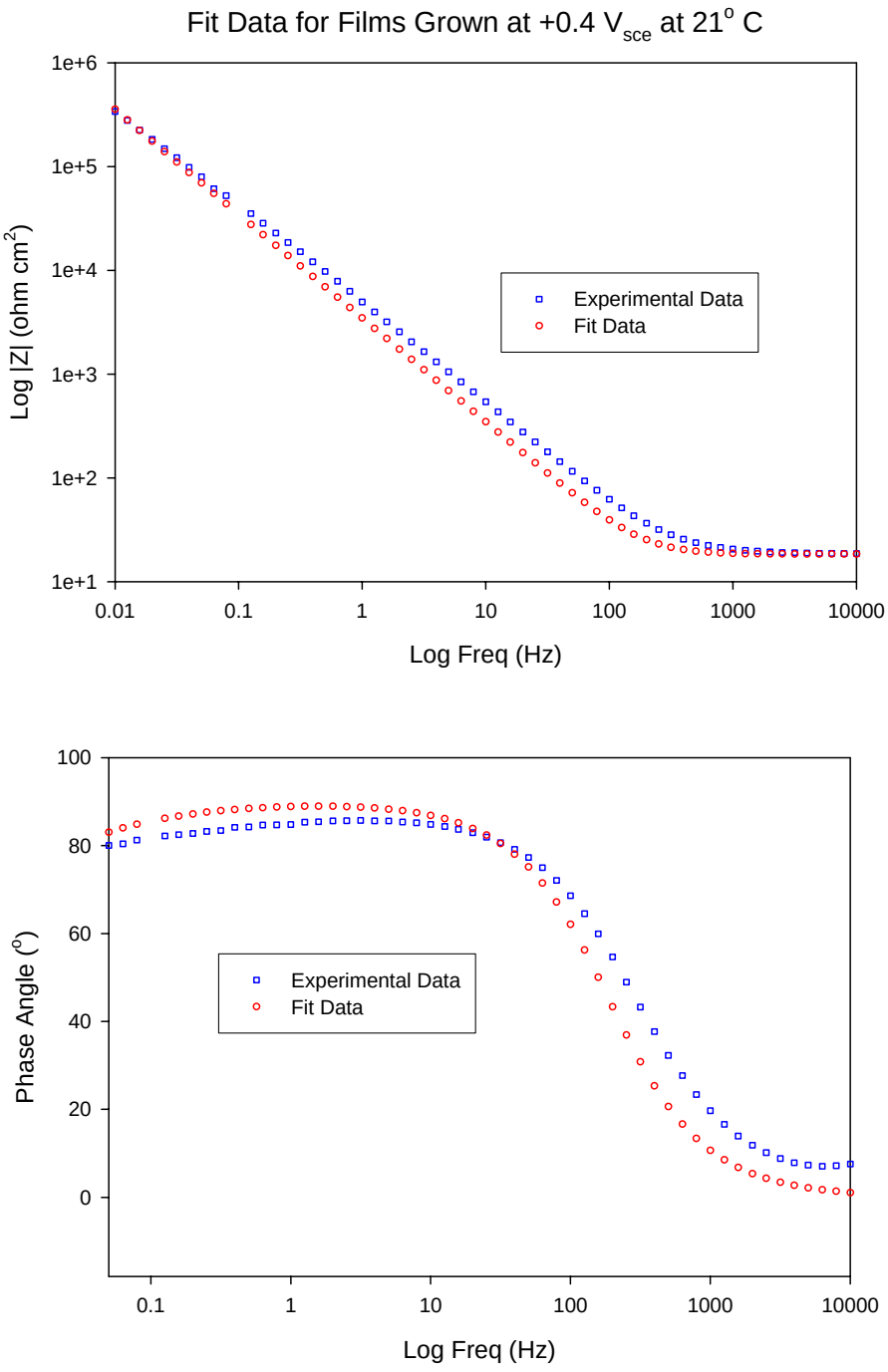

Figure **5-3**: Bode plot showing the fit for a PDM containing only oxygen vacancies. Films were grown for 24 hours at each formation potential prior to impedance measurements.

Table **5-1**: Table listing fitting parameters for films grown at various formation potentials across Region II of the passive region at 21° C. The mean represents the average value for all potentials for the model. The steady state thickness (L_{SS}), current (I_{SS}), and oxygen vacancy diffusion constant (D_W from the Warburg impedance) were calculated for each potential and are shown at the bottom of the table. The sensitivity factor is used to determine the importance of a parameter on the fit (its value can range from 0 (less likely that the parameter is actually 0) to 1 (the parameter in question has a value close to 0 and can be removed).

E_{app} / V_{SCE}	**0**	**0.2**	**0.4**	**0.6**	**Mean**	**Sensitivity factor**
Dielectric constant	30	30	30	30	30	Constant
T(K)	298	298	298	298	298	Constant
pH	8.4	8.4	8.4	8.4	8.4	Constant
C_{dl} (F/cm^2) Double layer capacitance	1.05E-05	8.99E-06	9.99E-06	1.01E-05	9.89E-06	.12
R_e(Ωcm^2) Electronic resistance	1E+08	1E+08	1E+08	1E+08	1E+08	Constant
R_s(Ωcm^2) Solution resistance	9.4	9.4	9.4	9.4	9.4	Constant
α_3 Transfer coefficient	0.10	0.03	0.07	0.13	0.08	.35
k_3^{oo} (mol/cm^{2}s) Standard rate constant	1.01E-16	9.9E-15	5.24E-15	4.84E-15	5.02E-15	.54
k_7^{oo} (mol/cm^2 s) Standard rate constant	9.19E-07	1.01E-06	9.16E-07	5.19E-07	8.41E-07	.32
β (V) Dependence of potential drop across m/oxide interface	0.0036	0.0096	0.0062	0.036	0.0139	.27
Φf/s in the standard state (V=0, pH=0)	-0.30	-0.29	-0.15	-0.05	-0.20	0.2
Lss (cm) Steady state thickness	**1.27E-7**	**1.14E-7**	**-2.7E-7**	**-5.1E-7**		**calculated**
Iss (A/cm^2) Steady state current density	**4.18E-8**	**4.18E-8**	**3.48E-8**	**3.53E-8**		**calculated**
D_{eff} (cm^2/s) Diffusivity of principal defect.	**5.05E-6**	**4.29E-07**	**8.9E-6**	**1.30E-06**		**Calculated**

Although this model is capable of obtaining quality fits to the data, if fails to render either meaningful parameter values or predict suitable physical values for the steady state current and thickness. Therefore, one can implicitly assume that there must be another defect present in the film to account for this disagreement. This assumption in and of itself is nothing new, previous researchers [4, 6-11] have used some of the experimental evidence to arrive at the conclusion that the film contains oxygen vacancies and iron interstitials (both can cause the film to exhibit n-type behavior). However, no researchers have attempted to use a model to deduce the defect type or types present in the film. Therefore, the fact that an oxygen vacancy PDM cannot describe or predict the physical characteristics of the film leads to the conclusion that other defects must be present. As expressed by Liu's model [4], originally derived by Macdonald in unpublished work on iron, oxygen vacancies and iron interstitials are included. Therefore, the oxygen vacancy and iron interstitial containing PDM is being adapted for application to the iron-borate system as a function of temperature.

5.4 Including Iron Interstitials and Oxygen Vacancies to Describe Iron Oxide Film Growth

As stated, Macdonald's original derivation of a PDM for iron, containing both iron interstitials and oxygen vacancies, is going to be used to describe the oxide growth on iron as a function of temperature. Macdonald's model, used by Liu, was derived to account for the oxide growth on iron at one temperature [4], however, some minor changes to the model, used in Liu's work,make it possible to quickly assess the oxide

growth for a range of temperatures. In this work, that model was adjusted such that the temperature now becomes a parameter that can easily be input as a parameter. In addition, the model was used as a stand alone model and the measured impedance was understood to be derived from the faradaic impedance only. Therefore, the equivalent circuit in Figure **5-1** is going to be used and the faradaic impedance will be placed in the circuit as was done in the previous section. Since the derivation has already been performed, it will not be shown here, only the data fits will be reviewed in this section.

The Nyquist plots, showing the fit results for the three temperatures, for films grown at +0.4 V_{SCE} are shown next. The Nyquist/Bode plots for 21° C, 50° C and 75° C are shown in Figure **5-4/** Figure **5-5**, Figure **5-6/Figure 5-7,** and Figure **5-8/** Figure **5-9,** respectively.

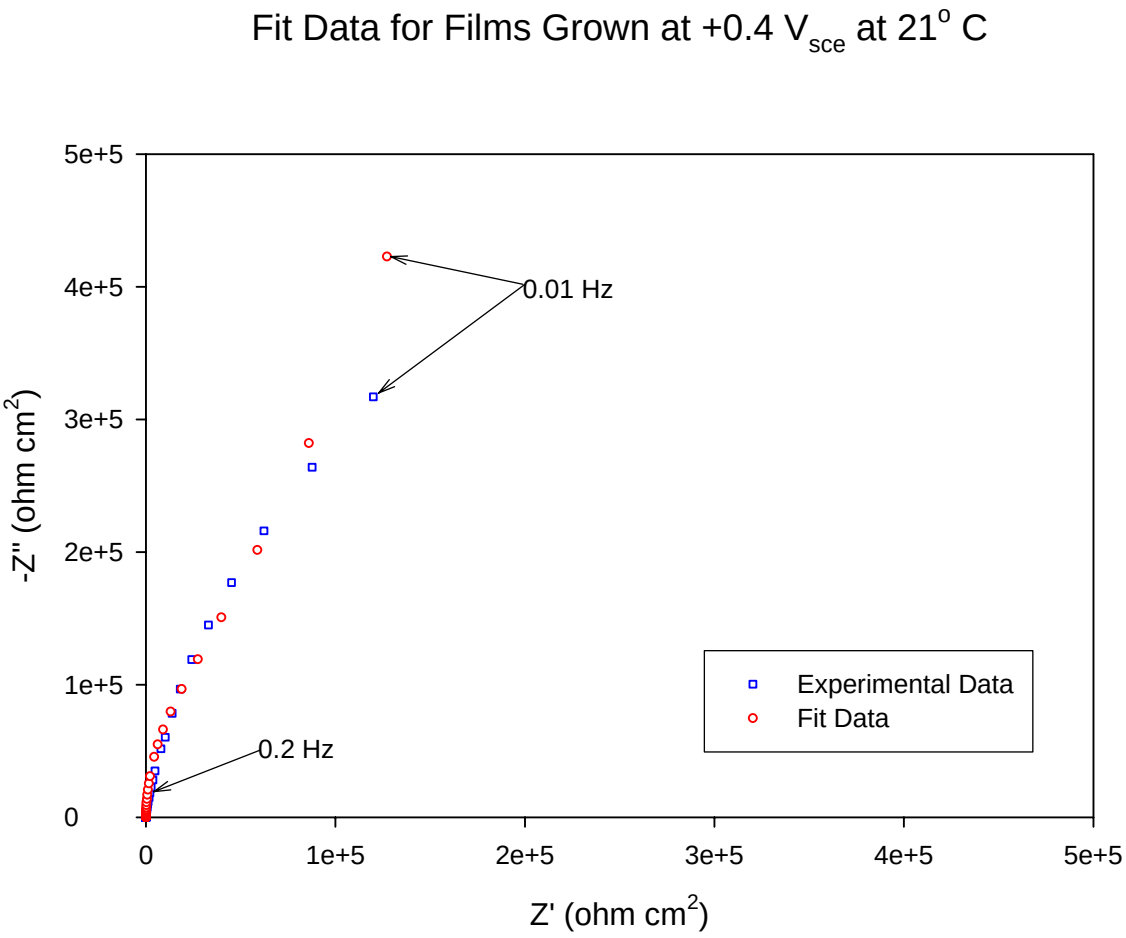

Figure **5-4**: Nyquist plot showing the fit for a PDM containing oxygen vacancies and iron interstitials at 21° C. Films were grown for 24 hours at each formation potential prior to impedance measurements.

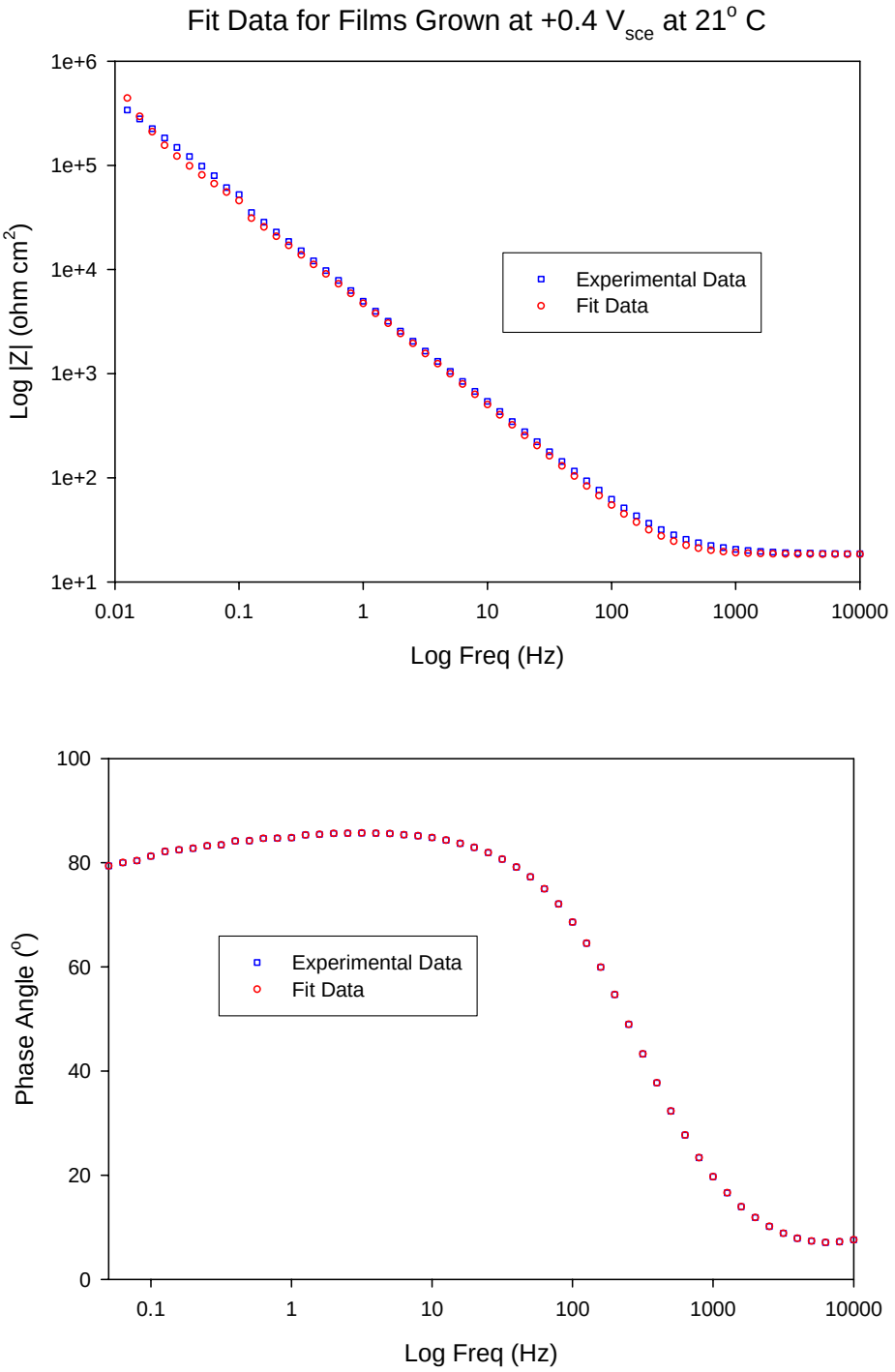

Figure **5-5**: Bode plot showing the fit for a PDM containing oxygen vacancies and iron interstitials at 21° C. Films were grown for 24 hours at each formation potential prior to impedance measurements.

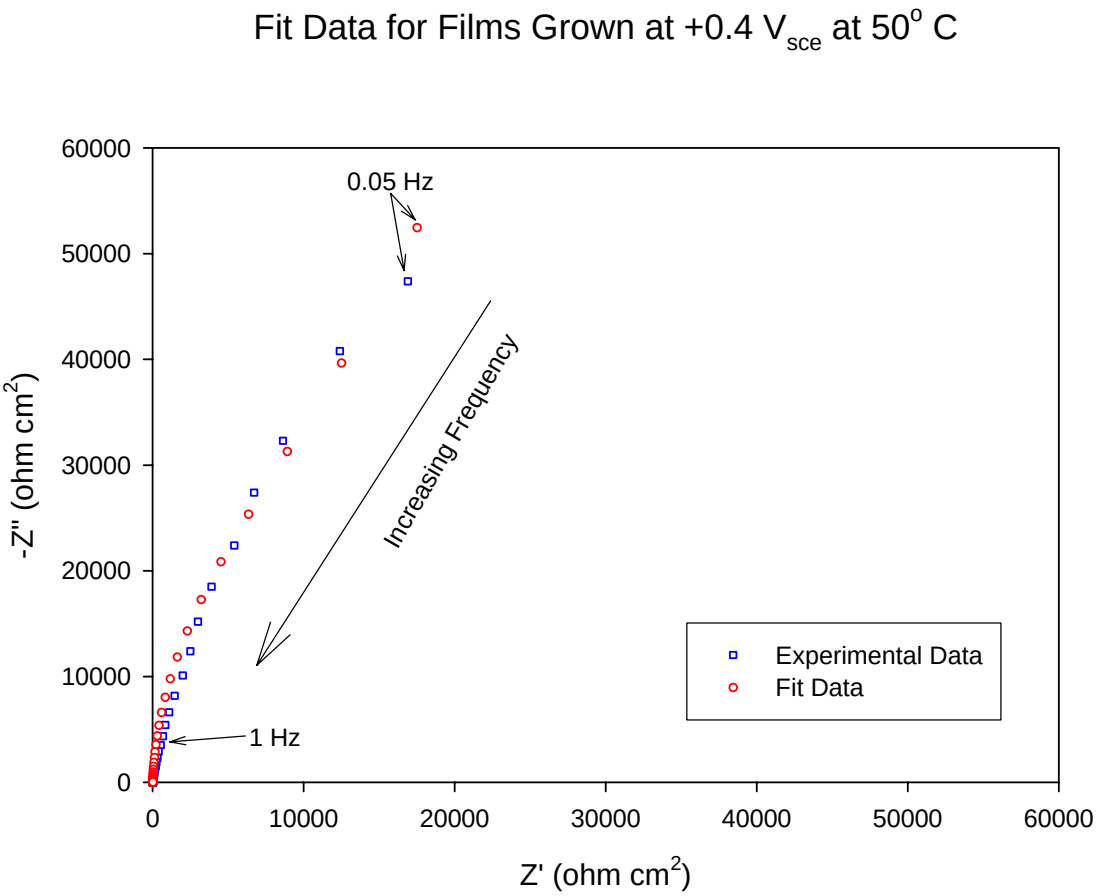

Figure **5-6**: Nyquist plot showing the fit for a PDM containing oxygen vacancies and iron interstitials at 50° C. Films were grown for 24 hours at each formation potential prior to impedance measurements.

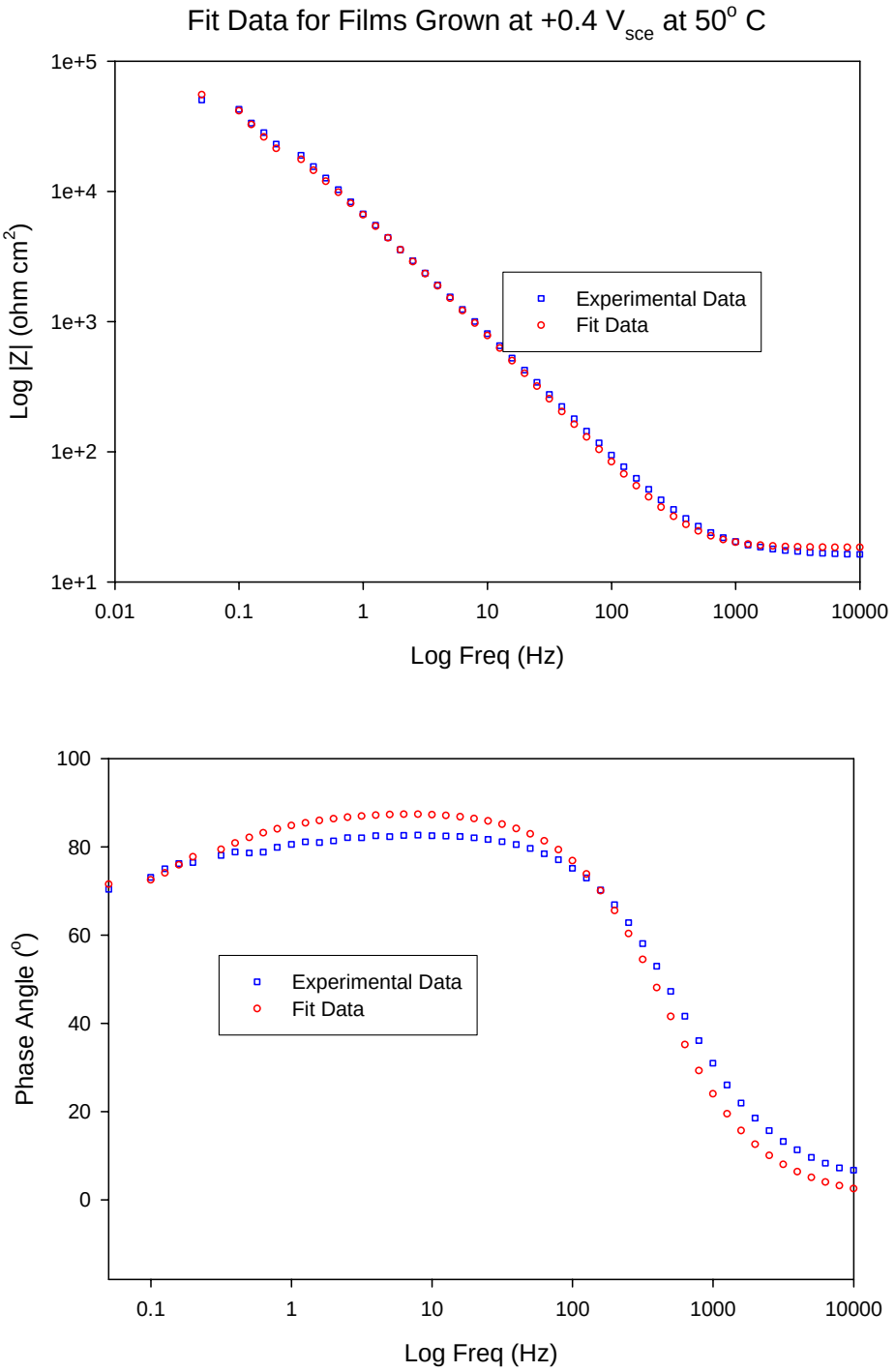

Figure **5-7**: Bode plot showing the fit for a PDM containing oxygen vacancies and iron interstitials at 50° C. Films were grown for 24 hours at each formation potential prior to impedance measurements.

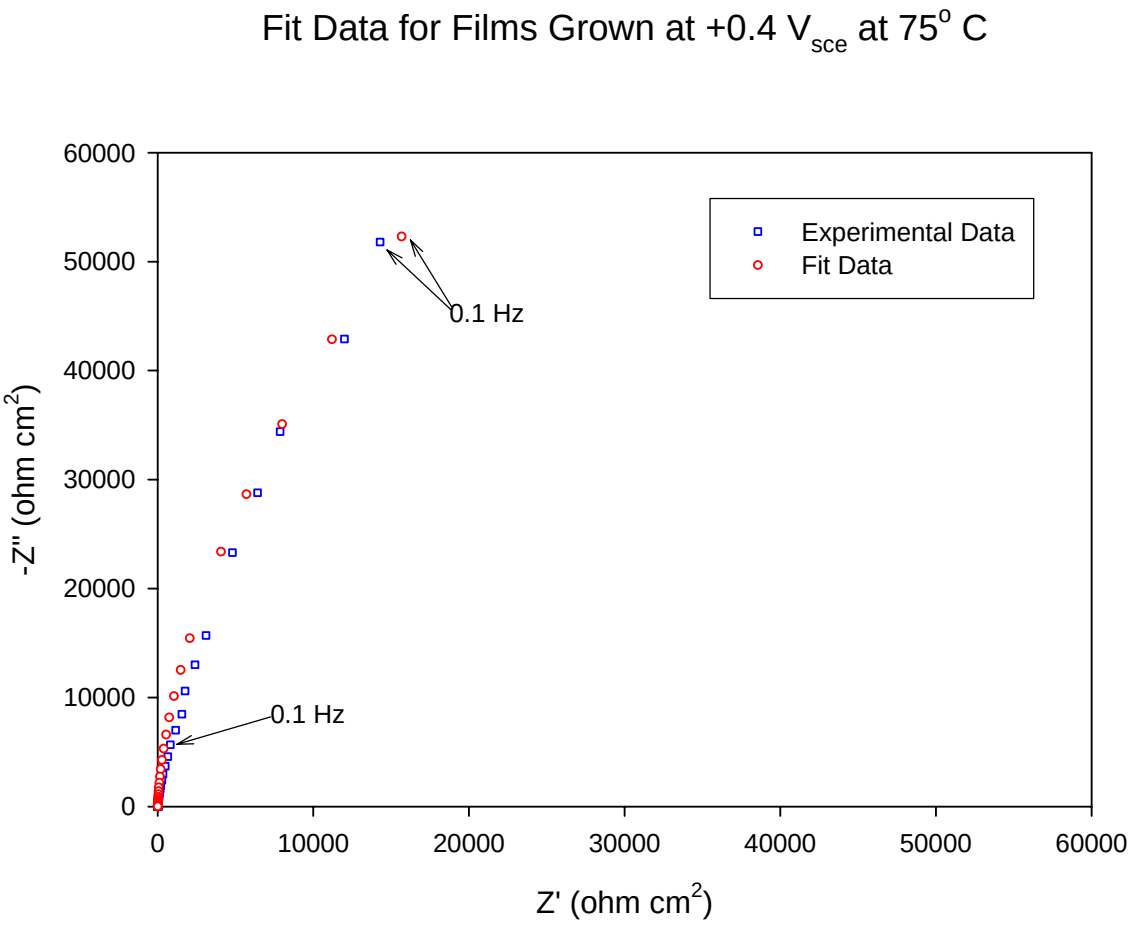

Figure **5-8**: Nyquist plot showing the fit for a PDM containing oxygen vacancies and iron interstitials at 75° C. Films were grown for 24 hours at each formation potential prior to impedance measurements.

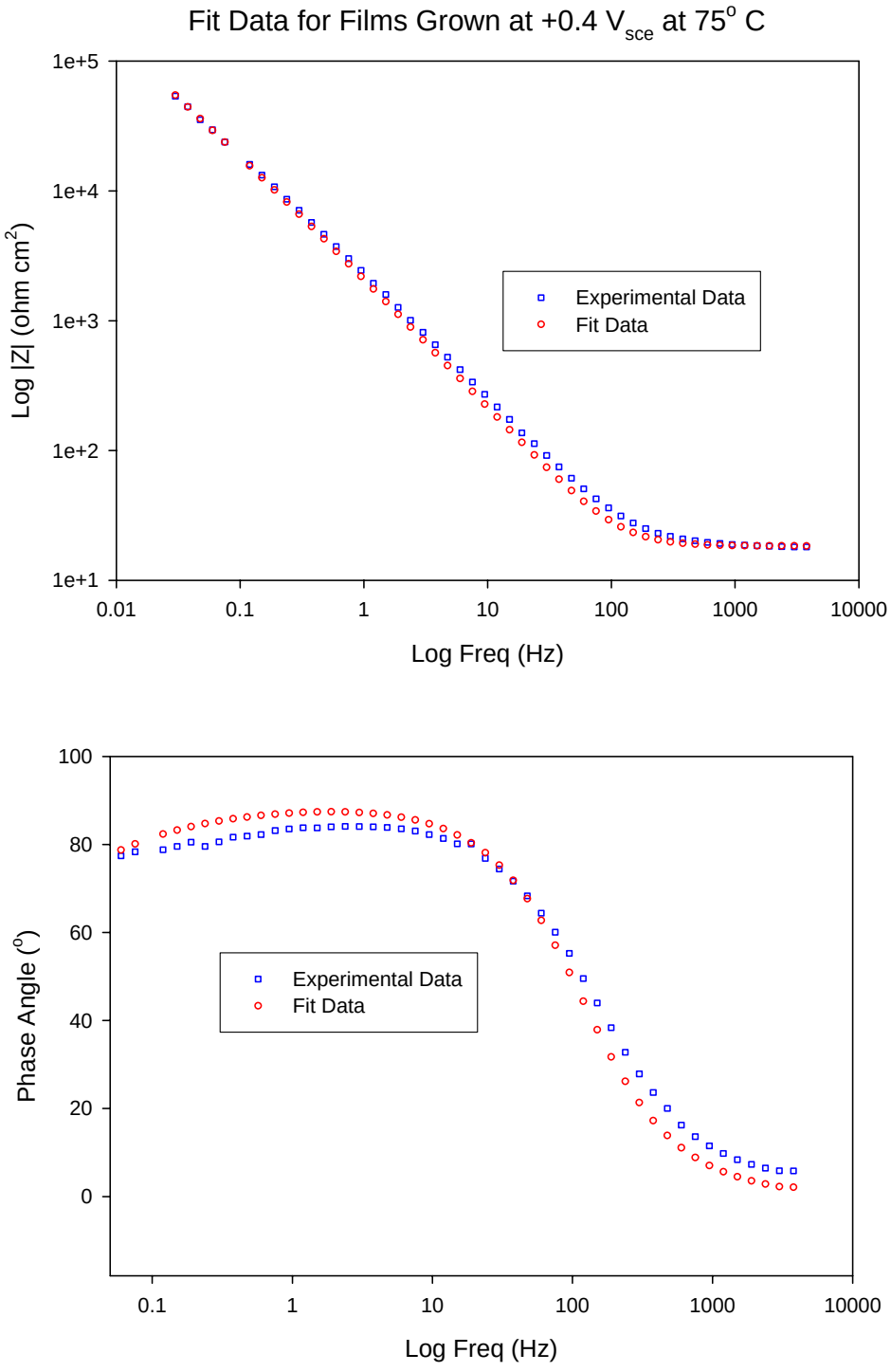

Figure **5-9**: Bode plot showing the fit for a PDM containing oxygen vacancies and iron interstitials at 75° C. Films were grown for 24 hours at each formation potential prior to impedance measurements.

Good fits were obtained for each of the temperatures and the results shown in the above figures are indicative of all of the fits obtained for each of the formation potential across region II in the passive range. The parameter values, as a function of formation potential and temperature, are displayed in the tables below. It should be noted that the circuit element values (i.e. C_{dl}, $R_{e,h}$, R_s, etc.) are not being displayed in the tables to prevent the tables from becoming too crowded. The typical range for these parameters are shown in Table **5-5.** This small change in magnitude did not have any major effect on the parameters related to the faradaic impedance. The parameters are shown as a function of formation potential for 21° C in Table **5-2**, 50° C in Table **5-3** and 75° C in Table **5-4**. The rate constants (k_i^{00}) and the charge transfer coefficients (α_i) are related to the reactions shown in Figure **3-2**, where "*i*" represents the reaction number in the figure (i.e. "i"= 2 is for rxn II in Figure **3-2**)

Table **5-2**: Table listing fitting parameters for films grown at various formation potentials across Region II of the passive region at 21° C. The mean represents the average value for all potentials for the model. The steady state thickness (L_{SS}), current (I_{SS}), and oxygen vacancy diffusion constant (D_W from the Warburg impedance) were calculated for each potential and are shown at the bottom of the table. The sensitivity factor has been explained in the last section.

E_{app} / V_{SCE}	0	0.2	0.4	0.6	Mean	Sensitivity factor
k_2^{00} (mol/cm^{2}s) Standard rate constant	1.27E-12	2.31E-12	2.22E-12	2.43E-12	1.27E-12	.43
k_3^{00} (mol/cm^{2}s) Standard rate constant	4.95E-16	7.10E-16	6.95E-15	8.79E-15	4.23E-15	.01
k_5^{00} (mol/cm^{2}s) Standard rate constant	5.25E-06	1.02E-07	1.79E-07	1.56E-07	1.42E-06	.13
k_7^{00} (mol/cm^2 s) Standard rate constant	1.02E-09	1.13E-09	1.12E-09	4.75E-10	9.36E-10	.27
α_2 Transfer coefficient	0.076	0.00033	0.00025	0.00033	0.019	.57
α_3 Transfer coefficient	0.25	0.63	0.28	0.63	0.44	.18
α_5 Transfer coefficient	0.363	0.44	0.41	0.44	0.41	.08
α_7 Transfer coefficient	0.261	0.25	0.25	0.25	0.25	.01
β (V) Dependence of potential drop across bl/ol interface	-0.00206	-0.001624	-0.00025	0.002	-0.00048	.03
$\phi_{f\|s}$ (V) in the standard state (V=0, pH=0)	-0.023	-0.018282	-0.0067	0.01	-0.0095	.05
L_{ss} (cm) Steady state thickness	**8.87E-08**	**1.14E-7**	**1.38E-7**	**1.59E-7**		**Calculated**
I_{ss} (A cm^{-2}) Steady state current density	**2.58E-07**	**4.46E-7**	**4.32E-7**	**4.73E-7**		**Calculated**
D_{eff} (cm^2/s) Diff of Principal Defect	**1.83E-16**	**4.74E-14**	**4.50E-16**	**4.44E-15**		**Calculated**

Table **5-3**: Table listing fitting parameters for films grown at various formation potentials across Region II of the passive region at 50° C. The mean represents the average value for all potentials for the model. The steady state thickness (L_{SS}), current (I_{SS}), and oxygen vacancy diffusion constant (D_W from the Warburg impedance) were calculated for each potential and are shown at the bottom of the table. The sensitivity factor has been explained in the last section.

E_{app} / V_{SCE}	0	0.2	0.4	0.6	Mean	Sensitivity factor
k_2^{00} (mol/cm^{2}s) Standard rate constant	1.38E-10	9.72E-11	1.21E-10	3.00E-10	1.64e-10	.32
k_3^{00} (mol/cm^{2}s) Standard rate constant	3.48E-15	4.28E-14	1.90E-12	2.34E-13	1.18E-13	.08
k_5^{00} (mol/cm^{2}s) Standard rate constant	5.25E-06	5.25E-06	1.22E-05	1.43E-06	6.03E-06	.05
k_7^{00} (mol/cm^2 s) Standard rate constant	1.83E-09	1.00E-09	8.10E-09	1.40E-10	2.77E-09	.38
α_2 Transfer coefficient	0.23	0.32	0.23	.32	0.28	.04
α_3 Transfer coefficient	0.27	0.27	0.27	.27	0.27	.12
α_5 Transfer coefficient	0.5	0.5	0.5	.5	0.5	.08
α_7 Transfer coefficient	0.26	0.26	0.26	.26	0.26	0.0
β (V) Dependence of potential drop across bl/ol interface	-0.003	-0.002	-0.001	-1.00E-03	-0.0018	.07
$\phi_{f\|s}$ (V) in the standard state (V=0, pH=0)	-0.036	-0.02	-0.02	-1.00E-02	-0.022	.01
L_{ss} (cm) Steady state thickness	**1.73E-07**	**2.64E-7**	**3.12E-7**	**3.69E-7**		**Calculated**
I_{ss} (A cm^{-2}) Steady state current density	**6.69E-06**	**6.69E-6**	**1.90E-6**	**1.10E-6**		**Calculated**
D_{eff} (cm^2/s) Diff of Principal Defect	**1.61E-15**	**5.30E-14**	**7.29E-14**	**3.02E-15**		**Calculated**

Table **5-4**: Table listing fitting parameters for films grown at various formation potentials across Region II of the passive region at 75° C. The mean represents the average value for all potentials for the model. The steady state thickness (L_{SS}), current (I_{SS}), and oxygen vacancy diffusion constant (D_W from the Warburg impedance) were calculated for each potential and are shown at the bottom of the table. The sensitivity factor has been explained in the last section.

E_{app} / V_{SCE}	0	0.2	0.4	0.6	Mean	Sensitivity factor
k_2^{00} (mol/cm^{2}s) Standard rate constant	1.90E-10	1.90E-10	1.98E-10	1.28E-10	1.77E-10	.29
k_3^{00} (mol/cm^{2}s) Standard rate constant	4.60E-14	9.60E-13	8.33E-13	3.00E-13	5.45E-13	.03
k_5^{00} (mol/cm^{2}s) Standard rate constant	1.65E-05	2.31E-05	1.48E-05	2.00E-05	1.86E-05	.12
k_7^{00} (mol/cm^2 s) Standard rate constant	1.44E-08	1.37E-09	1.67E-10	3.57E-10	4.07E-09	.26
α_2 Transfer coefficient	.032	.11	.008	.11	0.155	.01
α_3 Transfer coefficient	.27	.27	.27	.27	0.27	.00
α_5 Transfer coefficient	.5	.5	.5	.5	0.5	.00
α_7 Transfer coefficient	.26	.26	.26	.12	0.225	.04
β (V) Dependence of potential drop across bl/ol interface	-.003	-.003	-.0043	-.003	-0.0034	.12
$\phi_{f\|s}$ (V) in the standard state (V=0, pH=0)	-.02	-.012	-.036	-.02	-0.022	.11
L_{ss} (cm) Steady state thickness	**1.78E-07**	**3.89E-7**	**5.03E-7**	**5.09E-7**		**Calculated**
I_{ss} (A cm^{-2}) Steady state current density	**4.465E-06**	**3.96E-6**	**5.64E-6**	**2.13E-6**		**Calculated**
D_{eff} (cm^2/s) Diff of Principal Defect	**6.23E-14**	**3.90E-17**	**1.09E-11**	**1.28E-15**		**Calculated**

Table **5-5**: Type Caption Here

Parameter	Range of Values
σ (Warburg constant)	124,000 - 178,000
ε (dielectric constant)	24 - 58
$R_{e,h}$	8.0E+7 - 1.1E+8
$R_{R/O}$	9.4 - 18.9
C_{dl}	7.3E-6 – 1.5E-5

It should be noted that all of the parameter values in these tables are well within the limits that physically make sense. The next thing to notice is that the rate constant dealing with the oxygen vacancy formation and rate growth, k_3 (corresponding with rxn III), has the lowest value of the rate constants. This would indicate that the oxygen vacancies do play a role, but that the reactions involving the iron interstitials (rxns II and V) dominate due to the much larger rate constants (nearly double for k_5). It is also worth-while to mention that the injection of iron interstitials into the film (corresponding to rxn II) is much lower. This would give credence to the claim that if any Fe^{2+} is in the film, it forms slowly and is most likely located directly on the metal/film interface as was proposed earlier. Then, by rxn V, the Fe^{2+} readily oxidizes to Fe^{3+} (just by observing the magnitude of k_5), whereby it can more easily diffuse through the film and enter the solution. Although rxn V is shown to take place at the film/solution interface, there are no constraints in the model dictating that this particular reaction must occur at the interface. It is more likely that Fe^{2+} is oxidized in the film itself thus allowing for the easier diffusion of the smaller Fe^{3+} interstitial. Before finally comparing the current, thickness, and diffusivities predicted by this PDM, it is worth comparing the mean values for the reaction constants as a function of temperature. Table **5-6** shows the mean values

for the parameters for each of the temperatures being considered. The one observation to be made here is that the rate constants did increase with temperature overall (some more than others). The other parameters in the table remained relatively constant over the temperature range. The final thing then to consider is how well the predicted values agree with the measured ones.

Table **5-6**: Table displaying mean parameter values at the various temperatures.

E_{app} / V_{SCE}	Mean-21° C	Mean-50° C	Mean-75° C
k_2^{00} **(mol/cm^{2}s) Standard rate constant**	1.27E-12	1.64e-10	1.77E-10
k_3^{00} **(mol/cm^{2}s) Standard rate constant**	4.95E-16	1.18E-13	5.45E-13
k_5^{00} **(mol/cm^{2}s) Standard rate constant**	1.42E-06	6.03E-06	1.86E-05
k_7^{00} **(mol/cm^2 s) Standard rate constant**	1.02E-09	2.77E-09	4.07E-09
α_2 **Transfer coefficient**	0.076	0.28	0.155
α_3 **Transfer coefficient**	0.25	0.27	0.27
α_5 **Transfer coefficient**	0.363	0.5	0.5
α_6 **Transfer coefficient**	0.261	0.26	0.225
β **(V) Dependence of potential drop across bl/ol interface**	-0.00206	-0.0018	-0.0034
$\phi_{f\|s}$ **(V) in the standard state (V=0, pH=0)**	-0.023	-0.022	-0.022

The first parameter to consider is that of the effective diffusion coefficient. In order to consider the Warburg impedance as a vital part of the equivalent circuit, it should

at least be able to account for the diffusivities of the defects. The average values shown in the tables appear to range from 10^{-14} to 10^{-16} cm^2/sec. These values are approximately in the range as those reported by others [6, 12, 13]. Therefore, the incorporation of a Warburg impedance appears to be viable here.

The final test is to compare the steady-state thickness and current values to determine how well they match up with the measured values. Figure **5-10** shows the data for the steady-state thickness. It is clear that there is good agreement between the measured and calculated values. Figure **5-11** compares the steady-state current values at the various temperatures. While there is some difference between the measured and calculated values, the difference is only a factor off.

The PDM, containing iron interstitials and oxygen vacancies, is able to account for the oxide growth on iron. The parameter values obtained for the various temperature ranges make it possible to make future predictions concerning the general corrosion of iron in mildly basic solutions. The PDM can determine an oxide thickness and more importantly the steady-state current. This steady state current can then be used to calculate the damage accumulation due to corrosion in these environments. It is yet to be determined what role, if any, that pH (in the basic range) has on the corrosion rates. However, it has been shown that the reaction rates do increase with the temperature, as would be expected. The PDM also helps to point to what reactions play an important role in the corrosion of iron. Further studies into the effects of the conditions and environments on the individual reactions can provide valuable insight into the corrosion processes. This insight can then possibly be used to design alloys or coatings to prevent

corrosion, as well as indicate what environmental controls can aid in corrosion prevention.

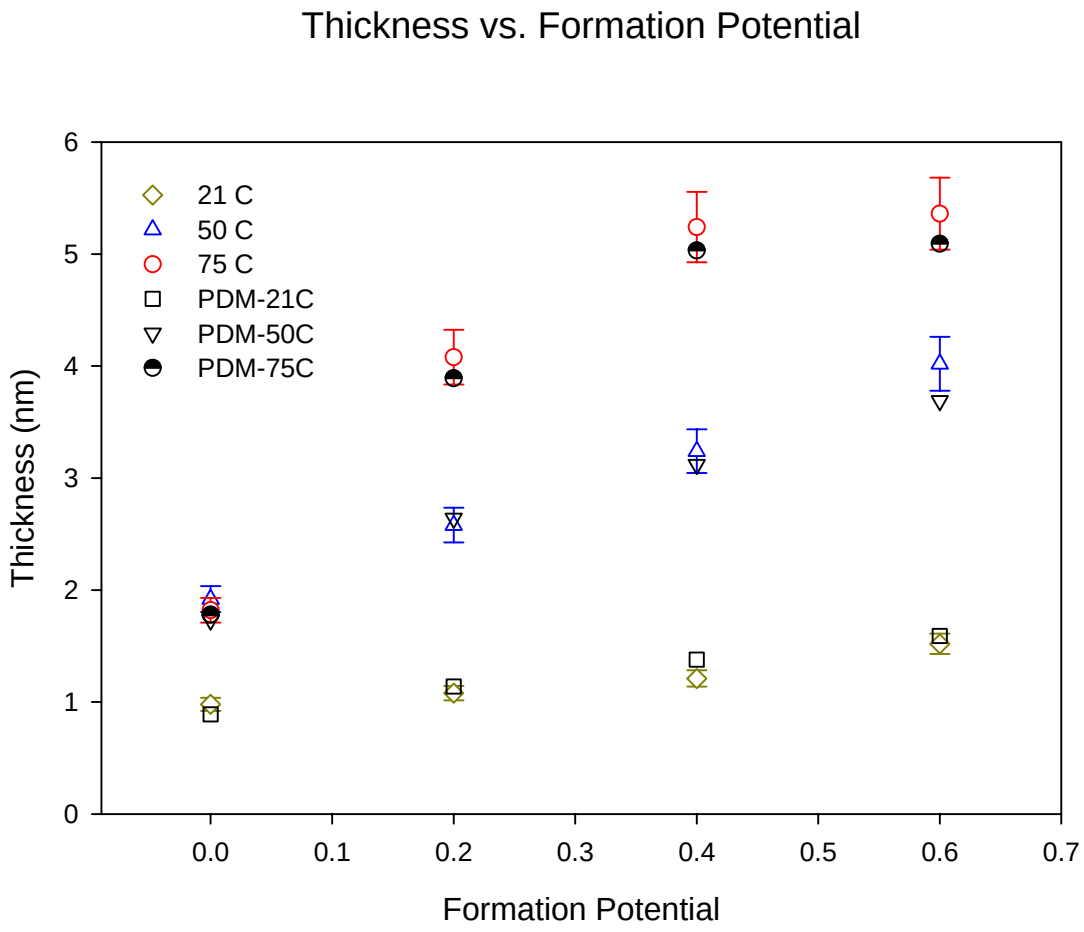

Figure **5-10**: Plot comparing the measured and calculated steady-state thickness values for the various temperatures.

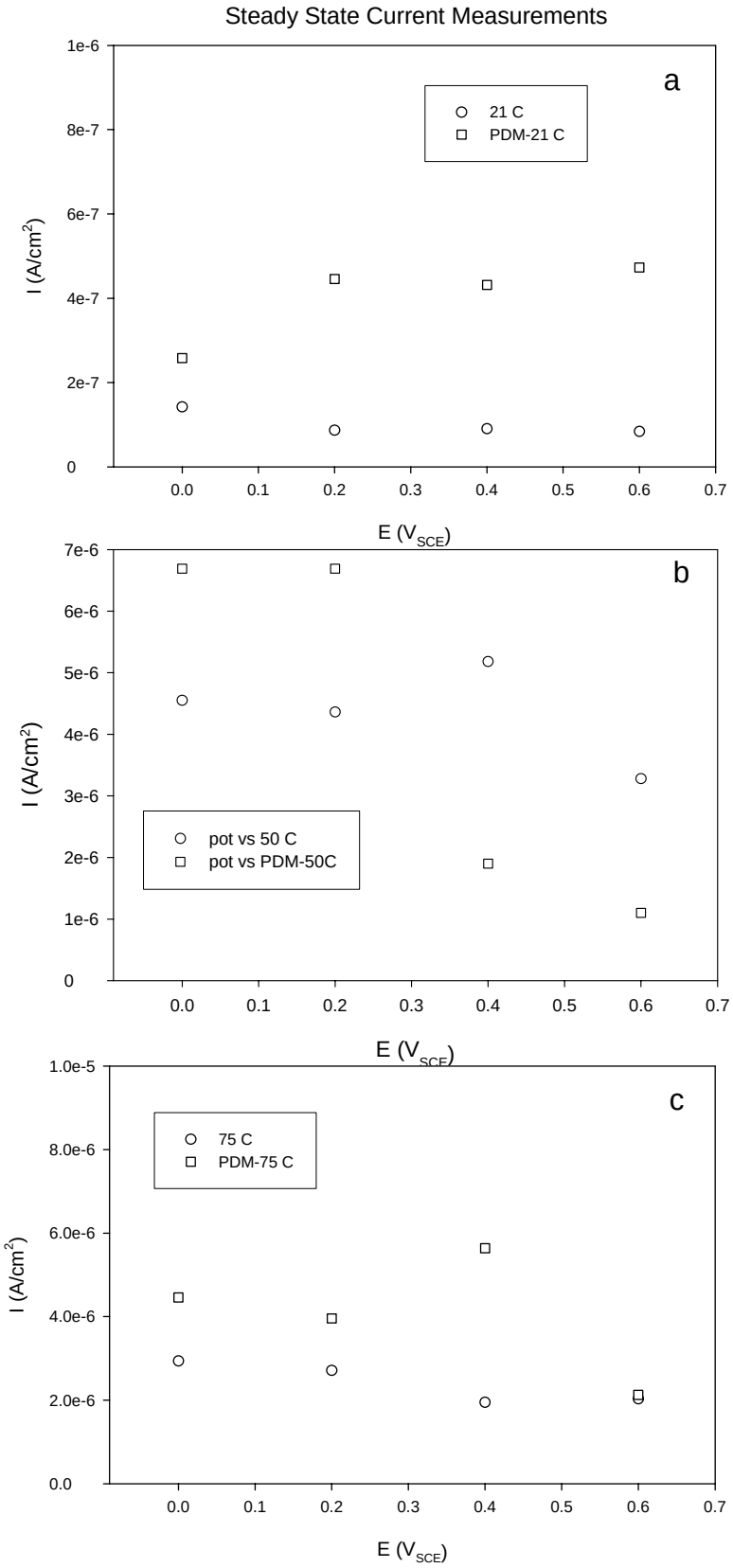

Figure **5-11**: Comparison of the steady-state current values at (a) 21° C, (b) 50° C and (c) 75° C.

5.5 References

1. Millot, F., et al., *Oxygen Self-Diffusion in Fe_3O_4: An Experimental Example of Interactions Between Defects.* Ber. Bunsenges. Phys. Chem., 1997. **101**(9): p. 1351-1354.
2. Ruckman, M.W., Chen, J., and Strongin, M.S., *Oxidation of iron films at 25 K and the reactive osidation of iron in solid oxygen.* Physical Review B, 1992. **45**(24): p. 273-278.
3. Sakisaka, Y., Miyano, T., and Onchi, M., *Electron-energy-loss-spectroscopy study of oxygen chemisorption and initial oxidation of Fe(100).* Physical Review B, 1984. **30**(12): p. 6849-6855.
4. Liu, J., *Electrochemical emmision and impedance spectroscopies of passive iron and carbon steel*, in *Material Science and Engineering*. 2002, Pennsylvania State University: University Park, PA. p. 170.
5. Chao, C.Y., Lin, L.F., and Macdonald, D.D., *A Point Defect Model for Anodic Passive Films I. Film Growth Kinetics.* J. Electrochem. Soc., 1981. **128**(6): p. 1187-1194.
6. Ahn, S. and Kwon, H., *Diffusivity of point defects in the passive film on Fe.* Journal of Electroanalytical Chemistry, 2005. **579**(2): p. 311-319.
7. Bojinov, M., et al., *Conduction Mechanism of the Passive Film on Iron Based on Contact Electric Impedance and Resistance Measurements.* J. Electrochem. Soc., 2001. **148**(6): p. B243-B250.
8. Chao, C.Y., Lin, L.F., and Macdonald, D.D., *A Point Defect Model for Anodic Passive Films III. Impedance Response.* J. Electrochem. Soc., 1982. **129**(9): p. 1874-1879.
9. Macdonald, D.D. and Urquidi-Macdonald, N., *Theory of Steady-State Passive Films.* J. Electrochem. Soc., 1990. **137**(8): p. 2395-2402.
10. Zhang, L., et al., *Onthe Kinetics of Growth of Anodic Oxide Films.* J. Electrochem. Soc., 1998. **145**(3): p. 898-905.
11. Macdonald, D.D., *Passivity-the key to our metals-based civilization.* Pure and Applied Chemistry, 1999. **71**(6): p. 951-978.
12. Beverskog, B., et al., *A mixed-conduction model for oxide films on Fe, Cr and Fe-Cr alloys in high-temperature aqueous electrolytes--II. Adaptation and justification of the model.* Corrosion Science, 2002. **44**(9): p. 1923-1940.
13. Cheng, Y.F., Yang, C., and Luo, J.L., *Determination of the diffusivity of point defects in passive films on carbon steel.* Thin Solid Films, 2002. **416**(1-2): p. 169-173.

Chapter 6

Summary and Future Work

Two major issues have been addressed in this thesis. First, experimental techniques were applied to ascertain the behavior of iron in aqueous solutions. This work was performed in order to generate a model capable of describing the kinetics of oxide growth on iron. In addition, based on the experimental evidence, a possible explanation for the variety of behaviors (an suggested structures) exhibited by iron oxide over the passive range has been proposed. The second major issue that was addressed in this thesis is that a model was developed and used for two purposes. One was that the model was applied to help implicitly determine which defects occur in the oxide formed on iron. The other was to generate kinetic parameters for the model in which could be used to make future predictions based on the occurrence of general corrosion on iron.

The experimental evidence, and in particular, the Mott-Schottky experiments seem to point to a change in the defect concentrations/types. It has been proposed in this thesis, based on the Mott-Schottky experiments, that three distinct regions exist over the passive range for iron. The first region displays a different defect concentration when the potential is swept through it. The second region is the main passive region, over which a stable, higher impedance film forms. The third region corresponds to a sudden change in the electronic character of the film and exhibits a change from n-type to p-type behavior. Two reasons have been proposed for this change in behavior. First, at the higher

potentials in the passive range, the oxygen activity at the surface increases, thereby decreasing the concentration of oxygen vacancies (donors). By decreasing the concentration of donors in the film, the cation vacancies (acceptors) become the dominant defect and alter the film's electronic character. The other proposed reason is that the iron oxide changes to three distinct phases across the passive region. In the lower potential region, Fe_3O_4 is the stable phase and due to its higher conductivity the lower impedance values in this region can be explained. The stable phase in the middle potential range is the less conductive γ-Fe_2O_3. Then, in the high region a new phase, possibly the LAMM phase, becomes the stable phase. Due to the cation deficiency of the LAMM phase, the film takes on the p-type character as displayed by the Mott-Schottky plots in this region.

Based on these proposed ideas, a PDM was used to describe the film in the stable region II (mid-passive range). The results were two-fold. First a PDM was derived to account for only oxygen vacancies being present in the film. However, due to the lack of a suitable prediction (mainly negative film thickness and high defect diffusivities), it was implicitly shown that the oxide formed on iron must have other defects present to account for its behavior. Therefore, a PDM containing iron interstitials and oxygen vacancies was used to study the kinetics surrounding the general corrosion of iron for various temperatures. The results yielded values for the kinetic parameters that can possibly be used to quantify general corrosion damage on iron.

Another major issue worth noting here is that many recent papers are assuming that the structure of the stable passive film formed on iron is the LAMM phase, as proposed by Davenport et. al. The work performed in this thesis indicates that the proposed LAMM structure is the exception and not the rule. In other words Davenport et. al. designed experiments to produce a passive film on iron, but the formation potential used in their work is high in the passive range, very near a transpassive range. Therefore, as pointed out in this work, the electronic character of the film changes to the p-type behavior as would be indicative of the LAMM structure. However, the majority of the passive range displays a n-type electronic character, which would not be possible to obtain with the LAMM structure, due to the majority of defects being cation vacancies.

As for future work on this subject, it is the author's hope that others will continue to use novel techniques for probing the film formed on iron. Although iron oxide (rust) has been studied for over a century (and possibly a millennia), its nature still eludes us today. One of the main focuses should be to research more techniques capable of definitively identifying and quantifying the defects present in the oxide formed on iron. Also, the most in-depth structure studies on iron have really only been performed on oxides formed at high formation potentials and this could lead to an incorrect view of the oxide formed on iron oxide. Therefore, a detailed and precise structure study should be performed across the entire passive region to better understand all of the interesting behaviors exhibited by this age-old material.

VITA

Brian M. Marx

Brian M. Marx was born on May 9, 1972 in Johnstown, Pennsylvania. He was the first of six children in the family. After graduating high school, he went to work for a railcar manufacturer in Johnstown. It was during this time that Brian's interest in metallurgy was first realized. After working for nine years, he enrolled in the Material Science and Engineering Dept. at Pennsylvania State University. While an undergraduate, he worked at the Powder Metal Laboratory at the university. He graduated with his Bachelor's degree in Materials Science and Engineering in May of 2000. Upon graduation, Brian decided to continue with his schooling and began working on his doctoral degree in The Center for Advanced Electrochemical Science and Technology.

Brian Marx is the author and co-author on a few publications pertaining to both powder metallurgy and corrosion. He is a member of the Electrochemical Society and ASM International.